On-Line Fly Ash Characterization

Jean Luc CASTAGNER

IMPERIAL COLLEGE

PhD

Abstract

Monitoring the efficiency of coal burning furnaces is of crucial importance with regard to running costs and emissions. In this work, the carbon content in fly ash, which is indicative of the furnace efficiency, is to be optically determined. The measurement of fly ash particle size and velocity is also investigated. From this information, radiative transfer phenomena and combustion performance can be evaluated inside the furnace.

From sampled fly ash, carbon content can be determined by various techniques such as Thermal Gravimetric Analysis (TGA), Loss On Ignition (LOI) and optical microscopy. For direct measurement in the furnace, infrared emission spectrometry, microwave measurements and polarisation ratio can be used. The latter was proven by Card and Jones (1995) to be approximately linearly correlated with the carbon content, and provides a useful means to analyse in-situ the residual carbon in fly ash.

To this aim, an optical instrument was designed to measure the polarisation ratio. The prospects of integrating simultaneous measurements of carbon content, size and velocity of fly ash particles in coal burning furnaces into a single optical instrument is of great interest, due to the non-invasive nature of such an instrument. This constitutes the aim of the following thesis.

Following a literature review, the design of the optical instrument to measure the carbon content of fly ash particles is presented. A grating projection system (GPS) is studied to achieve velocity measurements at distances up to 3 m and the possibility of sizing particles with this system is investigated both theoretically and experimentally.

An alternative technique using a Two Beam System (TBS) arrangement to estimate particle velocity and size is then described.

The new design of the optical instrument for polarisation ratio measurements has been successfully built and tested, both in laboratory and industrial environments. The investigation of a grating projection system technique to measure particle size and velocity was achieved theoretically and experimentally. Particle velocities up to 20 m/s were measured with this method using spherical glass particles. However, the sizing of particles with this technique was proven to exhibit high uncertainties and therefore was not considered suitable for this use. The Two Beam System technique has been tested for both size and velocity measurements. A broadening in the recovered particle distribution was observed and thought to be due to the non-sphericity in the particles used in the experiment. The GPS and TBS methods were only tested in laboratory with non-absorbing spherical glass particles. However, by extending the theoretical calculations to non-spherical and absorbing particles, the field of investigation of these techniques could be widened to meet more real-world conditions.

Acknowledgments

I would like to express my sincere gratitude to my supervisor Pr. A.R. Jones from the Chemical Engineering Department of Imperial College (IC), whose patience and kindness have been flawless during the three years of this PhD. I also wish to thank him for having supported my ideas and helped me to materialize them. His expertise in the field of light scattering and his ability to transmit effortlessly his knowledge were determinant for the development of my competencies in this particular area of physics.

Many thanks also to Malcom Jones, head of the Electronics Wokshop of the Chemical Engineering Department at IC. His help was very significant in the completion of my experiments. I appreciated very much the interest he took in the development of the electronics that were an essential part of the experiments I carried out.

I wish also to thank Gavin Barnes, Mechanical Engineer from the Mechanical Workshop of the Chemical Engineering Department at IC, for the outstanding work he did on the optical instrument.

Finally I wish to express my sympathy to Dr. Jacqueline Card, Dr. Subbodh Sharma, Dr. Alexis Khokanovsky and Dr. Karim Ouazzane for their day-to-day kindness and support.

This project was supported by the European Coal and Steel Community (ECSC) and funded by Powergen.

Table of Contents

List of figures.

Page

List of tables

Page

List of symbols.

a	distance from the centre of the spherical wave to the grating.	(m)
a	particle radius.	(m)
a_0	amplitude of the DC component.	
a_n	amplitude of the n^{th} harmonic frequency.	
ARC	Anti-Reflection Coating.	
C	BNC cable capacitance.	(F)
d	particle diameter.	(m)
D	distance from aperture to laser beam.	(m)
d_g	grating spacing.	(m)
$\vec{E}$	vector electric field.	
$E_n^{(0)}$	n^{th} incident electric field amplitude.	
f	focal distance.	(m)
f_c	cut-off frequency.	(Hz)
$f_n(\theta,\phi)$	complex scattering function of the n^{th} diffracted order.	
h	distance from optical axis to mirror M_2.	(m)
$\vec{H}$	vector magnetic field.	
I	incidence angle	(rad)
I	intensity.	($W.m^{-2}$)
I_0	intensity at $r = 0$.	($W.m^{-2}$)
$I(x,y)$	intensity distribution in the x-y plane.	($W.m^{-2}$)
I_L	laser beam intensity.	($W.m^{-2}$)
I_L'	laser beam intensity after beam expansion.	($W.m^{-2}$)
I_s^{th}, I_p^{th}	theoretical intensity of s- / p-polarised light.	($W.m^{-2}$)
I_s^m, I_p^m	measured scattered intensity of s- / p-polarised light.	(V)
I_s^c, I_p^c	corrected scattered intensity of s- / p-polarised light.	(V)
$Im(X)$	imaginary part of X.	
k	wave number.	(m^{-1})
$\vec{k}$	wave propagation vector.	
l_0	distance from laser output to mirror M_1.	(m)
$L^{(t)}$	length of the test space.	(m)
m	complex refractive index.	
M	magnifying factor.	
N_p	number of points used in the Fast Fourier Transform.	
P	power.	(W)
Q	absorption efficiency.	
r	radius.	(m)
r_0	$1/e^2$ radius.	(m)
r_s, r_p	minimal distance of the particle trajectory to the beam centre.	(m)
R	resistor load.	(Ω)

R_0	oscilloscope input impedance.	(Ω)
R_c	reflection coefficient.	
R_e	equivalent resistor load.	(Ω)
$Re(X)$	real part of X.	
R_g	radius of curvature of the concave grating.	(m)
R_α	mass specific absorption coefficient.	($m^2.g^{-1}$)
SNR	Signal-to-Noise Ratio.	
t_s, t_p	position of maximum in the fits of the s- / p-polarised light signals.	(s)
THD	Total Harmonic Distortion.	
%THD	Total Harmonic Distortion expressed in %.	
$\overline{u}$	mode of the size distribution.	(m)
v	particle velocity.	($m.s^{-1}$)
V	visibility parameter.	
$V^{(t)}$	volume of the test space.	(m^3)
V_0^s, V_0^p	photomultiplier output voltage for s- / p-polarised light.	(V)
V_i^s, V_i^p	photomultiplier input voltage for s- / p-polarised light.	(V)
w_n^s, w_n^p	coefficients of 2nd order polynomial fits.	
x_m	distance from laser beam to test space.	(m)
x_s, x_p	position of the laser beams centres.	(m)
x_b, y_b	coordinates of impact of the laser beam on the wall furnace (back wall radiation).	(m)
x_i, y_i	coordinates of the image of the back wall radiation.	(m)
x, y, z	axis of referential (O, x, y, z).	
z_f	fractional distance of Talbot Array Illuminators.	(m)

Greek Symbols

α	trajectory angle of the particle.	(rad)
β	laser beam deflection angle.	(rad)
$\beta(\chi)$	non-linear correction coefficient.	
γ_n	n^{th} beam incident angle.	(rad)
$\delta^{(L)}$	laser beam divergence.	(rad)
δ_{sp}	distance between the maximum of the laser beams.	(m)
ε_s, ε_p	rotation angles of the polariser.	(rad)
θ	scattering angle.	(rad)
θ_p	angle of p^{th} diffracted order.	(rad)
λ	wavelength.	(m)
$\frac{\lambda}{2}$	half-wave.	
λ_f	fringe spacing.	(m)
ϕ	diameter of optical components.	(m)
ϕ	azimuth angle.	(rad)
ϕ_i	diameter of the image of the aperture in the test space.	(m)

ϕ_A	diameter of the aperture.	(m)
ρ	density.	($Kg.m^{-3}$)
σ	standard deviation of the Gaussian intensity distribution.	
σ_u	standard deviation of the size distribution.	(m)
σ_m	measured $1/e^2$ width of the scattered intensity Gaussian fits.	(s)
τ	time constant.	(s)
τ_R	refraction angle.	(rad)
τ_L	reflection angle.	(rad)
χ	size parameter.	
ω	pulsation.	(Hz)
ω_{hm}	spatial harmonic frequencies.	(m)
Ω	solid angle of integration.	(strd)

Introduction

Fly ash is a fine powder, usually of colour grey, and is extracted from the flue gas of coal-fired power stations. However its composition varies significantly according to the type of coal. The main elements found in fly ash are silicon oxide, other metallic oxides and unburned carbon. Fly ash particle size distribution is usually found to exhibit mono-modal behaviour, ranging from sub-micrometer to few hundreds of micrometers. It is an absorbing material, for which the imaginary part of its complex refractive index ranges from –0.005 to –0.05. Given that its main component is S_iO_2, the real part of the complex refractive index is usually taken as 1.5.

The determination of fly ash characteristics such as unburned carbon, size and velocity is useful to characterize the combustion process in coal burning furnaces. Mass throughput (to monitor emissions of particulates), ash formation process and coal fragmentation can then be derived from these measurements. Unburned carbon also constitutes a significant loss of energy during the combustion process. Fly ash is also used for the production of cement in the construction industry, where a carbon content smaller than 5% is a requirement.

The carbon content of fly ash is usually obtained with methods such as Loss On Ignition (LOI) and Thermal Gravimetric Analysis (TGA). However, these intrusive techniques require the collection of samples during the combustion process and analysis is carried out afterwards to determine the carbon content. The design of a non-intrusive on-line technique is therefore of interest to obtain this information in a short time compared to LOI and TGA. Recently, Card and Jones [1.42] proved that the polarisation ratio of backscattering of linearly polarized light by fly ash particles is indicative of the carbon content.

Also, with the development of lasers, many optical techniques relative to the measurement of particle velocity and size have been designed and constitute nowadays a wide field of study (the most commonly used being laser Doppler anemometry and phase Doppler anemometry). Velocity measurements of large droplets (3-7mm) have been achieved [I.1] using a laser grating technique, in which a projected structured laser light pattern illuminated the droplets. The main frequency of the signal was afterwards recovered with a frequency-domain Fast Fourier Transform analysis. Similarly, Wang and Tichenor [1.32] investigated the measurement of size of bituminous coal particles by analysing the signal generated by the image of the particle crossing a variable frequency grid. The non-sphericity of the particles was thought to induce large measurement errors.

The advantages of an on-line optical instrument that would simultaneously measure carbon-in-ash, size and velocity of fly ash particles in coal burning furnaces are many: Non-invasive real time measurements, reduced costs, simplified automated operating procedure. Given the operating conditions (c.f. industrial environment below), we designed two techniques for particle size and velocity measurements which could easily be implemented into an optical instrument for on-line measurement of carbon-in-ash. The first one was inspired from the projective techniques described before, and the second one was based on intensity measurement and particle trajectory determination.

Thesis aims and outline

The objectives of the project were twofold:

1 -Design of an optical instrument to measure the carbon content of fly ash. An existing design was significantly modified in order to define more accurately the measurement test space and to reduce the noise due to multiple reflections on the optics. An instrument has been built according to this requirements.

2 -Investigation of size and velocity measurements by means of a single technique. A grating projection technique was investigated for this purpose. In this method, a truncated magnified image of a square grating was projected into the test space. Particles crossing the square wave illumination pattern generated a modified square wave signal whose main frequency was directly related to the particle velocity and whose distortion contained information relative to the particle size. An alternative technique using a two laser beam configuration to measure the velocity and size of particles is also presented. In this technique, the two beam system used to illuminate the test space allowed determination of the 2-dimensional particle trajectory in order to avoid the Gaussian beam uncertainty associated with the intensity distribution of the laser beams.

A literature review constitutes the first chapter of this thesis. An overview of different methods to measure particle size and velocity of particles is given, followed by the investigation of a possible fly ash composition-size correlation. The second chapter is dedicated to the design of an optical instrument to measure the carbon content of fly ash. The calibration procedure and the mechanical/optical characteristics of this instrument are explained in detail. Its application in laboratory and industrial environments, carried out respectively at Imperial College (London) and Powergen's Power Technology Centre at Ratcliffe-on-Soar, is described in the third chapter. Velocimetry and particle sizing methods using a square wave grating projection

technique are investigated in the fourth and fifth chapters. In the final chapter an alternative technique, based on a two beam system configuration to measure the velocity of particles, is presented, along with an intensity technique to measure particle size. In this, the particle location within the beams is obtained from the ratio and delay between the two orthogonally polarised scattered intensities. An algorithm is used to correct the non-linearity in the relationship between particle size and the orthogonally polarised components of the light scattered by the particle crossing the two beam system.

Industrial environment

The industrial environment in which the instrument is intended to be operated is coal-fired power plants. As part of an ECSC (European Coal and Steel Community) project co-ordinated by Powergen, we had to meet the following requirements:

1/ Design of an optical instrument to measure the carbon content in fly ash.

2/ Implementation of the instrument with size and velocity measurements.

3/ Operating conditions:
- Temperature: of the order 700°C.
- Length of test space: up to 6 m.
- Flow velocity: up to 40 m/s.
- Particles: fly ash (up to 20 μm).

Fig.I.1 shows a schematic diagram of the test rig at Ratcliffe-on-Soar on which measurements were made with the optical instrument described in section 2. This test rig is composed of a furnace, in which pulverised coal is burned. An ash box is used to collect the main burnout residues. However fly ash is found in the flow up to the end of the combustion chamber, and varies in size, shape and composition at different steps of the combustion process. The instrument described in this thesis was bolted at the

location indicated in the diagram by "convection duct". At this position, the port connecting into the duct is 12 cm in diameter. This restricted the insertion of the instrument and required a special adaptor to be designed. The width of the duct is approximately 80 cm, which set the maximum length of the test space. However, in some other power plants, the width of the duct can reach 6 m. Typically, the size range of the fly ash particles is up to 20 μm, depending on the location within the furnace duct. Also, the average particle velocity is approximately 10 m/s at this section of the duct.

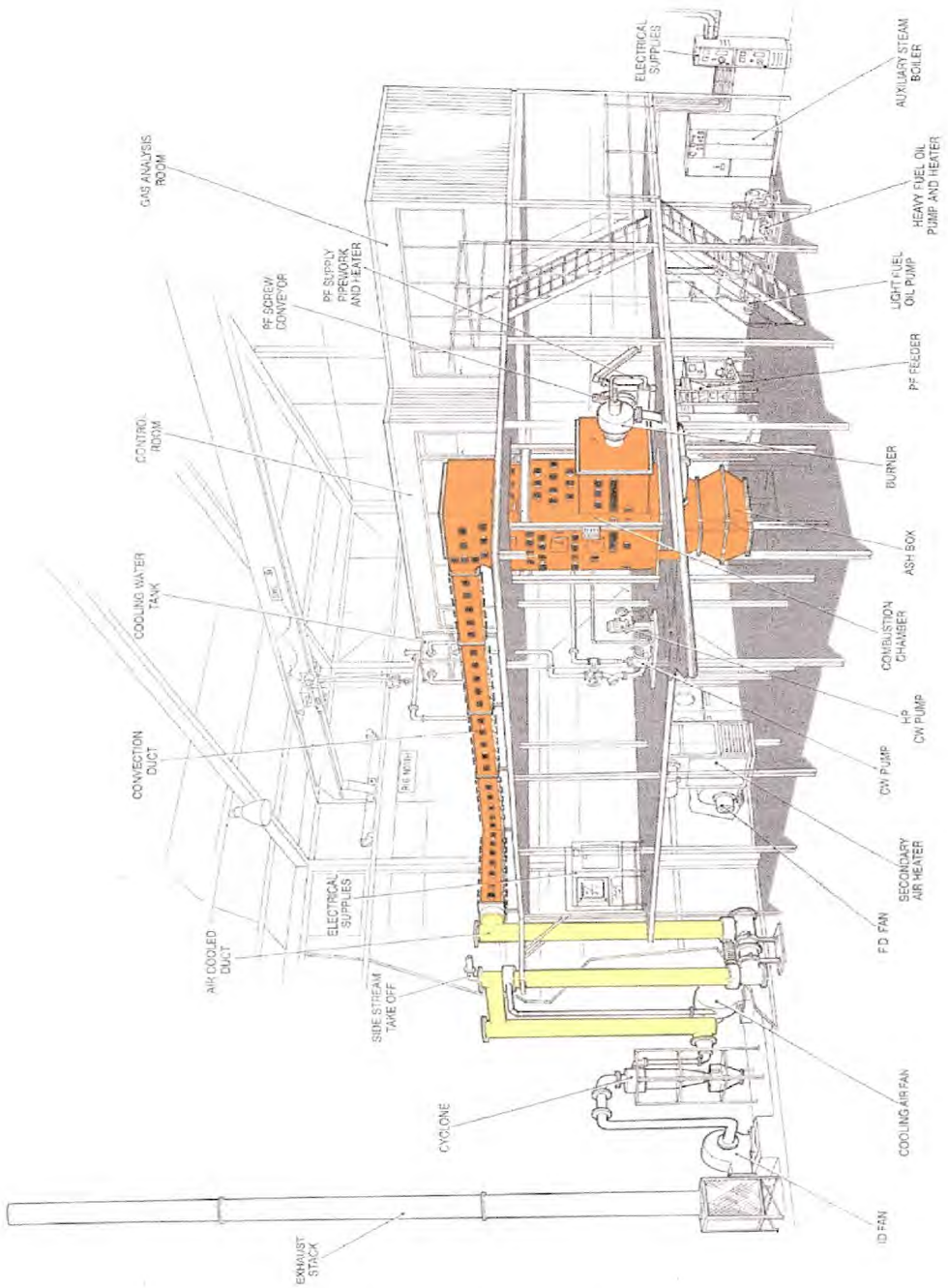

Fig.I.1. Schematic diagram of the test rig
(courtesy of Powergen Ltd).

1. Literature review.

An overview of velocimetry and single particle sizing techniques is given in the first part of this literature survey, followed by a review of studies related to the composition of fly ash and its potential correlation with size.

1.1. Techniques for particle sizing and velocity measurements.

Particle sizing has become a very important subject and is used in many different fields such as combustion, sprays, medicine, paints, pollution control, meteorology, etc. A wide collection of techniques is now available, and we can divide them into two categories: Single Particle Counters (SPC) and ensemble methods. SPC can further be divided into two groups: amplitude dependent and amplitude independent methods.

Absolute intensity measurements, intensity ratio measurements, top-hat and dual-beam techniques fall into the first group, whereas other techniques based on Phase Doppler, projected grids, pulse displacement and visibility are not amplitude dependent, and thus constitute the second group.

As this literature review is linked with the design of an optical instrument operating in low particle concentrations ($0\text{-}10^2/cm^3$), only SPC methods will be examined in this review.

1.1.1. Absolute intensity measurements and laser time of flight velocimeter.

The scattering properties of a homogeneous spherical particle are exactly described by the Lorenz-Mie theory [1.1]. The scattered intensity in the forward

direction is then a function of the particle diameter to approximately the power 4 for sizes greater than 4 μm (in the visible range), and to the power 6 for sub micron particles. Ungut et al [1.2] incorporated this method into Laser Doppler Anemometry (LDA) to obtain simultaneously information on the size and velocity of particles. Depending upon the location at which a particle crossed the sample volume (generated by two laser beams at an angle to each other), the magnitude of the scattered light signal was different. This is a problem encountered when using laser beams, where the radial intensity distribution $I(r)$ is Gaussian[1.3]:

$$I(r) = I_0 * \exp[-2(\frac{r}{r_o})^2] \qquad \text{(Eq.1.1.1.a)}$$

where I_0 is the maximum intensity of the beam, and r_0 is the radius for which the intensity is decreased by a factor $1/e^2$. This is often referred as the trajectory ambiguity problem. This is illustrated on Fig.1.1.1.a for the one-dimensional case [1.4], where two identical particles A and B crossing the beam at two different positions would yield different scattered intensities.

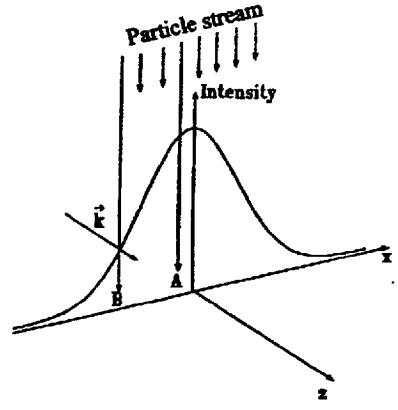

Fig.1.1.1.a. Gaussian intensity distribution of the sample volume.

Holve and Self [1.5][1.6] described a sizing technique using an intensity deconvolution algorithm to statistically correct the size distributions, obtained by measuring the scattered intensity of particles crossing a laser beam with a Gaussian intensity profile. They obtained velocity information by measuring the time of flight of the particle through the sample volume. Holve and Self applied this method to both spherical and non-spherical particles, as well as opaque and transparent. Size accuracy of 5-10% was achieved.

The laser time of flight velocimeter is based on determining the time it takes for a scattering structure to travel from one illuminated region to the next. The spacing between the two regions being known, the velocity component along the bisector between the illuminated spots is given by the ratio between the spacing and the measured time of flight [1.7]. The schematic diagram of this technique is shown in Fig.1.1.1.b.

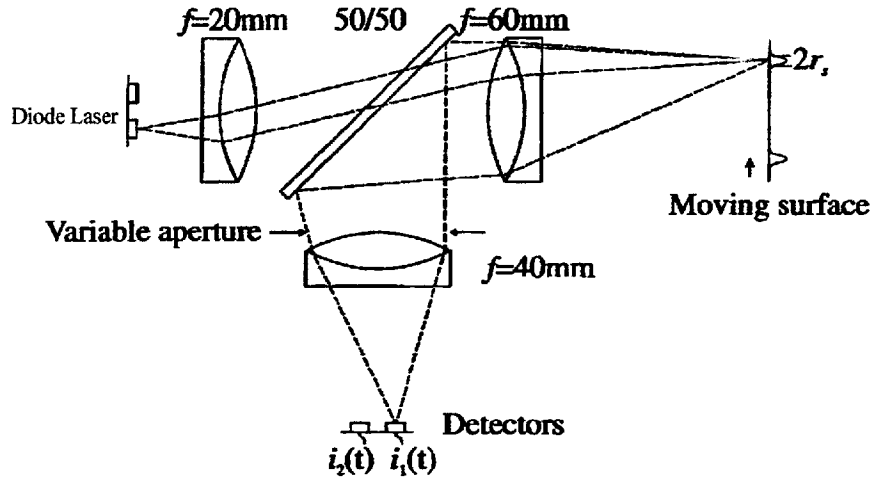

Fig.1.1.1.b. Time-of-flight schematic diagram [1.7].

Baxter [1.8] used a Particle Counter Sizing Velocimeter (PCSV), based on the time-of-flight technique, to study char fragmentation and fly ash formation during pulverised coal combustion processes. When applying this method in an industrial environment, particular care was taken to avoid deposition of dust on the collecting optics.

1.1.2. Dual beam technique.

The light scattered by a particle passing through two concentric beams of different wavelengths in an LDA contains information on its location. The inner beam is used as a trigger to measure the intensity scattered from the outer beam. This avoids problems arising due to the Gaussian nature of the beam profile. This method has been applied to Laser Doppler Anemometry (LDA) by Hess [1.9]. The principle is shown in Fig.1.1.2.a.

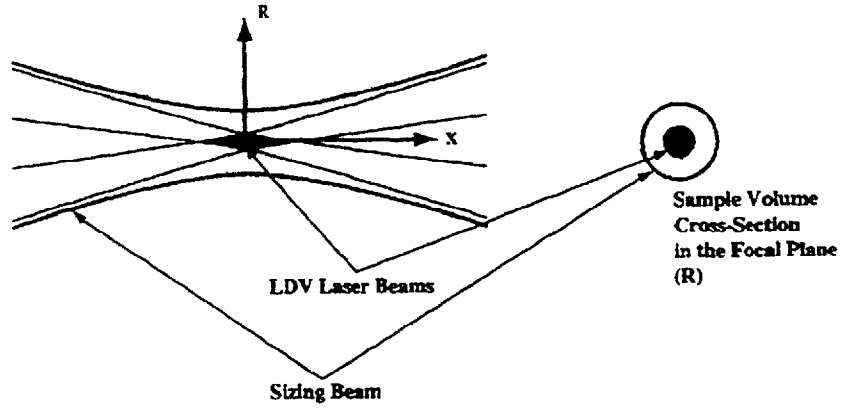

Fig.1.1.2.a Dual beam technique configuration used in a LDA system [1.9].

Fincke et al [1.10] also incorporated this method in a Laser Doppler Velocimeter (LDV) system and performed two-colour pyrometry to get simultaneously size, velocity and temperature of the particle. Size measurements were achieved for particle diameter up to 200 μm.

1.1.3. Top-hat beam technique.

By producing a top-hat beam profile, one avoids the uncertainties in particle size caused by the Gaussian intensity distribution of the laser beam. Laser beams with uniform profiles are also of interest in many different applications, such as laser fusion, laser projection printing, optical data processing, laser radar and coherent imaging systems. Several techniques now available for laser beam shaping are presented hereafter.

By expanding a laser beam and selecting the central part of the expanded Gaussian distribution with an aperture, a nearly uniform irradiance can be achieved (see Fig.1.1.3.a. below).

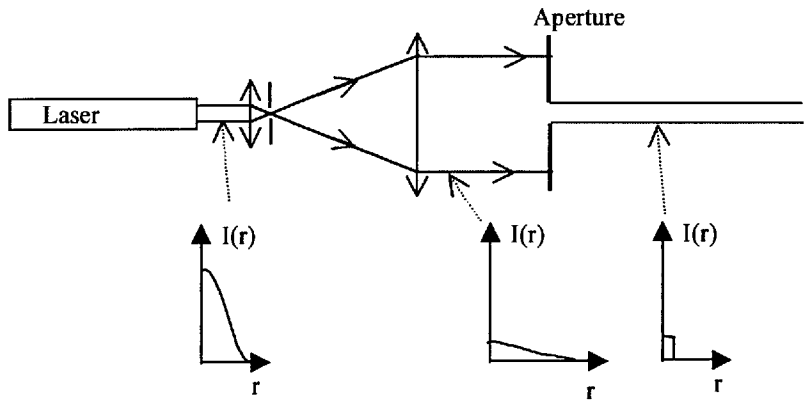

Fig.1.1.3.a. Top-hat laser beam profile generated by selecting the central part of the Gaussian distribution.

Although this technique is straightforward, the energy efficiency is less than 10%, which makes it useful only for low power laser applications.

Another method is to separate a Gaussian beam into two, reverse one of them to produce an axis-symmetric distribution, and then to add them up [1.11]. The result is a nearly one-dimensional flat top profile, the other axis having still a Gaussian distribution. In this configuration, the efficiency is dependent on the optical elements used for the recombination of the two halves.

Different approaches use a phase-only transformation of the laser beam. Pu and Zhang [1.12] presented a theoretical study for generating flattened irradiance of a laser beam by means of aberrated lenses. They showed that by using a lens with a negative spherical aberration coefficient, it is possible to obtain a flattened intensity distribution at two positions along the focused field. The energy efficiency is then a maximum. However, the depth of field of the flattened profile is very narrow.

Similarly, Lu et al [1.13] achieved a uniform profile by producing two-dimensional focusing of the laser beam. This was accomplished with two orthogonal Segmented Wedge Arrays (SWA) to split the incident laser beam into beamlets in both xz and yz planes. The uniform profile, which was the integral of the beamlets, was then obtained at the focus of an aspherical lens. The energy efficiency was also maximum. Fig.1.1.3.b shows the intensity distribution at the focus.

A more complicated method was used by Nemoto et al [1.14]. They designed a system with a deformable mirror, associated with a feedback control loop. The beam profile was determined with a CCD camera, and the correction signal for the deformable mirror was controlled with a computer, which used a genetic algorithm (GA) to obtain

the optimum surface profile. Fig.1.1.3.c below shows the schematic diagram of the laser beam intensity profile control loop.

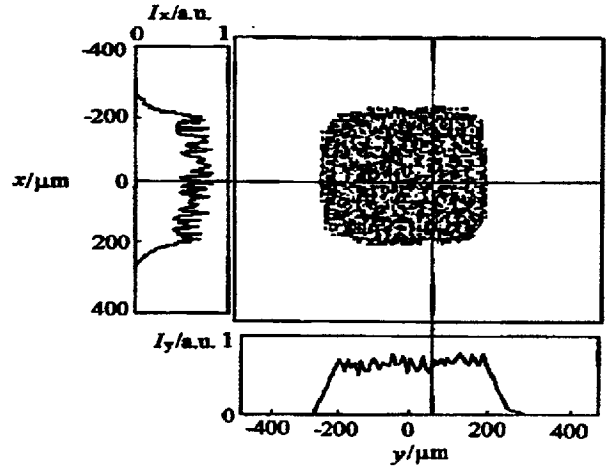

Fig.1.1.3.b. Intensity distribution at the focus of the aspherical lens [1.14].

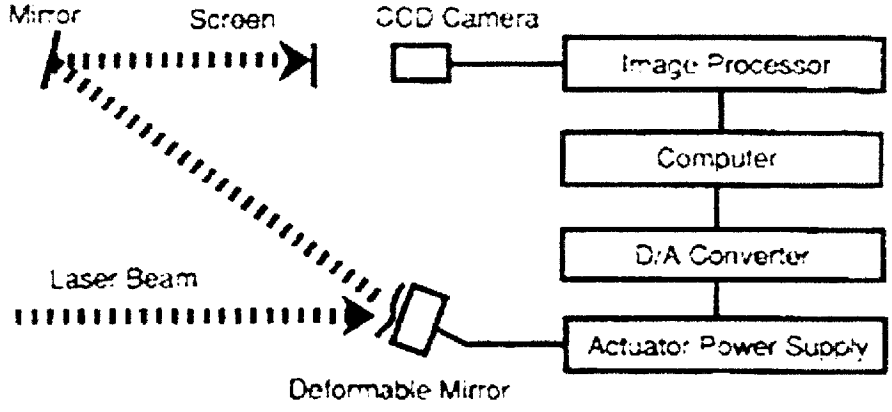

Fig.1.1.3.c.Schematic diagram of the laser beam intensity profile control loop [1.14].

A simpler technique has been proposed by Chang et al [1.15], in which the flattened irradiance was obtained by means of inverse-Gaussian transmittive neutral

density filters. An inverse-Gaussian transmittive filter is a non-uniform absorbing material. When the laser beam was transmitted through this type of filter, the high intensity central part of the beam was reduced to a lower uniform level (see Fig.1.1.3.d.)

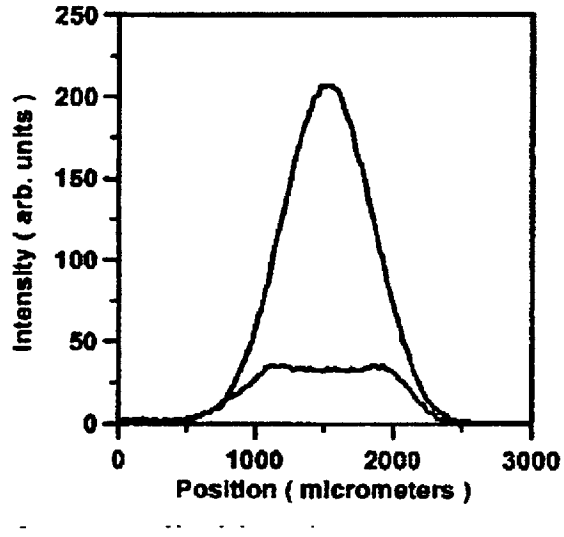

Fig.1.1.3.d. Intensity profile of the unfiltered (top curve) and filtered (bottom curve) Gaussian laser beam irradiance [1.15].

Such filters have typically a transmission efficiency less than 10% and less than 3% of intensity fluctuation. However, because they are simple to use and inexpensive, they constitute a good compromise.

More recently, Liu and Gu [1.16] proposed a laser beam shaping method using polarisation-selective diffractive phase elements (PDPE). In their theoretical work, they studied the transformation of a Gaussian irradiance of circular polarisation by two PDPE made of birefringent material. (P1 and P2 were the input and output planes respectively. $U_{1\alpha}$ and $U_{2\alpha}$ were the input and output optical field).

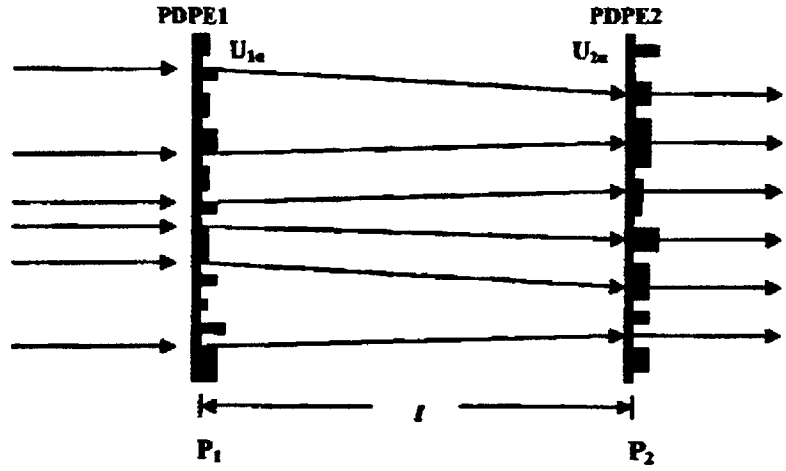

Fig.1.1.3.e. Schematic diagram of a beam shaping system composed of PDPEs [1.16].

PDPE1 was used for the transformation of the Gaussian profile into a uniform profile. PDPE2 was used to compensate the phase of the output field, in order to achieve its propagation without any distortion. They obtained a top-hat profile with high diffractive efficiency.

1.1.4. Intensity ratio measurements.

This technique allows measurements of particle sizes in the range 0.1-10 μm [1.17]. Hodkinson [1.18] showed that it is possible to get information on particle size by measuring scattered light intensities at different angles within the main lobe of the Franhofer diffraction pattern. However, this method has shown large uncertainties associated with the relative refractive index. Measurements became independent of refractive index only for the primarily diffracted light, i.e. in the near forward direction [1.19]. Fig.1.1.4.a illustrates the basic set-up used for this technique [1.4].

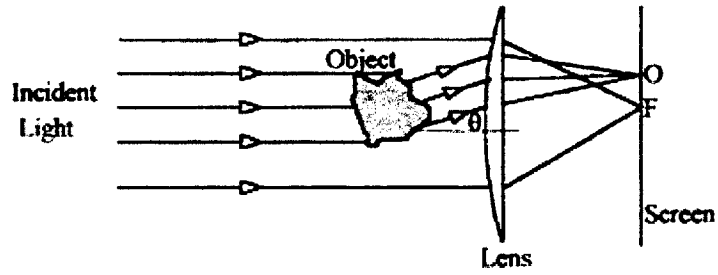

Fig.1.1.4.a. Basic set-up for intensity ratio measurements [1.4].

Another method called Polarisation Intensity Ratio (PIR) aims at measuring the ratio of two different polarized beams scattered by the particle to measure its size. Azzazi and Hess [1.20] proved this technique has the same uncertainties as the previous standard intensity ratio method.

1.1.5. Laser Doppler Anemometry and Phase Doppler Anemometry (PDA).

Amplitude independent techniques which are widely used in industry nowadays include Phase Doppler Anemometry (PDA) and the Pulse Displacement Technique (PDT).

Velocity and size measurements of spherical particles by Laser Doppler Anemometry (LDA) was first proposed by Farmer [1.21]. LDA is based on the analysis of the frequency of the signal generated by the scattering of a particle crossing a set of interference fringes (see Fig.1.1.5.a. below).

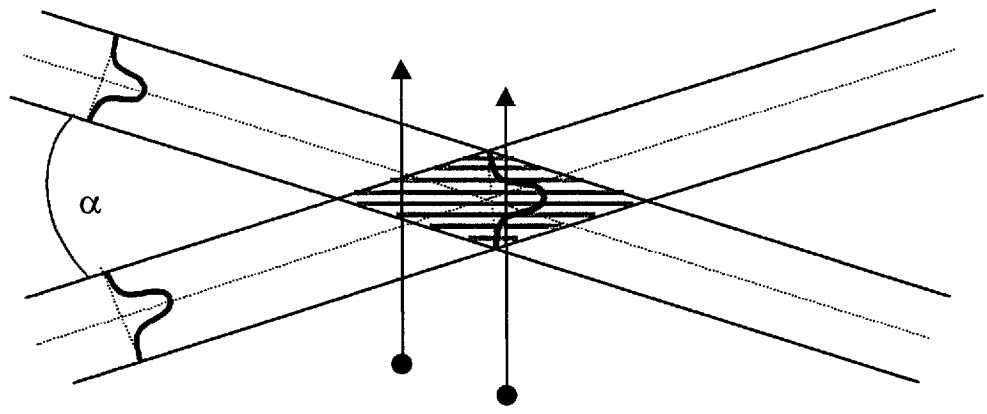

Fig.1.1.5.a. Set of interference fringes created by two laser beams.

A monotonic relationship was established between the visibility of the light scattering signal V ($V = \frac{I_{max} - I_{min}}{I_{max} + I_{min}}$) and the particle size (over a limited range) by using Mie theory with linearly polarized incident light (Fig.1.1.5.b).

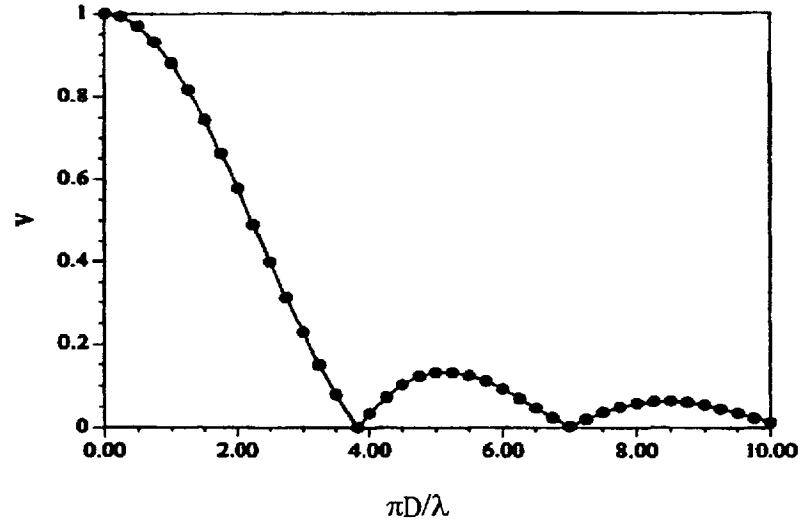

Fig.1.1.5.b.Variation of the visibility parameter V with particle size parameter [1.4].

The LDA visibility technique for sizing particles was proven by Negus and Drain [1.22] to be effective in the backscatter direction when circularly polarized light is used for non-absorbing particles for a size parameter less than 200. However, in the forward direction, the visibility functions are unaffected by the change of the polarisation of the incident light. Azar and Ventrice [1.23] determined that the visibility technique was applicable for particle sizing in the backscatter directio, for specific ranges of refractive indices and specific values of the optical parameters of the receiving optics.

PDA was first proposed by Durst and Zare [1.24], and has since been intensively developed. More recently, Hirleman [1.25] described the Phase Doppler Anemometer in detail. It uses the same principle as LDA for velocity measurements. However, whereas in LDA size measurement is obtained with the visibility parameter *V,* PDA is based on the analysis of the phase difference at two or more spatial locations of the receiving optics from the intensity scattered by a particle crossing a set of interference fringes created by two laser beams [1.26]. Fig.1.1.5.c. and Fig 1.1.5.d. show the computed phase differences versus particle diameter for different particle locations in the test space (a, b, c, d, e, f, g, h, i refer to different positions in a section of the test space) respectively for forward and backward direction [1.27].

The PDA technique offers many advantages such as wide range of measurement (from 0.5 μm to several millimetres), simultaneous measurements of velocity, size and in a particular configuration allows refractive index measurements as well [1.28][1.29].

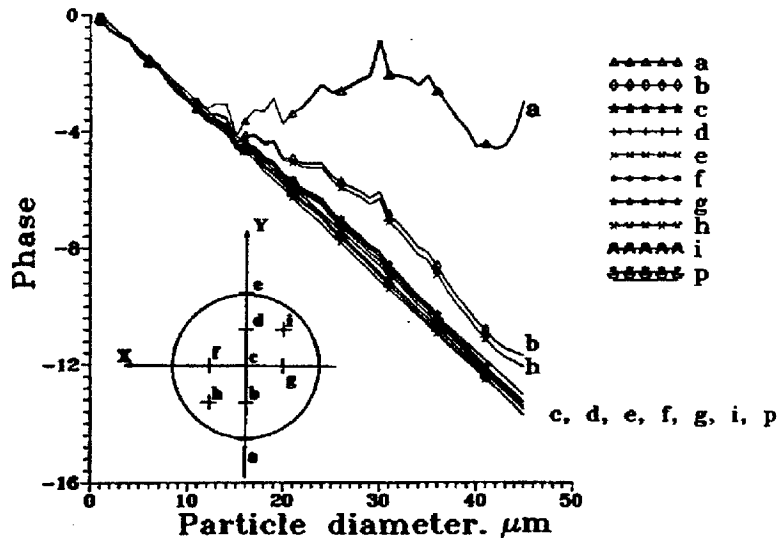

Fig.1.1.5.c. Signal phase versus particle diameter for forward direction [1.28].

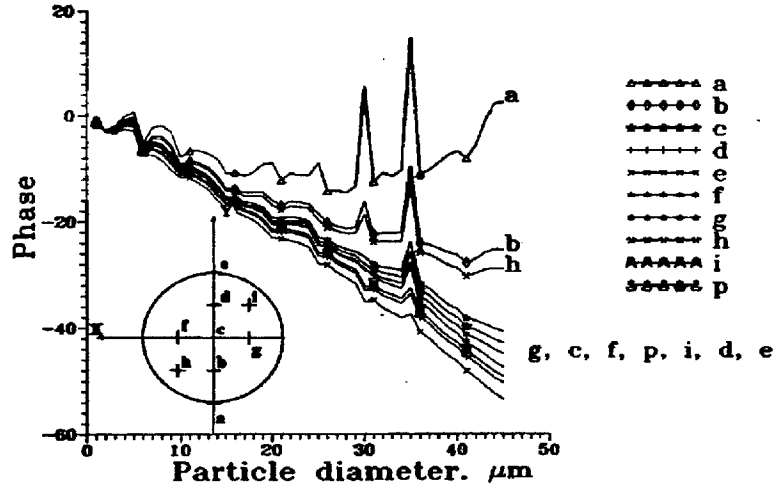

Fig.1.1.5.d. Signal phase versus particle diameter for backward direction [1.28].

1.1.6. Pulse Displacement Technique (PDT).

This technique was first described by Hess and Wood [1.30]. It was thoroughly described in another paper from the same authors [1.31], along with additional implementations like dual receiver and single or dual wavelength configuration. The

PDT method is based on measuring the time delay between refracted and reflected light scattered from a particle as it crosses a laser sheet (see Fig.1.1.6.a. below).

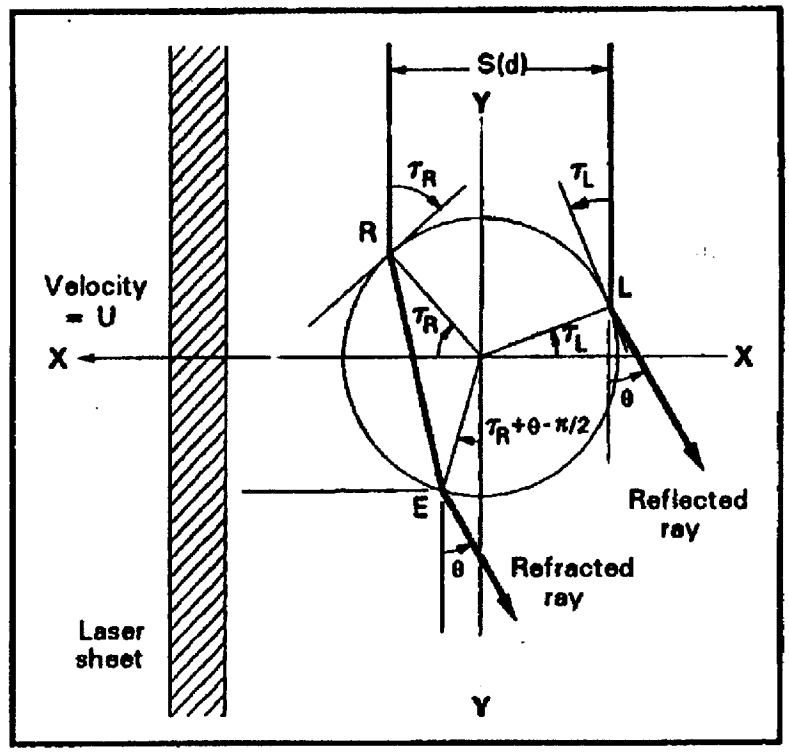

Fig.1.1.6.a. Spherical particle scattering refracted and reflected light at an angle Θ [1.31].

S(d) is the separation distance between the refracted and reflected rays, which is deduced from the measurement of the particle velocity. The particle diameter is then given by the following formula: $d = \frac{2S(d)}{\cos(\tau_R)+\cos(\tau_L)}$, where τ_R and τ_L are the refraction and reflection angles. It is obvious that the measure of the particle velocity is crucial to determine correctly S(d). The authors proposed as well a configuration called "dual receiver", to measure the particle velocity. The schematic of this configuration is shown in Fig.1.1.6.b.

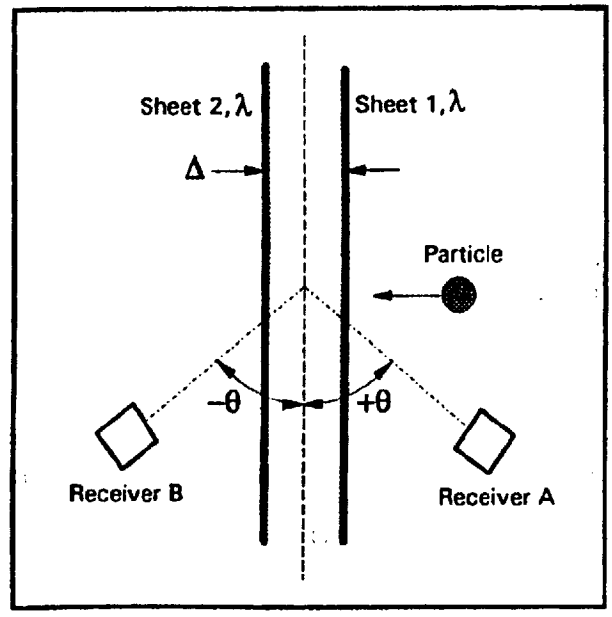

Fig.1.1.6.b. Schematic of dual receiver configuration [1.30]

The sizing limits for this technique range from 0.2 to 1.5 times the thickness of the laser sheet up to several hundred times the sheet thickness [1.17]. Because PDT uses refracted and reflected light, it cannot be used in the backscatter direction.

1.1.7. Projected grids.

Projected grids offer the potential advantage of size and velocity measurement, with little complication regarding the optical configuration.

Wang and Tichenor [1.32] reported sizing particles of diameter larger than 10 μm using a variable frequency grid as shown in fig.1.1.7.a. As the image of a particle passed across the grid, it produced a signal the amplitude of which fell to zero at a position related to the size. Errors less than 10% occurred for spheres. Practically, when measuring sizes of bituminous coal particles and comparing the histograms obtained

with a Microtrac Analyser, they concluded that degradation in the signal occurred due to the non-sphericity of the particles analysed, orientation and rotation distorting the signal.

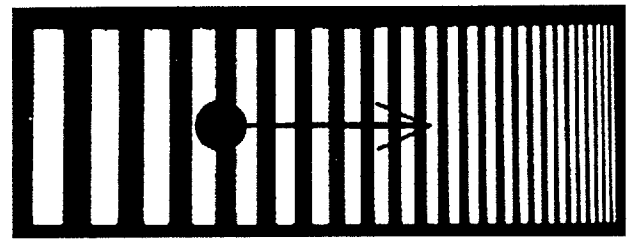

Fig.1.1.7. a. Schematic drawing of a spherical particle passing across a variable frequency grid [1.32].

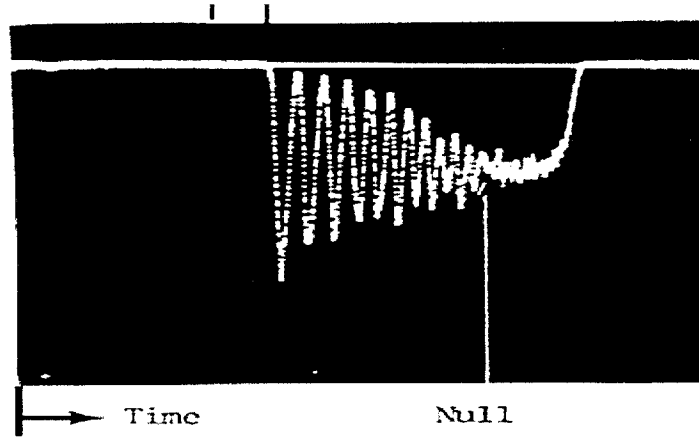

Fig.1.1.7.b. Signal generated by a particle passing across a variable frequency grid (the Null indicates the fall to zero of the oscillation) [1.32].

Additionally, degradation of the signal was noticed when using coherent illumination, due to the variation in particle reflectance coupled with interference effects. Physical limitations are due to the imaging optics, and particles of 10 μm in diameter can be clearly analysed with diffraction-limited lenses. However, better results were obtained with incandescent particles. Similarly, Semiat and Duckler [1.33] used the same

approach by analysing the signals from particles passing through the fringe pattern generated by a grating. Errors occurred in the order of 10-20%.

Systems based on the Talbot effect have been investigated in different applications such as binary logic, interferometry and array pattern generation.

Talbot Array Illuminators (TAIL) subdivide a generally uniform beam into an array of uniform light spots [1.34]: Self-imaging phenomena occur at the Talbot distance $z = \frac{2d_g^2}{\lambda}$ (λ: Wavelength, d_g: Period of the structure of the illuminated object) when the periodic structure is illuminated by a coherent monochromatic beam [1.35]. Furthermore, fractional distances $z_f=pz/q$ have been investigated and it has thus been proven that the diffracted field at these locations is a superimposition of shifted complex weighted replicas of the initial structure [1.36]. Exact images are formed at planes nz (n is an integer greater than 1) and have been numerically simulated for an array illuminator illuminated by a Gaussian beam [1.37]. At higher order Talbot planes ($nz+z/8$), the effect of the non-uniform illumination is more obvious and the uniform profile is degraded. Although at these distances the original structure is not properly conserved, a theoretical treatment could give a good description of the illumination at further distances.

The inhomogeneous quality of fly ash characteristics imply that traditional techniques to measure particle velocity and size, such as LDA and PDA, would be inefficient and inapplicable respectively, especially in the backward direction. It appears that the most suitable techniques to use within the operating conditions (cf. Introduction) of the

optical instrument would be those involving intensity measurements or structured light illumination. It is in this area that this work seeks to make a contribution.

1.2. Fly ash composition- size correlation.

Few articles deal with the analysis of size distributions and chemical compositions of coal fly ash particles. Goshal [1.38] characterised six types of coal from the US. Ramsden and Shibaoka [1.39] analysed four fly ash samples and four original coal samples from four main power stations in New South Wales, Australia. Mamane et al [1.40] studied individual particles from coal and oil fired power plant in Philadelphia, USA. Lee et al [1.41] characterized fly ash collected at successive distances from a boiler. In this study, particle size distribution, density, carbon content and glass content were measured. They mentioned multi-modal particle size distributions for fly ash collected at positions near the boiler and normal distributions further away. Although these studies were performed for specific types of coal, it has been outlined that chemical species such as SiO_2, Al_2O_3, Fe_2O_3, CaO, SO_3, K_2O are the main constituents. Other species like MgO, Na_2O, P_2O_5, BaO, Cl, TiO_2 are present in smaller amounts. The differences in the concentrations of the chemical species quoted above can vary significantly from one type of coal to another.

Card and Jones [1.42] showed a correlation between the carbon content of fly ash and the cross-polarisation ratio of backscattered light. Three types of coal were analysed: Astley, Chinese and Adaro, representing high, medium and low ash content (see Fig.1.2.a. below). Hurt [1.43] examined the size distribution and combustion reactivity with respect to the carbon content, mentioning the increase of carbon content

with increasing size for various fly ash samples from commercial scale pulverized coal fired boilers.

Hill and Rathbone [1.44] investigated fly ash carbon content by means of thermal analysis and optical microscopy. Dykstra and Brown [1.45] compared the photo-acoustic detection of unburned carbon from two excitation sources, namely a He-Ne (632 nm) laser and microwave radiation (12.24 cm). In this technique, the photo-acoustic effect is the conversion of modulated electromagnetic radiation absorbed

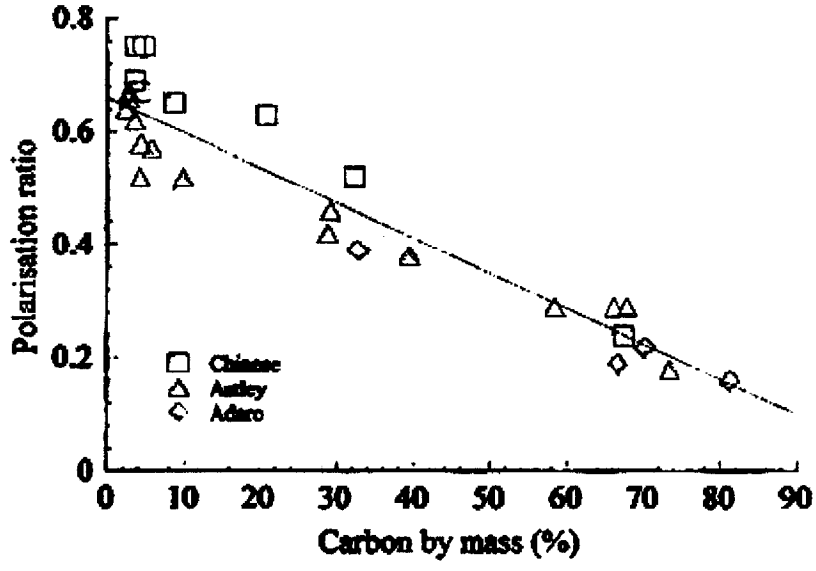

Fig.1.2.a. Polarisation ratio versus carbon content for three different types of fly ash (Chinese, Astley and Adaro) [1.42].

by gaseous, liquid or solid media into an acoustical wave, detected by a sensitive microphone. They used microwave radiation to attain the Rayleigh criterion, where the wavelength of the radiation is much larger than the diameter of the absorbing particle. This Rayleigh criterion is needed to obtain the mass specific absorption coefficient R_a defined as:

$$R_a = \frac{3}{2}\frac{Q}{\rho d} \qquad \text{(Eq.1.2.a)}$$

where Q is the absorption efficiency, ρ is the density and d is the particle diameter. Additionally, they mentioned carbon as a strong absorber of microwave radiation in comparison with mineral matter constituents in fly ash. The conclusion of their experiments was that the microwave photo-acoustic system signal was independent of the carbon particle size distribution, whereas the He-Ne radiation led to a signal dependent on particle size. Later on, Waller and Brown [1.46] studied the photo-acoustic response of carbon content in fly ash to infrared radiation.

Noda et al [1.47] detected the carbon content in fly ash, char and pulverized coal with automated Laser-Induced Breakdown Spectroscopy (LIBS). This technique uses a focused laser beam to produce a hot plasma the temperature of which varies between 10000 K and 20000 K, thus inducing the atomisation of the material inside the measurement area. The signal resulting from the material emission is then a function of its composition. They defined the carbon content as:

$$Carboncontent = \frac{\alpha_c I_c}{\alpha_{Si} I_{Si} + \alpha_{Al} I_{Al} + \alpha_{Fe} I_{Fe} + \alpha_{Ca} I_{Ca} + \alpha_c I_c} \qquad \text{(Eq.1.2.b)}$$

where α_i is a variable factor related to species i containing the plasma temperature and pressure correction factors, and I_i is the emission intensities of species i. They reported a detection time capability of less than 1 min for this technique, in comparison with 30 min for other conventional methods.

Mamane et al [1.40] analysed individual particles from coal- and oil-fired power plants with a scanning electron microscope equipped with an energy dispersive X-ray spectrometer to study size, morphology and composition. They found no dependence of

concentration with particle size for mineral elements Al, Si, K, Ca, Ti and Fe and trace elements Cr, Mn, Ni and Cu. Biermann and Ondov [1.48] showed that a d^2 dependence described the bulk concentrations of As and Se in size-fractionated coal fly ash samples in particles larger than 0.2 μm.

Ghosal et al [1.49] concluded that there is negligible correlation between particle size and composition. In their study, they defined a cumulative parameter $C_0(d)$:

$$C_0(d) = \frac{\int_0^d \delta_0(d')d'^3 \mathrm{d}d'}{\int_0^d d'^3 \mathrm{d}d'} \qquad \text{(Eq.1.2.c)}$$

d is the particle diameter, $\delta_0(d')\mathrm{d}d'$ is the mass fraction (or %) of oxide O present in particles with diameters between d and $d+\mathrm{d}d$. They used Computer Controlled Scanning Electron Microscopy-Energy Dispersive X-ray (CCSEM-EDS) to determine the chemical compositions of individual particles and a Coulter Multisizer to obtain the ash size distribution. Their results regarding $C_0(d)$ versus particle diameter are presented in Fig.1.2.b. They found a correlation between size and composition for S_iO_2, for particles with diameter <8 μm. The analysis of the linear correlation coefficient R for twelve oxides revealed that there is generally no significant correlation between any two oxides. They mention as well that although no significant correlation can be established between size and composition, this latter does vary considerably from particle to particle.

Similarly, Card and Jones [1.42] concluded from their results that the correlation between size and carbon content is almost non-existent, except for very small particles.

No significant correlation between fly ash mineral content and size has thus been clearly established. This can be understood given that fly ash is a very inhomogeneous substance and that its mode of formation depends on the type of coal and on the combustion process during which the coal was burned.

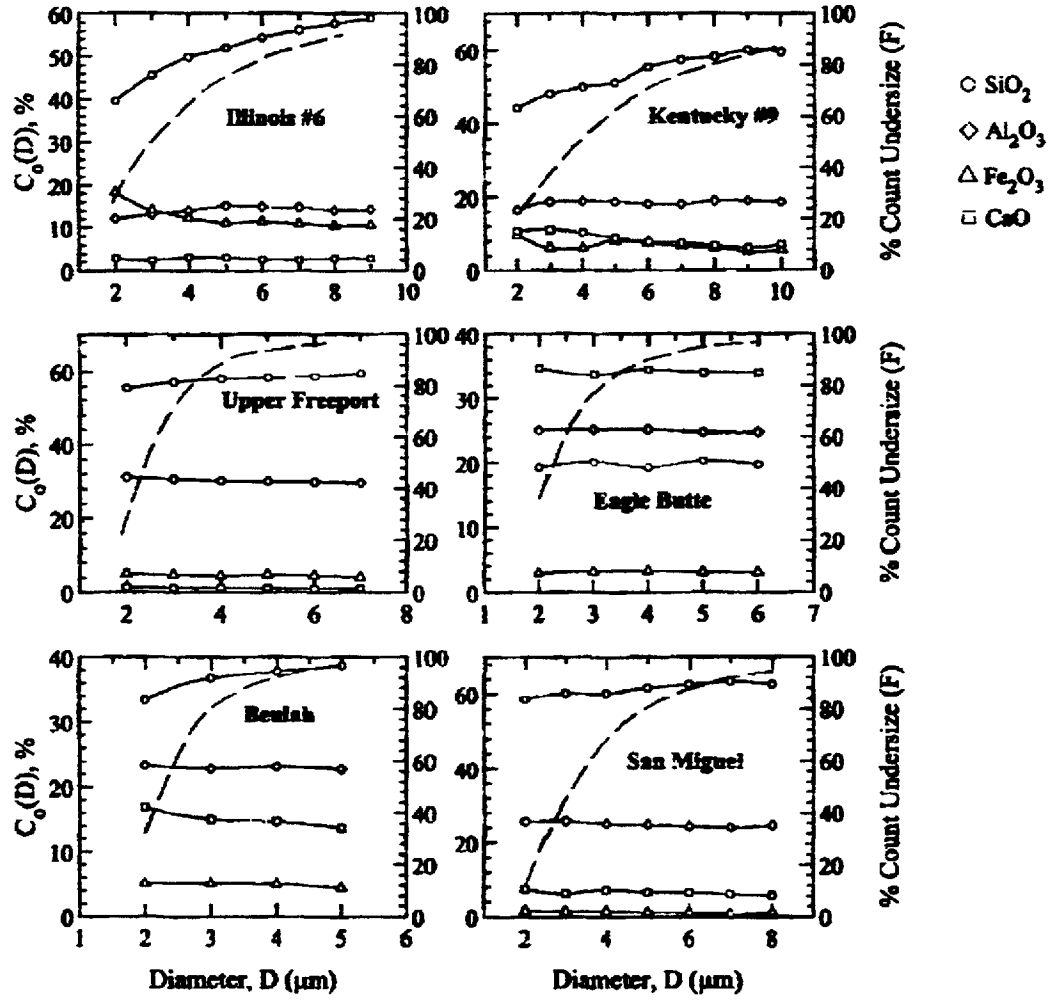

Fig.1.2.b. $C_0(d)$ versus particle diameter (4 oxide concentrations are characterized among 6 different types of fly ash) [1.49].

2. Design of an optical instrument for carbon-in-ash measurements in coal burning furnaces.

The measurement of carbon content in fly ash is commonly achieved by intrusive methods, which require the collection of fly ash samples. These are recovered from the flue gases leaving the furnace area by electrostatic precipitators or suction probes. In coal-fired power plants, a corona discharge in the electrostatic precipitator system charges negatively the ash. After attaching to the collector electrode, rappers induce the fall of the ash into hoppers [1.41]. The techniques used to determine the carbon content of the collected fly ash are, among the most widely used, Thermo-Gravimetric Analysis (TGA), Loss On Ignition (LOI) and burn out in a furnace followed by the measurement of the CO_2 evolved [2:1]. Paya et al. [2.2] mentioned that in LOI, the weight loss resulting from heating the fly ash sample at around 850°C is related to unburned carbon, but also to other components such as carbonates or residual clay minerals. They designed a thermo-gravimetric method combining inert and oxidizing atmosphere to avoid this problem.

Non-intrusive methods present the advantage of on-line real time measurement during the combustion process and do not generally cause significant disturbance. A review of the different techniques existing to date can be found in section 1.2.

In this thesis, the method developed is a continuation from the early work of Card and Jones [1.42]. The ratio of the orthogonal polarisation components in the backscattered light gave an almost linear correlation with the carbon content of the ash. With the aim to adapt this method to industrial environments, an instrument was designed and tested. In this chapter, we present an overview of fly ash properties and describe the design of the instrument for carbon-in-ash measurements.

2.1 Measurement of carbon-in-ash with the cross-polarisation technique.

2.1.1 Nature of fly ash from coal.

Coal fly ash is well known to exhibit strong variations from particle to particle with respect to diameter, shape and chemical composition. Ramsden and Shibaoka [1.39] stressed that knowledge of the bulk composition of the ash is not generally representative of individual particles as the inorganic material in coal is not uniformly distributed. Several factors are then of importance to understand the complexity observed from different individual fly ash particle compositions and morphologies: the occurrences of the mineral matter within the coal, the thermal behaviour of the coal in the furnace and a wide range of decomposition temperatures. Ghosal and Self [1.49] showed by microanalysis of the ash collected in the flue gas of cleaning plant that fly ash consists mostly of spherical particles of impure aluminosilicate glass. Katrinak and Zygarlicke [2.3], however, observed that several sub-micron particles were fused together to form irregularly shaped aggregates. They explained that this phenomenon was probably due to elevated temperatures during the combustion process. Additional vapour-phase condensation following aggregation was thought to smooth the spherule surfaces through the deposition of coatings. Maroto-Valer et al [2.4] stressed that unburned carbon in fly ash has been identified as three microscopically distinct types, namely inertinite particles (non-fused particles), isotropic coke and anisotropic coke (these later two being extensively reacted particles). Their work shown that these 3 carbon types found in fly ash have different physical and chemical properties.

Raask [2.5] was the first to report the presence of cenospheres (i.e. particles with trapped bubbles inside) in 1968. Ghosal and Self [1.38] studied the size-density relationship of fly ash. They reported that sub-micrometric particles can be expected to

be non-cenospheric as the excess pressure needed to sustain bubbles within such a small particle is much greater than that of typical compressed gases trapped in the porous char or the mineral particle itself. The smallest cenosphere observed was approximately 4 μm in diameter. They concluded that the cenosphere content of an ash is positively correlated with the total mineral content of the coal. They also established, given that silica with density in the range 2.2-2.28 $g.cm^{-3}$ is the main constituent of fly ash, its density should not be less than 2.2-2.28 $g.cm^{-3}$. Small ash particles were also sometimes observed inside the voids of the cenospheres. Fig.2.1.1.a. below is an electron microscope picture of a typical fly ash sample. We can observe in it the variation in sizes and shapes.

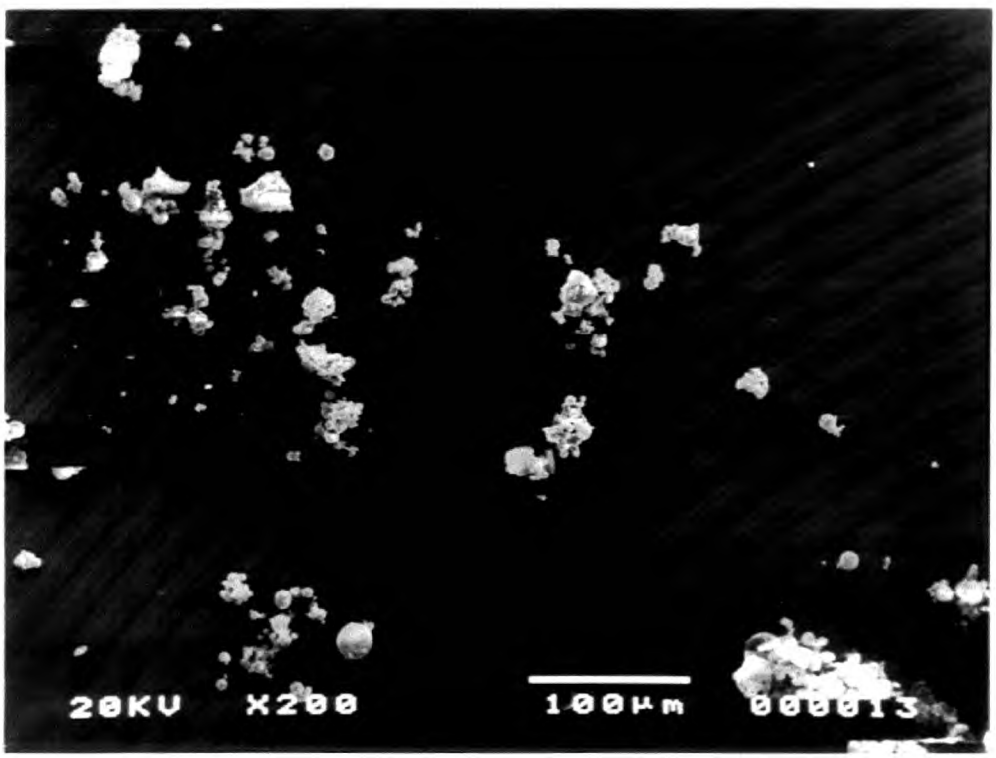

Fig.2.1.1.a. EM picture of fly ash particles.

Fly ash is also known for having a broad size distribution, covering more than 3 orders of magnitude [1.49]. A two-parameter log-normal function is often used to represent broad particle size distributions [2.6]:

$$f(d) = \frac{1}{\sqrt{2\pi d\sigma_u}} e^{-\frac{(Ln(d)-\overline{u})^2}{2\sigma_u^2}} \qquad \text{(Eq. 2.1.1.a)}$$

where d is the particle diameter, $\overline{u}$ is the mode of the size distribution and σ_u is its standard deviation. However, as mentioned previously in the section 1.2, multi-modal fly ash particle size distributions were observed in samples collected near the boiler. Further away the distributions became normal distributions [1.41].

Goodwin and Mitchner [2.7], in their study related to the fly ash radiative properties, showed that it was wrong to assume that the refractive index ($m = n\text{-}ik$) components n and k are independent of wavelength (usual values were taken as n=1.5 and k ranging from 0.005 to 0.05). However, their study was limited to the range of wavelength 1–10 μm, related to radiative heat transfer. Given the differences in shape and composition from one particle to another, it is expected that for individual particles this refractive index will vary greatly at a particular wavelength as well.

Borm [2.8] evaluated the toxicity and occupational health hazards of coal fly ash. The constituents were considered to be metals, polycyclic aromatic hydrocarbons and silica. They mentioned 4 major elements, namely silica, aluminium, iron and calcium. The presence of trace elements like Ni, As, Cr, Pb and Cd was said to differ between fly ash types and also between days and seasons. The concentrations of the different elements were dependent on the type of coal, whereas the amount of carbon also depended on the operating conditions of the furnace.

The carbon content is normally in the range 2 to 15 wt.% carbon [2.9].

2.1.2 Previous work.

Card and Jones [1.42] studied optically the combustion of pulverized coal in a drop tube furnace to obtain information on the properties of the particles resulting from the burning of the coal. Fly ash particle samples were collected at different stages in the combustion process. They established a linear correlation between the cross-polarisation in the backscattered light and the carbon content by mass. In their experiment, the backscattered light, caused by particles crossing a horizontally polarised argon ion laser beam (power: 25 mW, wavelength: 488 nm), was collected at 160° and separated into a straight (notation: s-) and a perpendicular (notation: p-) polarisation components.

2.2 Original design of the instrument.

The first prototype of the instrument was built in 1998 by Dr. Saira Ellahi from the Combustion group of the Chemical Engineering Department at Imperial College, London. It was designed to operate in the backward direction and to incorporate a polarisation splitting optical device. The light scattered from particles crossing the test space was collected by a single lens. The laser beam illuminating the measurement area was sent in the direction of the axis of the optical set up.

Fig.2.2.a shows the schematic diagram of the initial design of the instrument. A linearly polarized laser beam from a frequency doubled YaG laser (50 mW, 532 nm, TEM_{00}) was used to illuminate the particle under test. Two small prisms were inserted to deflect the beam directly into the test space. The first convex lens L1 (ϕ=35 mm, f=35 mm) collected the light backscattered, which was collimated by a concave lens L2

(ϕ=20 mm, f=-30 mm) and then focused at the focal plane of the second convex lens L3 (ϕ=20 mm, f=30 mm). The target position was set by moving lens L2, which, in combination with L1, acted as a telephoto lens. The aperture was used to reduce the depth of field of the system. A third convex lens L4, whose focal point was the same as L3, collimated the light. The light backscattered from the laser was passed through an interference filter at 532 nm. Then a polarisation cube split the incident light into two linearly polarized orthogonal components, which were focused onto two detectors by lenses L5 and L6. The measure of the ratio of the voltages from the detectors gave directly the polarisation ratio.

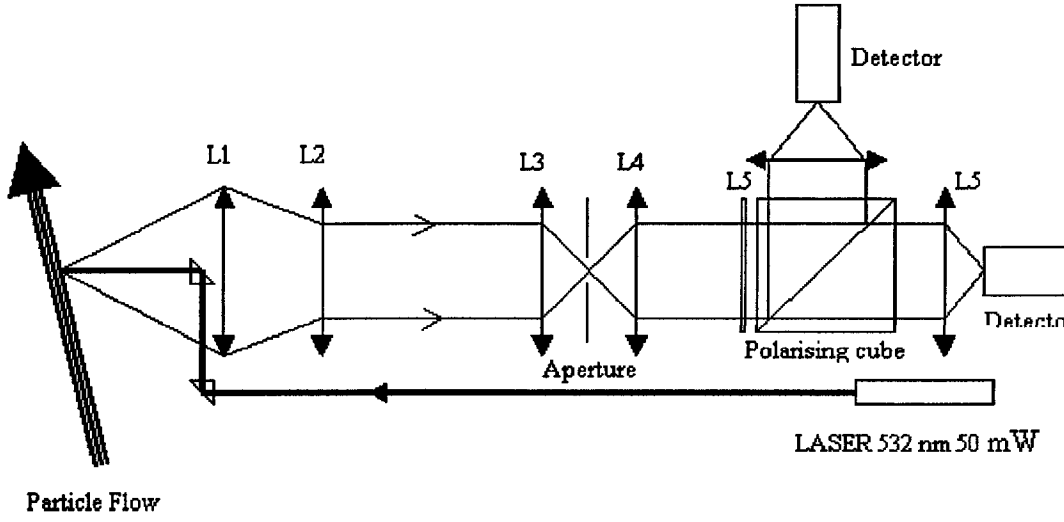

Fig.2.2.a. Schematic diagram of the initial design of the instrument.

2.3 Modifications to the original design.

The first tests we made on the instrument described above showed that the level of light collected by the system was lowered by the successive reflections at the surfaces of the lenses. Indeed, a reflection coefficient of approximately 5% per surface for each

of the 6 lenses lead to a total transmission of $(0.95)^{12}=0.54$. To increase the transmission the number of lenses had to be reduced and an anti-reflection coating (ARC) had to be applied to each of the lens surfaces.

The configuration of the laser beam in the original design implied a depth of field that was only dependent on the collecting lenses and the aperture. It appeared then that for any measurement at long distances in the test space, the depth of field was too long to determine accurately at which position the system was operating. Thus, the laser projection system had to be modified in order to reduce this depth of field. The only configuration possible to solve this problem was to make the laser beam incident at an angle from the lens optical axis. Fig.2.3.a. is the schematic drawing of the instrument with the new implementation. The physical characteristics of the different optical elements used are listed in Tab.2.3.a below.

The laser beam deflection system constitutes a fixed mirror at 45° from which the laser beam is reflected onto a mirror that can be rotated according to the z-axis. The control of the rotation angle allows the operator to orient the laser beam. Therefore, the test space is now restricted by the intersection of the depth of field of the lens-aperture collection system with the laser beam. The target position of the light collection system is determined by the position of lens L1. To achieve accurate positioning, this lens was coupled to a translation table of 10 μm precision.

For all the results presented in section 3 of this thesis, we used two photomultipliers type 9558. The more recent prototype of the probe uses now two miniature photomultipliers type CPM C944 from EG&G. Comparative characteristics of these two photomultiplier types are listed below in Table 2.3.b.

Round mirror 45°	ϕ=12.5 mm, Coating: Laser Line Max-R™ at 45 ° incidence, R_c>99%.
Rotating mirror	ϕ=12.5 mm, Coating: MAXBRITE™ for 0° to 45° incidence, R_c>98%.
Lens L1	Aspheric glass condenser, ϕ=75 mm, f=50 mm, no ARC.
Lens L4	Aspheric glass condenser, ϕ=18 mm, f=12 mm, no .ARC
Lens L5	Convex lens, ϕ=12 mm, f=20 mm, no ARC.
Aperture	ϕ=500 μm.
Polarizing cube	Broadband polarizing cube beam splitter, l=25.4 mm, ARC, 100:1.

Table.2.3.a Physical characteristics of the optical elements used in the design of the instrument prototype.

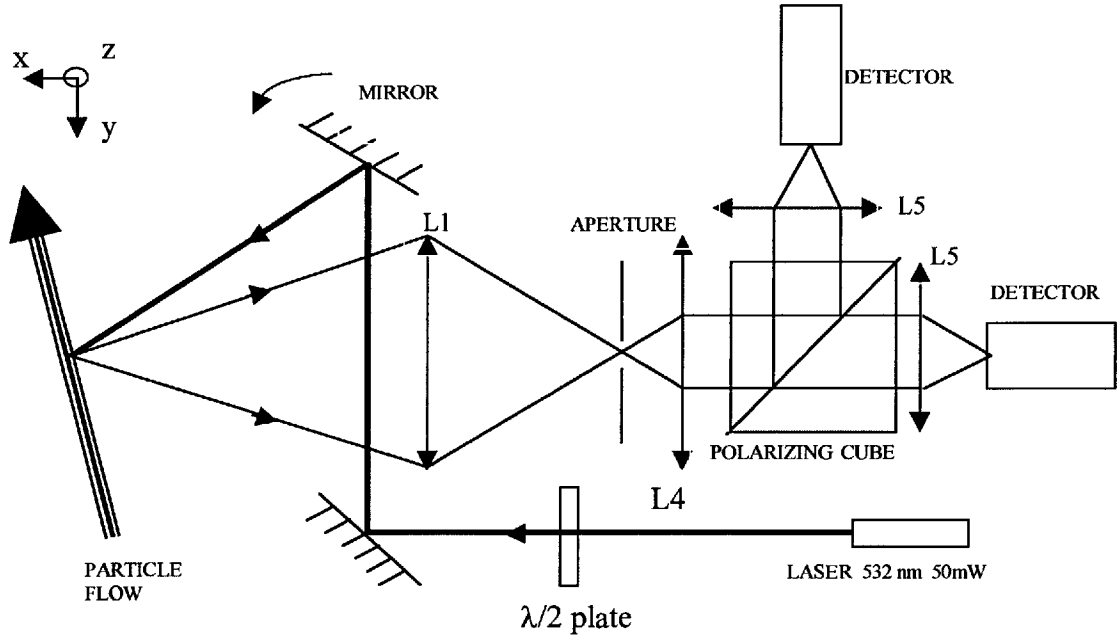

Fig.2.3.a Schematic drawing of the new design for the instrument.

Photomultiplier	Max Gain	Dark current	Time response	Housing Length	Housing Diameter
9558	10^6 A/W	1 nA	10 ns (rise time)	224 mm	75 mm
CPM	3.10^8 A/W	80 pA	3 ns (rise time)	75 mm	10.5 mm

Table.2.3.b. Photomultipliers characteristics.

Apart from superior properties, CPM photomultipliers also reduce the size and weight of the optical system. In order to connect this instrument to a furnace duct, a coupling section containing a quartz window was added in front of lens L1. A nitrogen blowing system was used to avoid accumulation of dust on the window during the measurements. Pictures of the instrument are presented in Fig.2.3.b.

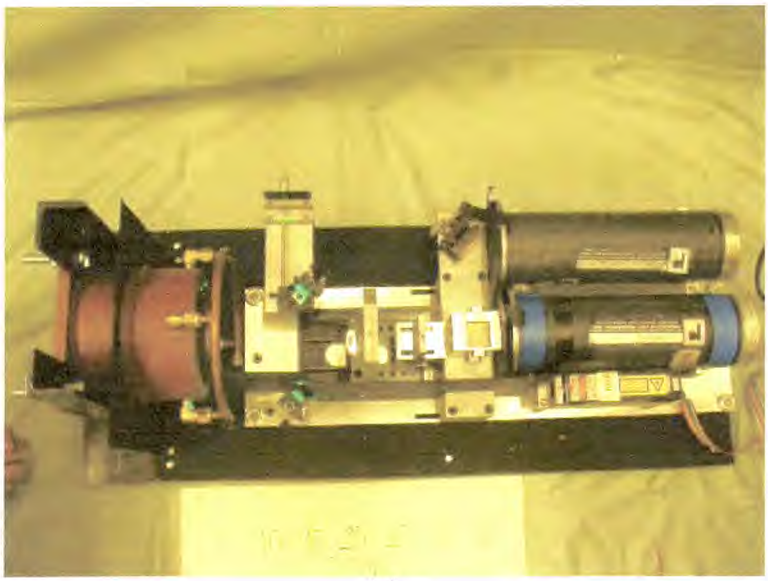

(a)

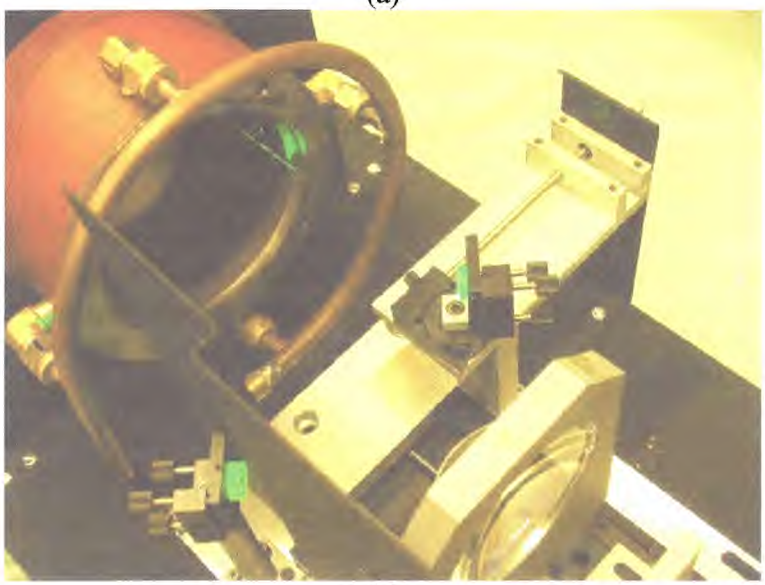

(b)

Fig.2.3.b. (a) Top view of the instrument with the window and N_2 blowing system. (b) The window and the N_2 blowing system.

2.4 Instrument calibration.

Two methods were established for the calibration of the instrument, each of which was related to the type of photomultiplier used. The primary objective of the instrument being to measure the polarisation ratio of the light backscattered by particles, the two photomultipliers analysing the s- and p-polarised light had to be balanced. In both methods, the polarisation of the frequency doubled YaG laser beam was aligned respectively to the s-polarisation of the polarising cube. This was verified by adjusting the λ/2 plate (532 nm) such that a maximum of intensity on the s-polarisation branch of the cube was observed.

Method to calibrate the instrument using the photomultiplier 9558 model.

Because the sensitive area of the cathode is wide (around 150 cm^2) and not necessarily homogeneous for this type of photomultiplier, we used unpolarised light from a tungsten lamp to illuminate fully the cathode of each photomultiplier. Fig.2.4.a illustrates the optical set up. Thus each photomultiplier will analyse the same intensity of light, as $\left\langle \left| \vec{E}_\lambda^{(s)} \right|^2 \right\rangle_t = \left\langle \left| \vec{E}_\lambda^{(p)} \right|^2 \right\rangle_t$ for unpolarised light.

The behaviour of the instrument was explored by Dr Karim Ouazzane from the Combustion group in the Chemical Engineering Department at Imperial College, London. He made measurements with the test space 1m from the collecting lens.

Experimentally, the voltage response to the unpolarised light of the analysed s-polarisation component was set within the linear range of the photomultiplier and the voltage response of the analysed p-polarisation component was adjusted to match.

Therefore, the two photomultipliers were balanced. In order to verify that this was achieved, he used spherical PMMA particles (polymethylmethacrylate).

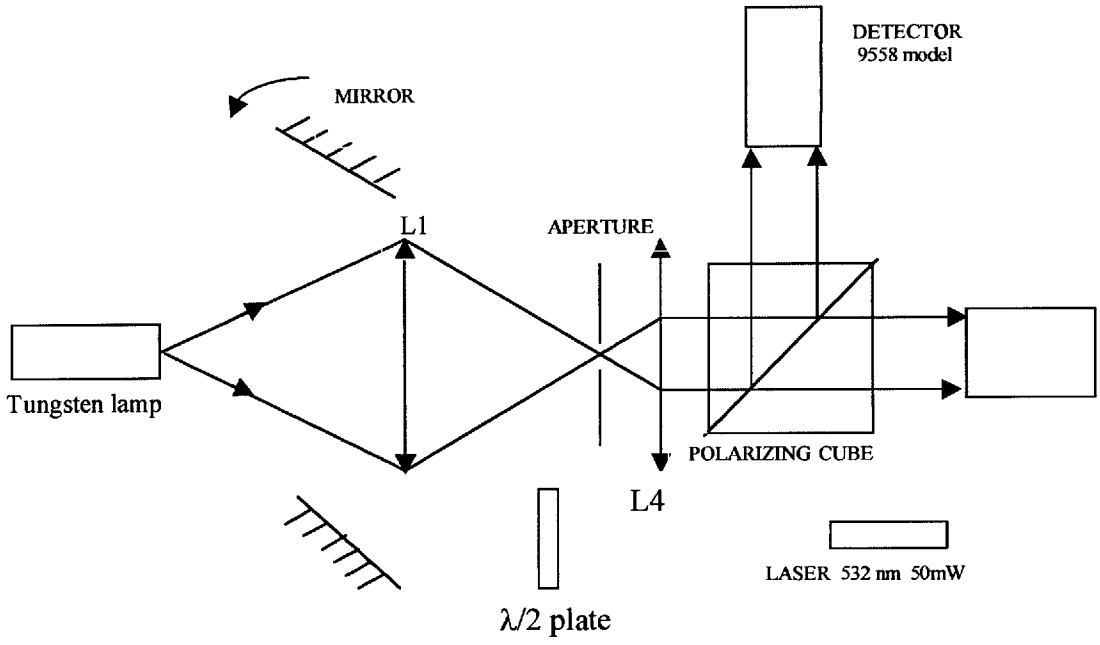

Fig.2.4.a. Optical set up used for calibration with photomultipliers 9558 model.

Spheres are known to have a zero cross-polarisation ratio [2.10], so we expect the polarisation ratio of spherical particles measured with the instrument to correspond to the extinction ratio of the polarising cube, namely 2%. The particles were dispersed by elutriation from a fluidised bed and crossed the test space via a small tube. The instrument observed single particle counts simultaneously on the two photomultipliers, the output being displayed on an oscilloscope. The polarisation ratio for each event was calculated from the ratio of these voltages. Fig.2.4.b below illustrates the measurement obtained with PMMA particles for which size distribution was 40-70 μm. The peak of the distribution is located at 2%, which is the result expected. A significant number of

particles with higher polarisation ratio is present. This is explained by the fact that only perfect spheres produce a zero cross-polarisation. It has been shown [2.11] that a deviation of only 1% from a perfect sphere becomes very significant.

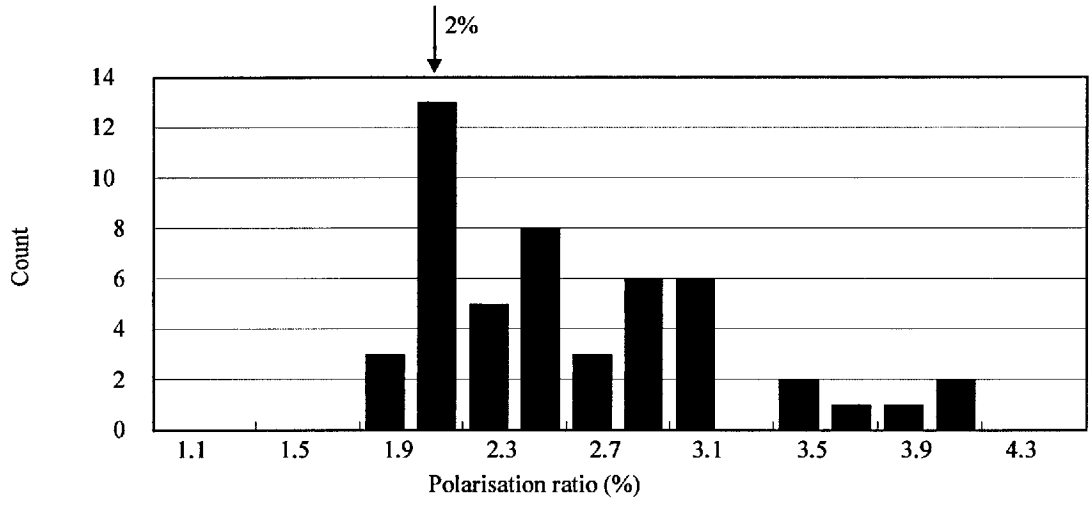

Fig.2.4.b. Calibration with PMMA particles-polarisation ratio distribution.

Method to calibrate the instrument using the photomultiplier CPM.

For this type of photomultiplier (c.f. Table.2.3.b for characteristics), the sensitive area is much smaller (approximately 3 cm^2 compared to 150 cm^2 for the 9558 model). Therefore it was possible to design a more precise approach using a laser beam and varying precisely its polarisation state in order to balance the CPM photomultipliers outputs. To this end, the frequency doubled YaG laser (532 nm) was used. The beam was levelled relative to the optical axis of the instrument. A dielectric mirror was used to reflect the laser beam back into the instrument along its optical axis. Fig.2.4.c below illustrates the optical set up of this calibration method.

The first step of the calibration procedure was to insert a half-wave plate ($\lambda/2$) between the dielectric mirror and the lens L1, and a polariser to ensure a maximum degree of

linear polarisation of the incident laser beam. The λ/2 system (this term denotes the λ/2 plate and the polariser) was then rotated at an angle ε_s so that the maximum of intensity was analysed on the s-polarisation photomultiplier. The s-polarisation CPM photomultiplier voltage $V_i^{(s)}$ was set to obtain on the output voltage $V_o^{(s)}$ the desired signal-to-noise ratio. The (λ/2 system was afterwards rotated to $\varepsilon_p = \varepsilon_s + \frac{\pi}{4}$ to align the laser beam polarisation state to the p-polarisation direction of the polarising cube. The p-polarisation CPM photomultiplier voltage $V_i^{(p)}$ was then adjusted in order to match the output voltage $V_o^{(p)}$ to $V_o^{(s)}$. The precision of the balance of the two photomultipliers was then a function of the precision of the rotating plate used for the λ/2 system and of the extinction ratio of the polariser.

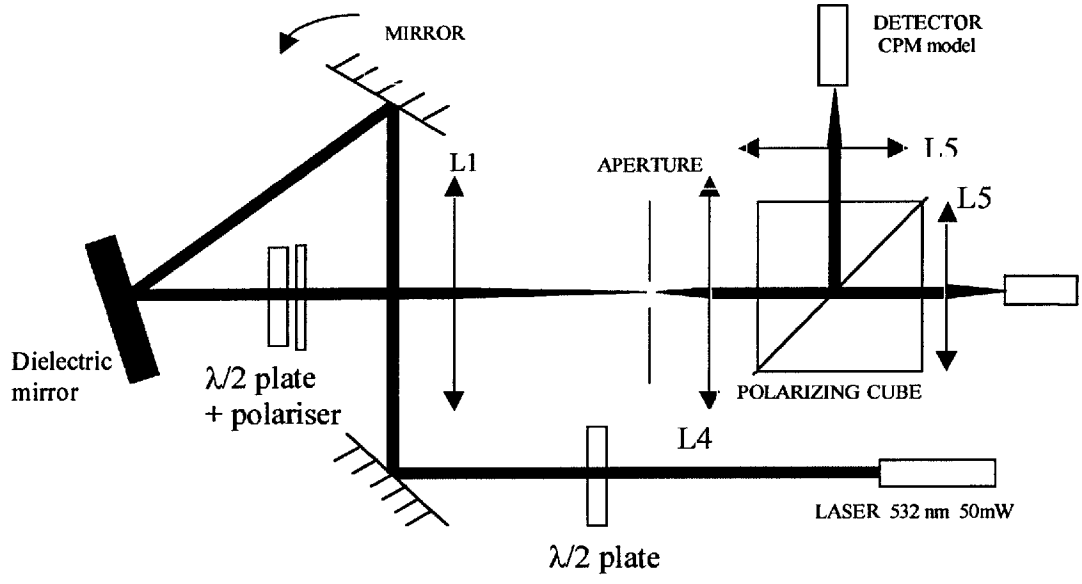

Fig.2.4.c. Optical set up used for calibration with photomultipliers CPM.

A $\pm 0.1^{\circ}$ precision rotating plate and a 500:1 extinction polariser were used for the calibration. If the incident light is a linearly polarised monochromatic plane wave (very good approximation in general for laser beams operating TEM_{00} mode), we can write relatively to the polarisation axis of the polarising cube (s- and p-directions), considering the time variation of the electric field $\vec{E}(t)$ very small compared to the integration time of the CPM photomultiplier:

$$\begin{aligned}\vec{E} &= E^{(s)}\hat{s} + E^{(p)}\hat{p} \\ &= E(\sin(\frac{\varepsilon}{2})\hat{s} + \cos(\frac{\varepsilon}{2})\hat{p})\end{aligned} \qquad \text{(Eq.2.4.d)}$$

Where ε is the rotation angle of the rotating plate, aligned relatively to the p-polarisation.

or in vector representation $\begin{pmatrix} E^{(s)} \\ E^{(p)} \end{pmatrix}$.

The extinction ratio α_c of the cube is defined as:

$$\begin{cases} E_o^{(s)} = \alpha_c E^{(p)} \\ E_o^{(p)} = \alpha_c E^{(s)} \end{cases} \qquad \text{(Eq.2.4.e)}$$

We can express the field transfer matrix of the cube T_c:

$$\begin{pmatrix} E_o^{(s)} \\ E_o^{(p)} \end{pmatrix} = T_c \begin{pmatrix} E^{(s)} \\ E^{(p)} \end{pmatrix} \qquad \text{(Eq.2.4.f)}$$

Therefore ,

$$T_c = \begin{pmatrix} 1-\alpha_c & \alpha_c \\ \alpha_c & 1-\alpha_c \end{pmatrix} \qquad \text{(Eq.2.4.g)}$$

We then have the expression of the fields at the output of the cube:

$$\begin{cases} \vec{E}_o^{(s)} = (1-\alpha_c)E^{(s)}\hat{s} + \alpha_c E^{(p)}\hat{p} \\ \vec{E}_o^{(p)} = \alpha_c E^{(s)}\hat{s} + (1-\alpha_c)E^{(p)}\hat{p} \end{cases} \quad \text{(Eq.2.4.h)}$$

The output intensities are:

$$\begin{cases} I_o^{(s)} = \vec{E}_o^{(s)}\vec{E}_o^{(s)*} = (1-\alpha_c)^2\left|E^{(s)}\right|^2 + (\alpha_c)^2\left|E^{(p)}\right|^2 \\ I_o^{(p)} = \vec{E}_o^{(p)}\vec{E}_o^{(p)*} = (\alpha_c)^2\left|E^{(s)}\right|^2 + (1-\alpha_c)^2\left|E^{(p)}\right|^2 \end{cases} \quad \text{(Eq.2.4.i)}$$

We see that $I_o^{(s)}$ and $I_o^{(p)}$ have the same form when we interchange $^{(s)}$ and $^{(p)}$. This proves that the extinction ratio of the cube is not a parameter necessary to know for the calibration procedure. Therefore the mere equality between $V_o^{(s)}$ and $V_o^{(p)}$ is sufficient.

2.5 Mechanical and test space characteristics of the instrument.

Mechanical characteristics.

As described in the paragraph 2.3, the instrument is operated mechanically by a translation stage of 10 μm precision that positions the collecting lens. A laser beam deflection system is used comprising two mirrors, one fixed at 45° and the other one mounted on a rotating plate. Fig.2.5.a below is the schematic diagram of the mechanical aspect of the instrument. In the following treatment, simple geometrical considerations were used to determine a set of equations to obtain the parameters necessary for the positioning of the instrument.

We have the following relationships between the parameters illustrated in Fig.2.5.a:

$$\beta(x_m) = \arctan(\frac{x_m}{h}) \quad \text{(Eq.2.5.a)}$$

$$y_b = x_b \tan(\frac{\pi}{2} - \beta(x_m)) - h \quad \text{(Eq.2.5.b)}$$

$$y_i = y_b \frac{x_i}{x_b + l(x_m)} \qquad \text{(Eq.2.5.c)}$$

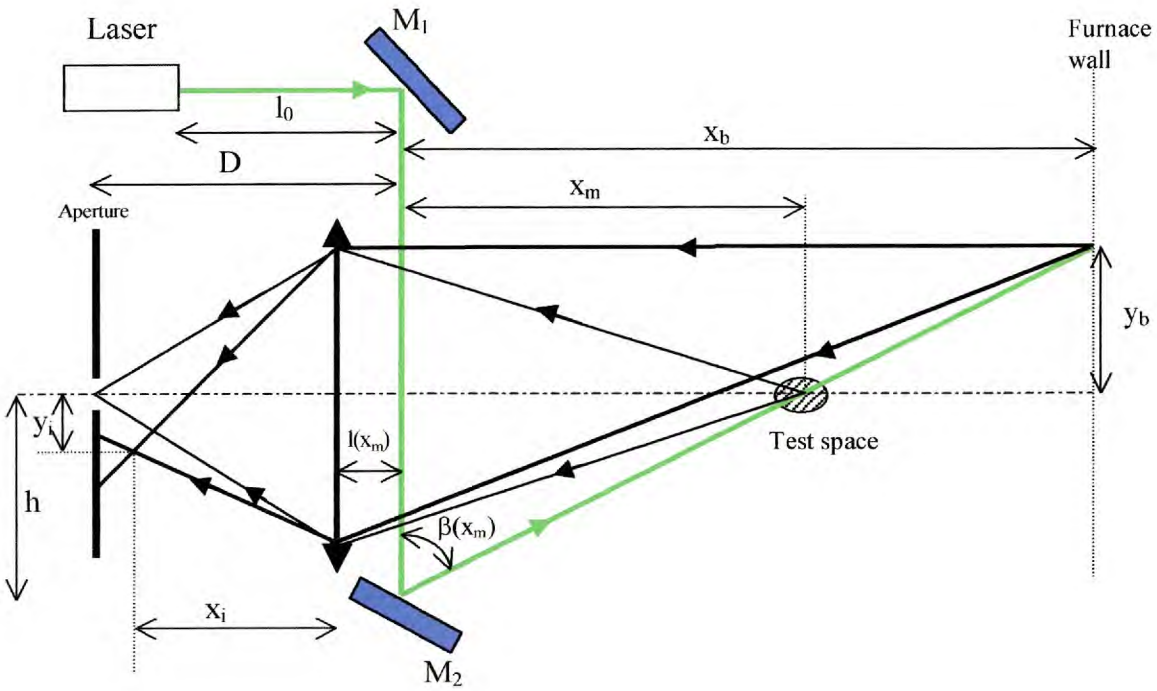

Fig.2.5.a Schematic diagram of the mechanical aspect of the instrument.

$l(x_m)$ is obtained using the well known thin lens equation:

$$l(x_m) = \frac{D - x_m}{2} + \sqrt{\frac{{x_m}^2 + D^2}{4} - f(D + x_m)} \qquad \text{(Eq.2.5.d)}$$

where f is the focal distance of the collecting lens. This equation gives the position $l(x_m)$ for which we have to set the lens in order to target at a distance x_m. Eq.2.5.a provides the angle to set the rotating plate for the deflection of the laser beam.

The background radiation, caused by the impact of the laser beam on the furnace wall, is imaged at the position (x_i, y_i) in Fig.2.5.a. These coordinates are given by:

$$\begin{cases} x_i = \dfrac{f(x_b + l(x_m))}{x_b + l(x_m) - f} \\ y_i = y_b \dfrac{x_i}{x_b + l(x_m)} \end{cases} \qquad \text{(Eq.2.5.e)}$$

Fig.2.5.b below shows the variation of the position y_i=f(x_m) of the image from the reflection of the laser beam on the wall of the furnace located at x_b = 1 m (c.f. Eq.2.5.e above). We can see that at x_m = 0.8 m, the radius of the aperture has to be less than 0.5 mm for the background radiation to be ignored by the system. However, for polarisation ratio measurements, the background radiation is a crucial parameter only if the intensity of the light collected falls outside the linear range of the photomultiplier. When testing the instrument in industrial environment at Powergen Ratcliffe-On-Soar power plant, the aperture diameter was 0.5 mm and the target distance x_m was 0.6 m, which allowed sufficient shielding from the background radiation.

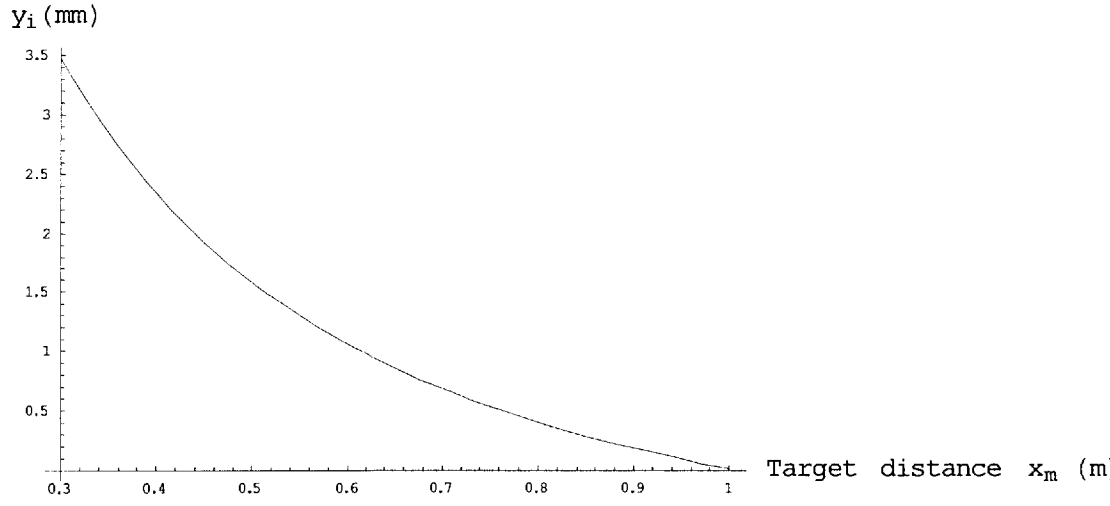

Fig.2.5.b. Variation of y_i=f(x_m) for a wall furnace at x_b= 6m.

Test space characteristics.

The test space characteristics (length $L^{(l)}$ and volume $V^{(l)}$) are important parameters for light scattering experiments. However, for polarisation ratio measurements these are not as fundamental as in Phase Doppler Anemometry, where the scattering angles need to be known precisely [2.12]. In our experiment, it is the volume of the test space which is of interest because the flow concentration varies at different positions along the combustion furnace. The knowledge of these two parameters will allow the user to estimate the occurrences of triggered signals corresponding to particles crossing the test space. The treatment below aims at giving an estimation of $V^{(l)}$ and the length of the test space.

The test space can be approximated as being the intersection in the furnace between the laser beam and the image of the aperture. We can use Eq.2.5.c to obtain:

$$\phi_i = \frac{x_m + l(x_m)}{D - l(x_m)}\phi_A \qquad \text{(Eq.2.5.f)}$$

Where ϕ_i is the image of the aperture diameter and ϕ_A is the actual aperture diameter. The angle of intersection is then given by Eq.2.5.a. Therefore we can approximate the length of the test space as (considering the laser beam diameter to be comparatively negligible):

$$L^{(l)} = \phi_i \tan(\beta(x_m)) \qquad \text{(Eq.2.5.g)}$$

The variation of the beam diameter along its propagation axis is:

$$\phi^{(L)}(x) = (l_0 + 2h + x)\delta^{(L)} \qquad \text{(Eq.2.5.h)}$$

$\delta^{(L)}$ being the laser beam divergence.

An approximation of the test space volume $V^{(t)}$ is obtained by integrating the quantity $\frac{\pi(\phi^{(L)}(x))^2}{4}$ between $x_1 = \frac{x_m - L^{(t)}(\frac{x_m}{2})}{\sin(\beta(x_m)}$ and $x_2 = \frac{x_m + L^{(t)}(\frac{x_m}{2})}{\sin(\beta(x_m)}$:

$$V^{(t)} = \frac{\pi}{4}\delta^{(L)^2}\int_{x1}^{x2}(l_0 + 2h + x)^2\,dx$$

Thus giving:

$$V^{(t)} = \frac{\pi}{4}\delta^{(L)^2}\left\{(l_0+2h)^2(x_2-x_1)+\frac{1}{3}(x_2^3-x_1^3)+(l_0+2h)(x_2^2-x_1^2)\right\} \quad \text{(Eq.2.5.i)}$$

Numerical application:

Using the parameters x_m= 1 m, l_0= 0.3 m, D= 0.125 m, h= 0.03 m, f= 0.05 m, $\delta^{(L)}$= 10^{-3} rad, we obtain the following results: l= 0.0726 m, β= 88.15°, x_1= 0.964 m, x_2=1.037 m and $V^{(t)}$=0.11 cm^3.

Thus, given the particle flow concentration is known, one can adapt the frequency of occurrence of particles crossing the test space by choosing an appropriate aperture diameter.

2.6 Electronic detection system.

The electronic detection system used for the polarisation ratio measurements consisted of a resistor load (typically R= 200 kΩ) mounted in parallel to the output of the photomultiplier, connected to an oscilloscope (R_o= 1 MΩ input impedance) by a BNC cable (C= 100 pF). The equivalent electronic circuit is shown in Fig.2.6.a below.

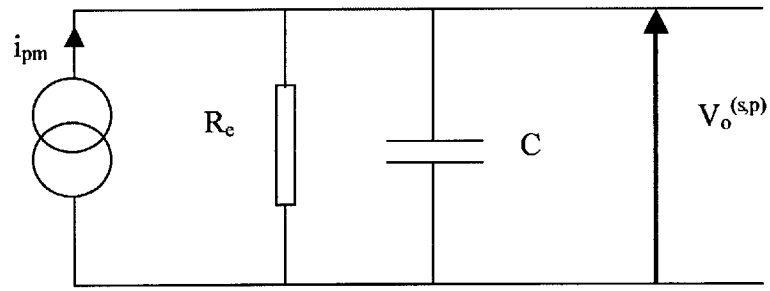

Fig.2.6.a. Equivalent electronic detection circuit.

with R=200 kΩ, C=100 pF and R_o= 1 MΩ, we obtain f_c= 60 kHz.

The resistor R was deliberately set to 200 kΩ in order to smooth out the high frequency oscillations generated by the scattering of light by the fly ash particles. These are irregular in shape and composition and induce a fluctuating scattered signal due to the significant particle inhomogeneities. The signal-to-noise ratio was thus increased. The resulting signal height was analysed and the polarisation ratio deduced. With a wide range of flow velocities, the cut-off frequency would need to be adjusted according to the speed of the particles and the diameter of the laser beam.

3. Measurements of carbon-in-ash using the instrument.

The instrument was tested in laboratory over a wide range of ash samples, from 12 different types of coal, supplied by Powergen. Their mineral content obtained by X-ray fluorescence was also provided. 63 ashes of varying carbon content were then produced from these samples by burning them partially in a furnace. The carbon contents relative to the 63 ashes were afterwards determined by thermo-gravimetric analysis (TGA).

3.1 Measurements from test samples characteristics in laboratory.

The behaviour of the instrument was tested by Dr Karim Ouazzanne. Polarisation ratio measurements of particles dispersed by elutriation from a fluidised bed and crossing the test space via a small tube were achieved. The calibration of the instrument was done according to the procedure described in section 2.4, using a photomultiplier model 9558.

The fly ash content of the 12 samples is presented in table 3.1.a. The carbon percentages obtained with TGA for each ash type are listed as well.

Ash	Fe	Al	Si	Ca	Mg	Ti	Ba	Na	K	P	Mn	Carbon percentages
BET96042	13.7	28	46.4	1.3	1.7	1.2	0.5	0.5	4.1	0.2	0.1	4.9; 0.8; 0.4; 0.3; 0.2
ELC99011	7.4	22	54.5	2.2	2.3	1	0.1	1	2.2	0.2	0.1	9.1; 4.9; 4.4; 3.1; 2.4
LAC98062	7.1	25.8	52.6	3.6	1.1	1.2	0.4	0.3	1.1	0.2	0.1	9.2; 7.4; 6.2; 5.0; 1.1; 0.5
FOR98062	3.7	28	45.7	6.9	2.2	1.5	0.3	0.1	0.6	0.8	0.1	10.1; 9.9; 7.5; 3.5; 4.5; 1.8
ATC98120	3.4	28.9	41.8	8.3	2.2	1.8	0.3	0.2	0.5	1.6	0.1	10.1; 9.6; 6.6; 5.5; 4.5
KNP98092	5.7	26.1	46.8	3.2	1.5	1.2	0.2	0.5	1.1	0.3	0.1	12.1; 7.0; 6.2; 2.0; 1.0
ELC97050	6.8	22.3	51.1	3.2	1.6	1	0.1	0.5	1.7	0.4	0.1	12.6; 12.5; 10.3; 9.7; 9.1
LAJ98062	6.1	21.7	50.9	2.8	0.7	1	0.2	0.3	1.5	0.3	0.1	13.1; 12.7; 8.3; 6.8; 2.2
PRO98070	5.5	19.8	45.8	4.1	2.5	1	0.2	0.9	1	0.4	0.1	16.4; 13.6; 12.1; 4.9; 2.0
cyclone17	5.4	30.25	53.1	4.83	1.73	1.66	0.22	0.4	1	0.48	0.05	14.5; 11.8; 9.2; 4.7; 0.6
cyclone18	5.3	30.8	52.8	4.8	1.7	1.7	0.23	0.4	1	0.5	0.05	15.3; 9.8; 7.4; 4.9; 3.2
cyclone19	5.4	29.7	53.2	4.9	1.8	1.7	0.22	0.4	1.1	0.5	0.06	7.4; 6.1; 5.4; 0.7; 0.3

Table 3.1.a. Fly ash properties.

The results of the polarisation ratio measurements for the 63 ashes are plotted in fig.3.1.a.

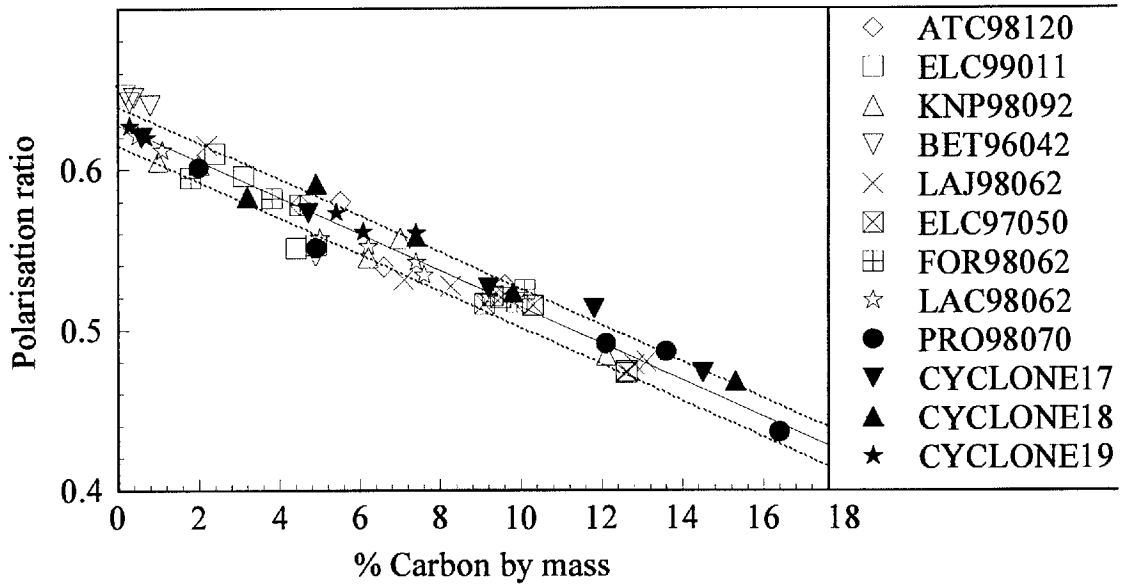

Fig.3.1.a. Polarisation ratio measurements of the 63 different fly ash samples (the dashed lines indicate the standard deviation).

Each point on fig.3.1.a results in the average of 100 polarisation ratios measured from single particles. The standard deviation for each point was 20% of the mean polarisation ratio.The error associated to the measurement of the polarisation ratio to predict the carbon content is then ±1% of the %carbon by mass. It is clearly seen that each type of coal fly ash exhibits a different behaviour, though all have apparently an identical linear trend. The discrepancies are associated to the differences in mineral contents. Because the polarisation ratio is dependent on the carbon content and also the mineral content of the ash, an attempt to predict the carbon content with reduced uncertainty using a Radial Basis Function (RBF) Neural Network (NN) (from the Neural Network Matlab toolbox)

analysis was made. The principle of the RBF Neural Network is illustrated in Fig.3.1.b below, where X is the input vector leading to the output (in our case the carbon content). The outputs from each individual neuron are formed by applying the basis function to the distance between their centre and the input vector. The NN output is then formed by a weighted sum of the neuron outputs and a unity bias so that the training data fit the network model.

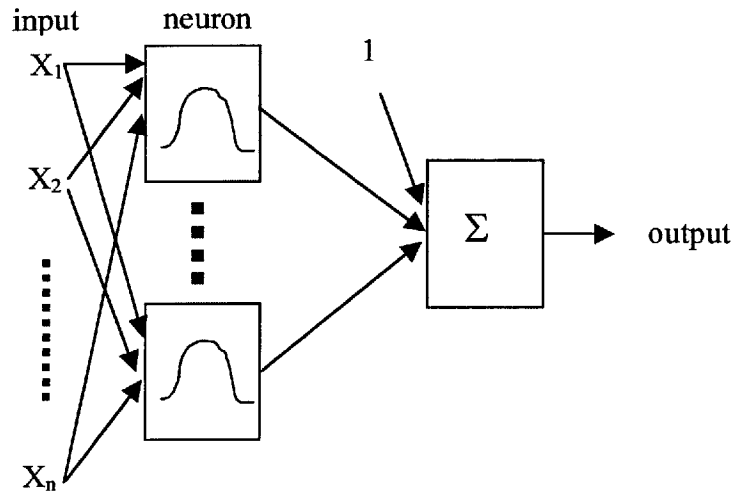

Fig.3.1.b. Schematic diagram of the RBF Neural Network.

The input parameters of the NN were the polarisation ratio and the mineral contents (cf. Tab.3.1.a). The training of the NN was made with 50 samples from the 63 mentioned previously. The results of the validation of the NN analysis made with the 13 remaining ash samples are presented in fig.3.1.c. In this figure are plotted the %carbon determined from TGA versus the %carbon determined from the NN. Thus the uncertainty in the determination of the carbon content by NN analysis was decreased to ±0.5% of the carbon by mass. This constitutes a significant improvement, provided the mineral contents of the fly ash sample are known.

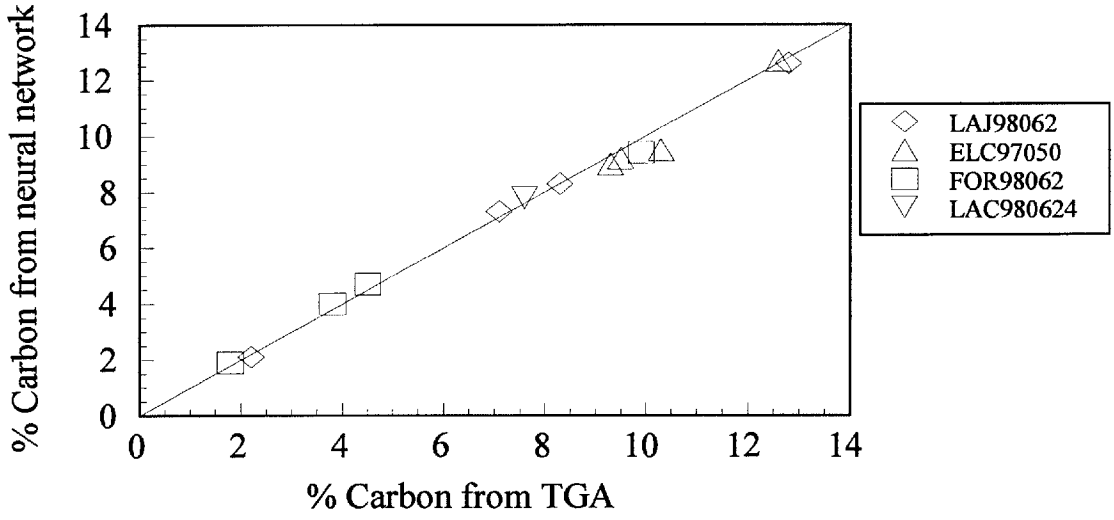

Fig.3.1.c. Validation of the NN analysis.

3.2 Measurements in industrial environment.

In-situ polarisation ratio measurements were achieved with the instrument at Powergen Ratcliffe-on-Soar coal-fired power plant. Two sets of experiments were completed in October 2000 and August 2001. Each time the instrument was bolted onto the furnace chamber at the end of the combustion process and measurements were taken continuously during the test. Because of the particular procedures involved in the running of the furnace, the amount of excess O_2 was varied at different times, leading to different amounts of unburned carbon in the fly ash samples. These were collected before varying the amount of excess O_2 at two positions upstream and downstream of the instrument. The carbon content was determined by Loss On Ignition measurements. The mean of the two LOI was then calculated to determine the average carbon content of the fly ash particles that crossed the test space of the instrument in the furnace. The

corresponding polarisation ratio was obtained by calculating the mean value of the polarisation ratio data obtained between two successive changes of the excess O_2. The results for the two sets of experiments are compared in fig.3.2.a with the results obtained by Dr Karim Ouazzanne in laboratory.

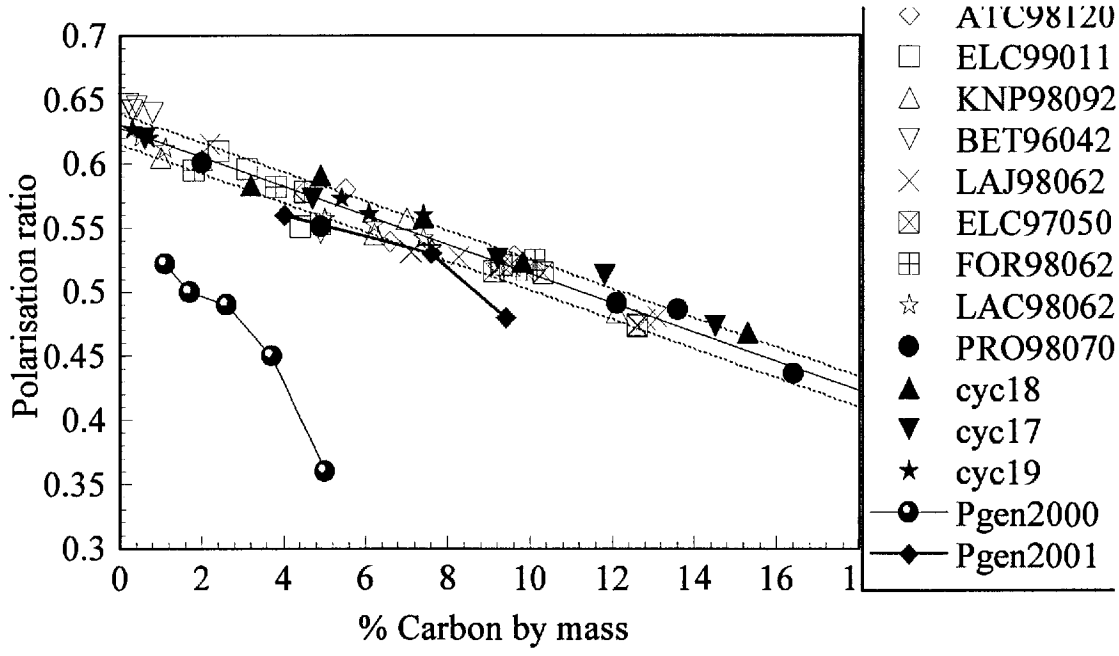

Fig.3.2.a. Comparison between in-situ and laboratory experiments obtained with the instrument.

The trend of the data obtained in 2000 (Pgen2000) are seen to be well off the trend of the data obtained in laboratory. This is thought to be due to the nature of the coal used in the test, that did not correspond to any of the coal fly ash types investigated. However the experiment carried out in 2001 (Pgen2001) presents a general trend that agrees with the data obtained in laboratory. These results suggest that the application of the instrument in industrial environments is feasible. Additional tests will be needed to characterize its full potential use.

4. Development of a fringe projection method for the measurement of velocity.

Nowadays many different techniques are available to measure particle velocities. The Laser Doppler Anemometry (LDA) and Pulse Displacement Technique (PDT) are widely used in industrial environments. A review of these techniques was given in section 1. The possibilities for implementing the optical instrument described in section 2 with such techniques is limited by the industrial environment in which it is meant to operate (c.f. Introduction-Industrial environment). The main obstacles are the length of the duct and temperature gradients within the furnace.

LDA techniques use a fringe pattern resulting from the interference of two laser beams crossing at an angle. Maintaining this angle at a constant value over the length of the furnace up to about 6 m would have been problematic with the fixed restricted 4 inches aperture connecting the furnace to the instrument. Also, temperature gradients within the furnace would cause the deviation of the laser beams, and so would compromise the production of the fringes. Furthermore, LDA was proven to be rather efficient in the backscatter direction (>170°) but with only certain types of particles and nevertheless with higher uncertainties (c.f. section 1.) than for usual scattering angles.

Time-of-Flight Velocimeter techniques are based on laser sheets. These can be produced by focusing a laser beam through a cylindrical lens. Two scattered signals, one relative to the refracted light and the other to reflected light are then analysed. The time delay between them contains the particle size information. The velocity information can be obtained by using two laser sheets, the absolute delay between the two pulses of refracted or reflected light being directly proportional to the speed of the particle in the direction orthogonal to the laser sheets. However this technique is

restricted to spherical particles. Also, the backscatter configuration of the instrument does not allow this technique to be implemented.

We needed to design an optical set up that would allow an intensity variation in the test space to measure particle velocity. Inspired by the Talbot Effect (c.f. section 1), we designed a Grating Projection System (GPS). A projection of periodic patterns is produced with a diffraction grating illuminated by a spherical wave of monochromatic coherent light. The diffracted light is collimated by a lens, the focal distance of which is at the centre of the spherical wave. Experiments have demonstrated that the diffracted orders are spherical waves centred on the same transverse plane as the incident spherical wave. The periodic illumination observed at different locations along the optical axis is proven to be the result of interferences between the diffracted orders.

4.1 The Grating Projection System (GPS).

Self-imaging phenomena have been used in many applications such as fibre optics telecommunications, image processing [1.37], distance measurement [4.1] and planar optics designs [4.2]. Different types of self-imaging phenomena have been reported. The most widely known, the Talbot effect, is the reproduction of exact images of a grating illuminated by a monochromatic plane wave at locations $z = \frac{2nd_g^2}{\lambda}$ (n is an integer, d_g is the grating spacing and λ is the wavelength) from the grating. Many other images occur at the so-called fractional Talbot distances when $n = \frac{m}{p}$ (m and p being natural numbers that do not have a common integer divisor) [1.37]. When the grating is illuminated with an incoherent source of light, the resultant irradiance is known as Lau bands [4.3]. Using the Talbot effect in a convergent beam of monochromatic coherent

light, demagnified truncated images of the periodic structure are created [4.4]. Alternatively, when the periodic structure is under a point-like source illumination, magnified self-focused images are found in a set of focal planes [4.5].

However, the methods described above do not provide the means to produce useful periodic patterns of light over long distances, and are therefore limited to short range applications. The optical set up described in this thesis, called GPS for simplification, produced truncated magnified self images of a grating over distances up to approximately 3 m, beyond which the quality of the images deteriorates.

4.1.1 Experimental Characterization.

A 3 mW He-Ne laser beam of wavelength 633 nm was focused through a 20× microscope objective to create a spherical wave (SW) that illuminated a square wave diffraction grating. The grating step was 125 μm. The diffracted light was then passed through a lens, the focal point of which was at the centre of the SW. Therefore in the absence of the diffraction grating, the laser beam was simply expanded and collimated. Fig.4.1.1.a illustrates the principle of the GPS.

Experiments were carried out, using lenses of focal distances 9, 15 and 20 cm. When varying the position of the observation screen along the optical axis z, the illumination consisted of a periodic pattern which disappeared at certain positions. Therefore we labelled two types of patterns: the in-phase pattern, for which a periodicity was observed, and the out-of-phase pattern, for which the periodicity disappeared. Because of the spread on the z-axis of the in-phase patterns, the uncertainty in recording their positions was bigger than for the out-of-phase patterns, which were less spread.

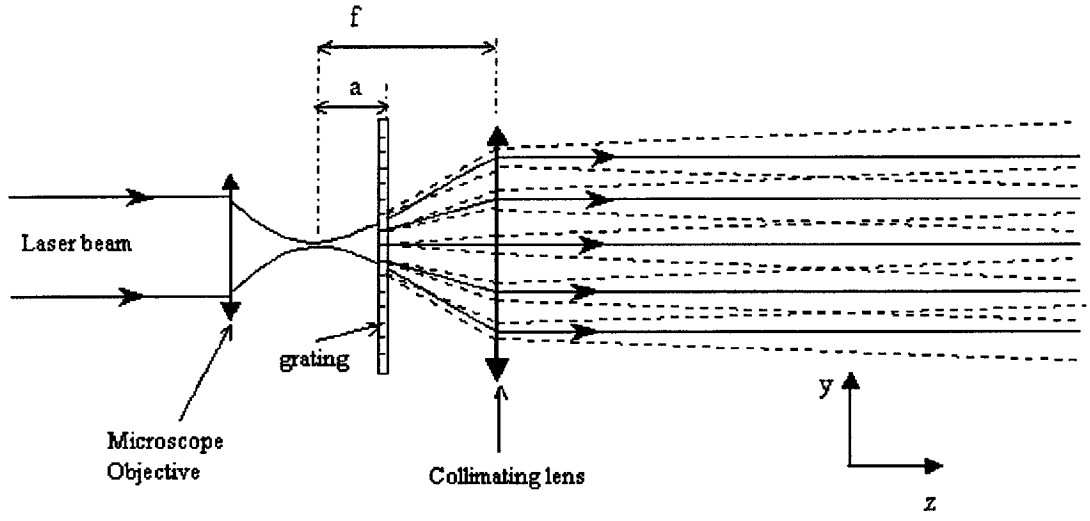

Fig.4.1.1.a. Schematic of the principle of the Grating Projection System.

The out-of-phase patterns were therefore chosen for the experimental characterization. The position of the grating between the centre of the SW and the collimating lens was varied in each case and the successive locations of the pattern illumination along the optical axis were recorded against the ratio between the distance a, from the centre of the SW to the grating, and the focal length f of the lens. Fig.4.1.1.b presents the results for different values of a/f for the lenses of f=15 cm and 20 cm. The labels on the x-axis relate to the number of the patterns observed. From these graphs, we can see that the spacing between two consecutive patterns is constant. The collimation of the diffracted orders was confirmed experimentally by varying the position of the observation screen along the optical axis z in order to characterize their divergence.

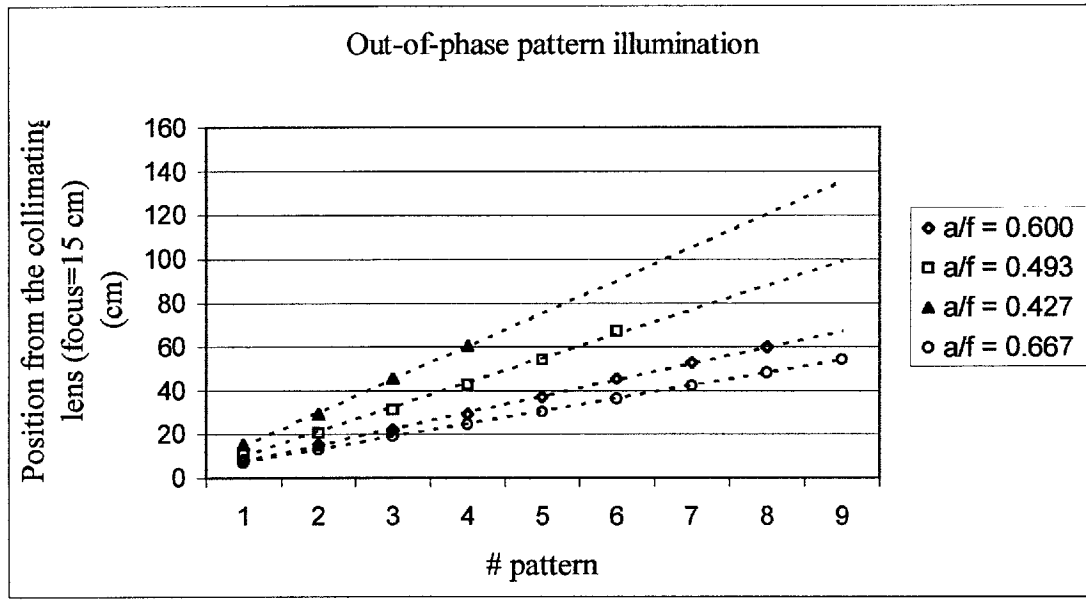

(a)

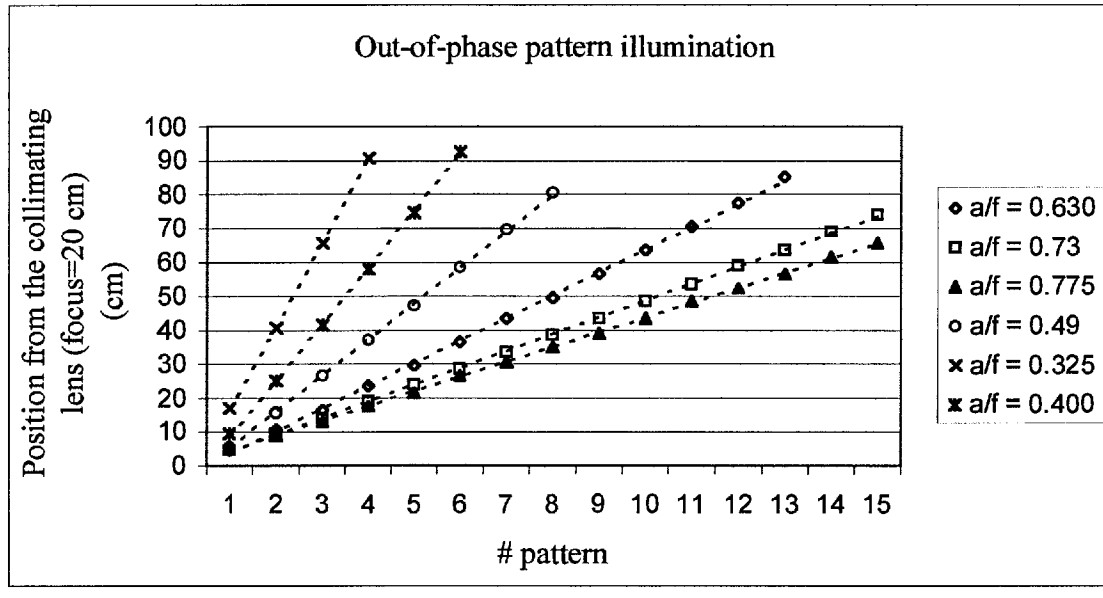

(b)

Fig. 4.1.1.b. Positions of the out-of-phase patterns. (a) f= 15 cm; (b) f= 20 cm.

The angles of the diffracted orders were measured relative to the centre of the collimating lens on the z-axis and are in agreement with geometrical optics theory (cf. fig.4.1.1.c below).

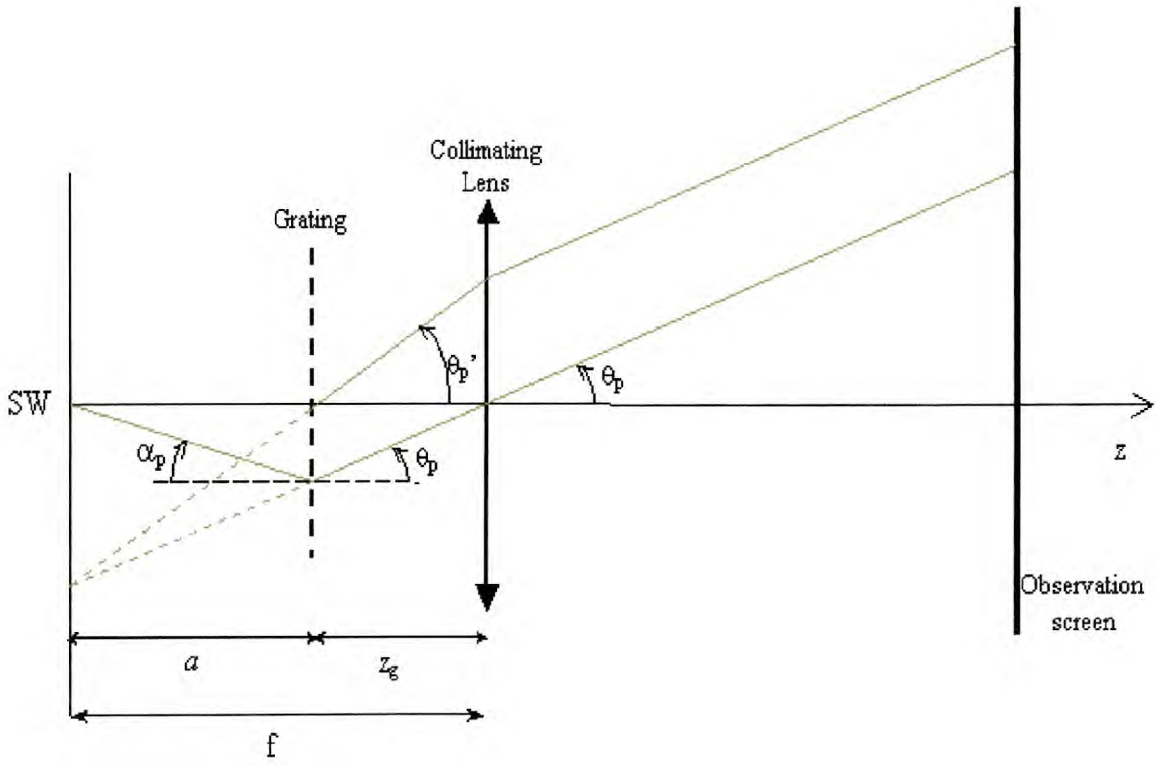

Fig.4.1.1.c. Ray-tracing diagram of a diffracted order.

Fig.4.1.1.d shows the plot of the angles θ_p as a function of a/*f*, for *f*=15 cm. The fact that the diffracted orders are all collimated suggests that diffraction of the SW by the grating creates a set of spherical waves, the virtual centres of which have the same transverse positions on the z-axis, at $z = -f$.

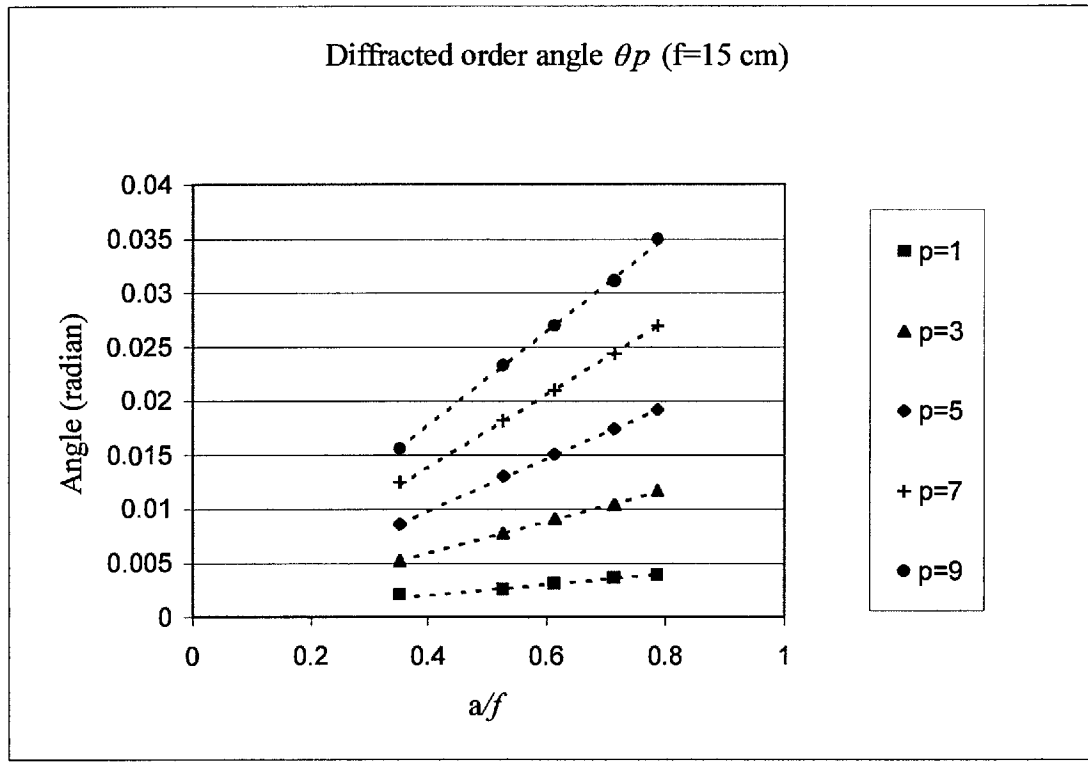

Fig.4.1.1.d . Angles θ_p versus $\frac{a}{f}$.

The experimental characterization of the in-phase and out-of-phase patterns was achieved with a CCD camera of pixel resolution 6.8 μm. The transverse intensity distribution of the patterns was recorded at different positions along the optical axis z. Fig.4.1.1.e below shows in-phase pattern illumination for f = 15 cm and (a) a = 7.4 cm, z = 11.7 cm, (b) a = 10 cm, z = 13.2 cm. The position at which the out-of-phase patterns were recorded is shown in Fig.4.1.1.b.(a). The in-phase patterns were recorded at half way intermediary positions. The non-uniformity of the intensity distributions shown in Fig.4.1.1.e is due to different factors: gaussian intensity distribution of the laser beam, aberrations of the grating and lenses, slight misalignment of the optics. The square-wave profile is clearly seen and degrades at further positions on the optical axis.

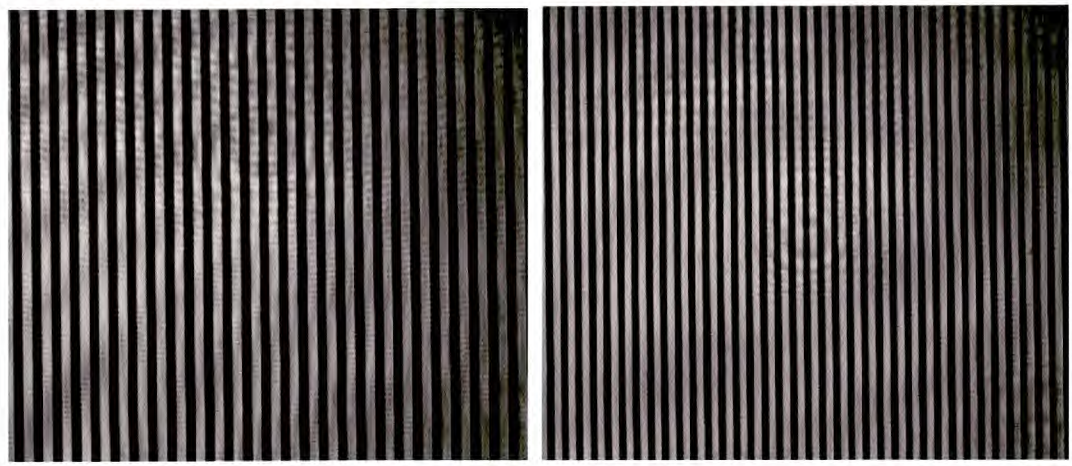

(a) (b)

Fig.4.1.1.e In-phase pattern illumination for f = 15 cm and (a) a = 7.4 cm, (b) a = 10 cm.

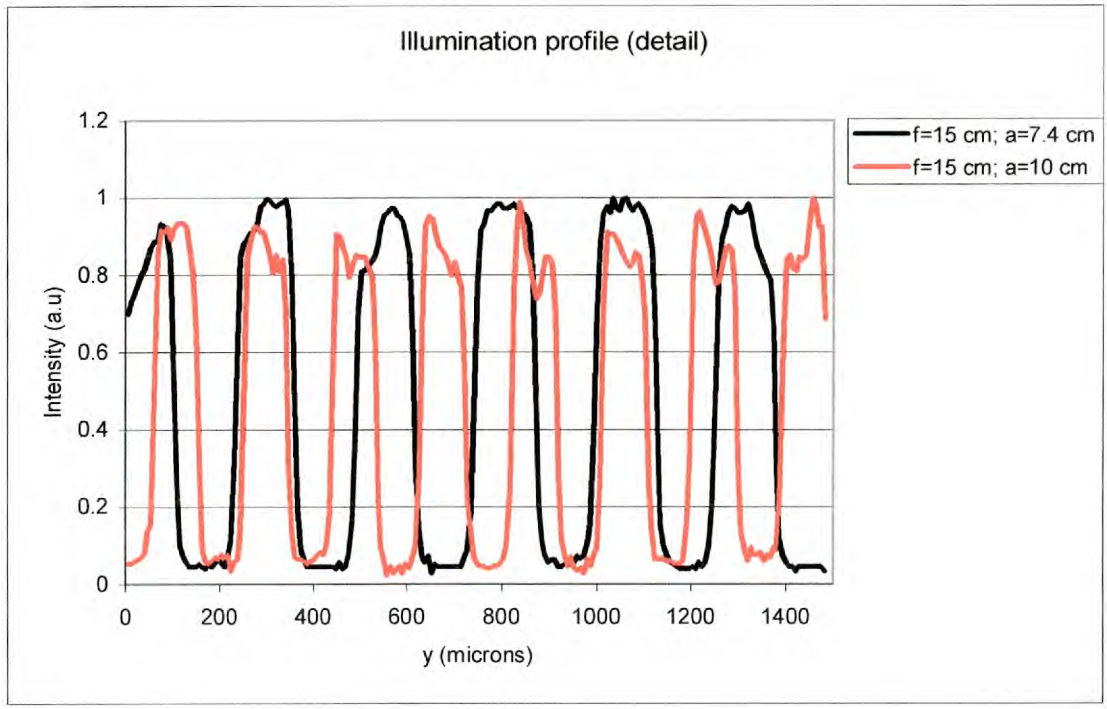

Fig.4.1.1.f. In-phase pattern illumination profile (detail) for f = 15 cm; a = 7.4 cm, and a = 10 cm.

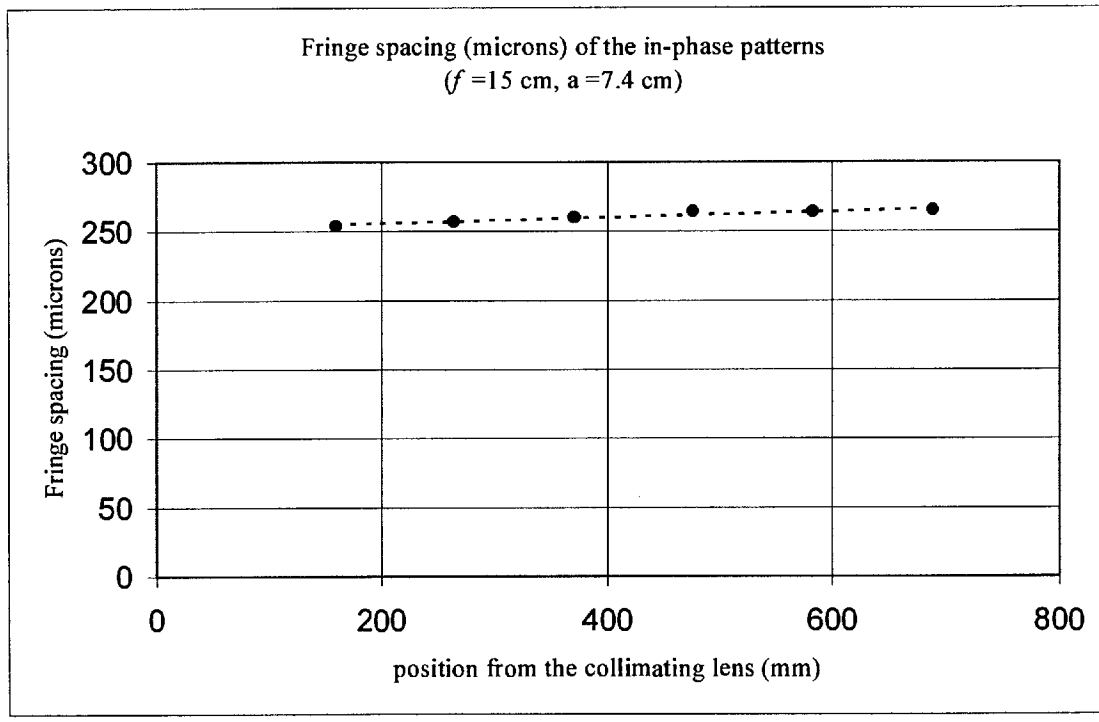

Fig.4.1.1.g. Fringe spacing of successive in-phase patterns (f= 15 cm, a=7.4 cm).

The fringe spacing measurements for each successive position of the in-phase patterns are shown in Fig.4.1.1.g above. We observe that the fringe spacing is not constant over the whole distance due to slightly imperfect collimation of the beam.

4.1.2 Theoretical characterization.

To model this system, we used the theory of diffraction by a concave grating illuminated by a point-like source [4.6], for which the radius of the grating is extended to infinity.

Diffraction by a concave grating illuminated by a point-like source

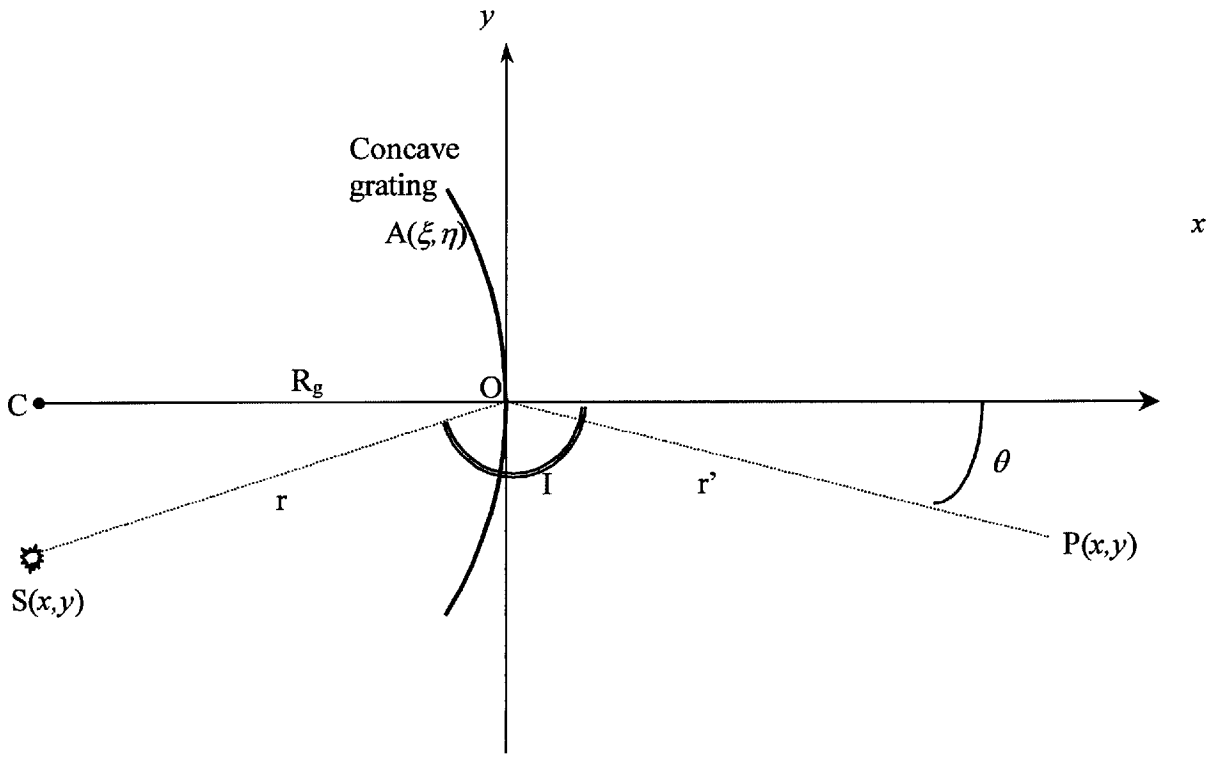

Fig.4.1.2.a. Concave grating treatment.

A(x,y) in fig.4.1.2.a characterize the profile of the grating.

It is shown that the diffraction equation is [4.7]:

$$\eta(\sin I+\sin\theta)-\frac{\eta^2}{2}\left[\left(\frac{\cos^2 I}{r}-\frac{\cos I}{R_g}\right)+\left(\frac{\cos^2\theta}{r'}-\frac{\cos\theta}{R_g}\right)\right]$$
$$-\frac{\eta^3}{2}\left[\frac{\sin I}{r}\left(\frac{\cos^2 I}{r}-\frac{\cos I}{R_g}\right)+\frac{\sin\theta}{r'}\left(\frac{\cos^2\theta}{r'}-\frac{\cos\theta}{R_g}\right)\right]+\ldots=\frac{\eta}{d_g}p\lambda \qquad \text{(Eq.4.1.2.a)}$$

where R_g is the radius of curvature of the concave grating, λ is the wavelength, d_g is the grating step and p is an integer. In our case, R_g is set to infinity (plane grating), so that the terms in $\frac{\cos\theta}{R_g}$ become zero. Furthermore, considering that r and r' are large in comparison with η, we obtain from Eq.4.1.2.a:

$$d_g(\sin I + \sin\theta) = p\lambda \qquad \text{(Eq.4.1.2.b)}$$

which is the well-known grating equation. Thus, the diffraction equation for the case of a plane wave illuminating a grating is the same (to first order approximation) as for the case of a spherical wave. However, we have to notice that in Eq.4.1.2.b the angle I is not constant, and therefore the nature of the diffracted waves will differ from that for plane wave illumination case. It was shown experimentally that these have the same nature as the SW.

As mentioned before (cf. Fig.4.1.1.c and Fig.4.1.1.d), it was established experimentally that the diffracted orders are collimated. Thus we can consider that each order is a spherical wave, the centre of which is located on the same transverse plane as the SW. As shown in Fig.4.1.1.c, the light rays passing through the centre of the lens are not deviated and are incident at an angle θ_p, p being the diffraction order. θ_p' is the p^{th} order angle for I=0. From simple geometrical optics, we can deduce that:

$$\tan(\theta_p) = \frac{a}{f}\tan(\theta_p') \qquad \text{(Eq.4.1.2.c)}$$

According to equation Eq.4.1.2.b, for I=0, we have:

$$\sin\theta_p' = p\frac{\lambda}{d_g} \qquad \text{(Eq.4.1.2.d)}$$

Combining equation Eq.4.1.2.c Eq.4.1.2.d, we obtain:

$$\tan(\theta_p) = \frac{a}{f}\frac{p\frac{\lambda}{d_g}}{\sqrt{1-(p\frac{\lambda}{d_g})^2}} \qquad \text{(Eq.4.1.2.e)}$$

Fig.4.1.2.b. below shows the experimental data compared to the theoretical values obtained using equation Eq.4.1.2.e. The calculated angles differ systematically by +3%

from the experimental data. This is due to the imperfect collimation of the beam, which affected the precision on the position of the grating.

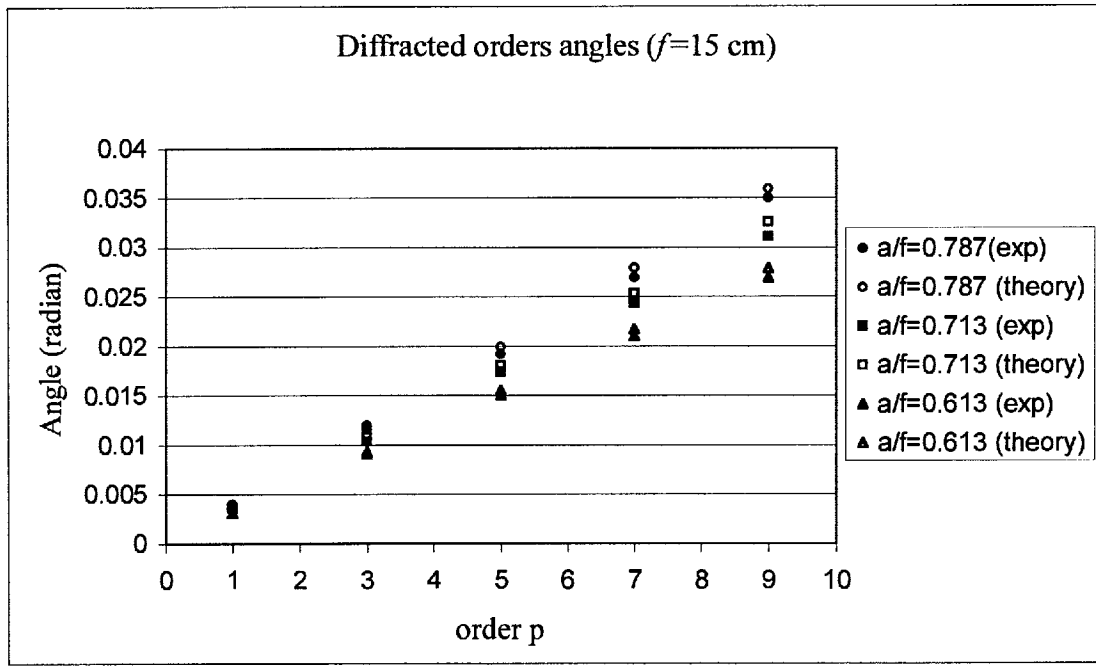

Fig.4.1.2.b. Comparison between experimental data and calculated values of the diffracted orders angles.

It was observed experimentally that the profile of the projected patterns is a truncated magnified square wave (cf.Fig.4.1.1.e). Because the diffracted orders are collimated after the lens, we can approximate each diffracted order as a plane wave with a different orientation angle θ_p, with $p = \pm 1, \pm 2, \pm 3, \ldots$. Thus we can consider each pair of orders and apply a summation on their relative amplitudes to find the resultant intensity distribution.

Let us examine the interference of two plane waves of amplitude 1, $e^{ikz_1}\hat{z}_1$ and $e^{ikz_2}\hat{z}_2$, crossing at the half-angles θ as illustrated in fig.4.1.2.c. The direction z refers to the undiffracted beam, corresponding to p=0.

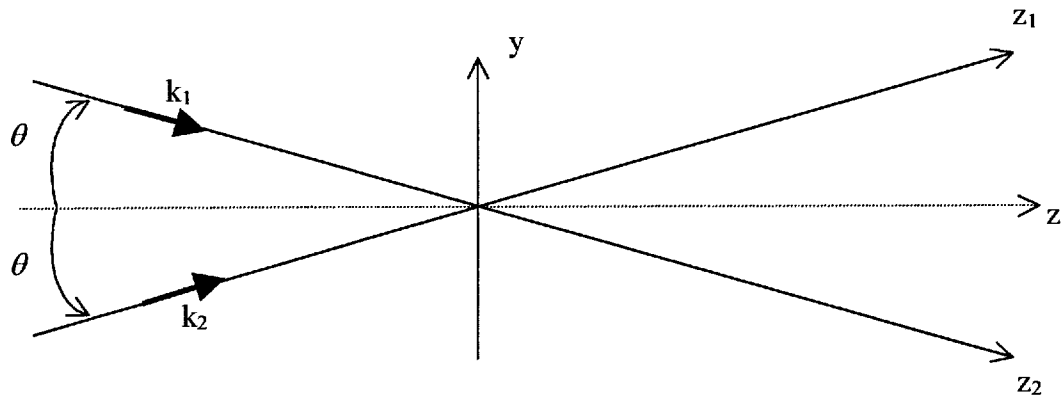

Fig.4.1.2.c . Plane waves crossing at the half-angle θ.

We can write z_1 and z_2 as:

$$\begin{cases} z_1 = z\cos(\theta) - y\sin(\theta) \\ z_2 = z\cos(\theta) + y\sin(\theta) \end{cases} \quad \text{(Eq.4.1.2.f)}$$

and express the resulting amplitude as:

$$E(y,z) = e^{ikz\cos(\theta)}\left\{e^{iky\sin(\theta)} + e^{-iky\sin(\theta)}\right\} = 2e^{ikz\cos(\theta)}\cos(ky\sin(\theta)) \quad \text{(Eq.4.1.2.g)}$$

The intensity is:

$$I(y,z) = |E(y,z)|^2 = 2\{1 + \cos(2ky\sin(\theta))\} \quad \text{(Eq.4.1.2.h)}$$

Here the fringe spacing is given by the following condition, resulting from the interference of the 0^{th} order and the 1^{st} orders (these make an angle θ relatively to each other):

$$2k\lambda_f \sin(\frac{\theta}{2}) = 2\pi \quad \text{(Eq.4.1.2.i)}$$

leading to, assuming θ is very small in our case:

$$\sin(\theta) = \frac{\lambda}{\lambda_f} \quad \text{(Eq.4.1.2.j)}$$

$$\rightarrow \cos(\theta) = \sqrt{1-\frac{\lambda^2}{\lambda_f^2}} \qquad \text{(Eq.4.1.2.k)}$$

We can now rewrite Eq.4.1.2.g as:

$$E(y,z) = 2e^{ikz\sqrt{1-\frac{\lambda^2}{\lambda_f^2}}}\cos(\frac{2\pi y}{\lambda_f}) \qquad \text{(Eq.4.1.2.l)}$$

For a finite series of N pairs of interfering plane waves where the resulting intensity distribution is a square wave, we need to write the amplitude as:

$$E_{total}(y,z) = a_0 e^{ikz} + \sum_{n=1}^{N} 2a_n e^{ikz\sqrt{1-\frac{n^2\lambda^2}{\lambda_f^2}}}\cos(\frac{2n\pi y}{\lambda_f}) \qquad \text{(Eq.4.1.2.m)}$$

where the coefficients a_n are obtained by standard Fourier decomposition of the square wave to be:

$$\begin{cases} a_0 = \frac{1}{2} \\ a_n = \frac{1}{n\pi}\sin(\frac{n\pi}{2}) \quad for\, n = 1,3,5,7... \end{cases} \qquad \text{(Eq.4.1.2.n)}$$

Therefore the field amplitude can be expressed as:

$$E_{total}(y,z) = \frac{1}{2}e^{ikz} + \sum_{n=1}^{N}\frac{2}{n\pi}\sin(\frac{n\pi}{2})e^{ikz\sqrt{1-\frac{n^2\lambda^2}{\lambda_f^2}}}\cos(\frac{2n\pi y}{\lambda_f}) \qquad \text{(Eq.4.1.2.o)}$$

and the intensity:

$$I_{total}(y,z) = \left|E_{total}(y,z)\right|^2 \qquad \text{(Eq.4.1.2.p)}$$

The fringe spacing of the in-phase patterns can be obtained by considering the interference between the 0th and 1st diffracted orders, as these produce the largest fringe pattern with the biggest weight. The corresponding diffraction angle $\theta_{\pm 1}$ is calculated

from Eq.4.1.2.e. The expression for the fringe spacing λ_f is given by the well-known interference formula between two plane waves of monochromatic coherent light:

$$\lambda_f = \frac{\lambda}{2\sin(\frac{\theta_{+1}}{2})} \qquad \text{(Eq.4.1.2.q)}$$

We can compare this fringe spacing with the one previously determined experimentally in the case where f = 15 cm and a = 7.4 cm. We then have θ_{+1} = 0.002498 rad, leading to λ_f = 253.4 μm. This theoretical value differs by less than 0.3 % from the experimental one (cf. Fig.4.1.1.f). However, as mentioned before, the increase of the fringe spacing with distance is due to slightly imperfect collimation.

Similarly, the positions of the in-phase patterns are determined by considering the interference between the 0th, +1st and −1st orders. The expression for the resulting intensity is then:

$$I(x,z) = 1 + 4\cos^2(kx\sin\theta_1) + 4\cos(kx\sin\theta_1)\cos[kz(1-\cos(\theta_1)] \qquad \text{(Eq.4.1.2.r)}$$

The periodicity along the optical axis z is then given by the following condition:

$$kz(1-\cos(\theta_1)) = n\pi$$
$$\Leftrightarrow z = \frac{n\lambda}{2(1-\cos(\theta_1))} \qquad \text{(Eq.4.1.2.s)}$$

We plot in Fig.4.1.2.d the theoretical value of the periodicity of the patterns compared to the experimental data from Fig.4.1.1.b.(b), as a function of $\frac{a}{f}$.

From Eq.4.1.2.e , Eq.4.1.2.q and fig.4.1.2.c above, we see that the fringe spacing and the in-phase pattern positions are contingent on the position of the grating between the microscope objective and the collimating lens. Thus an interdependent relationship exists between the two parameters of the Grating Projection System. Although presenting similar characteristics to the traditional Talbot effect, this system is in fact an

extension of it in the sense that one can set the fringe spacing of the in-phase pattern by adjusting the position of the grating between the collimating lens and the microscope objective.

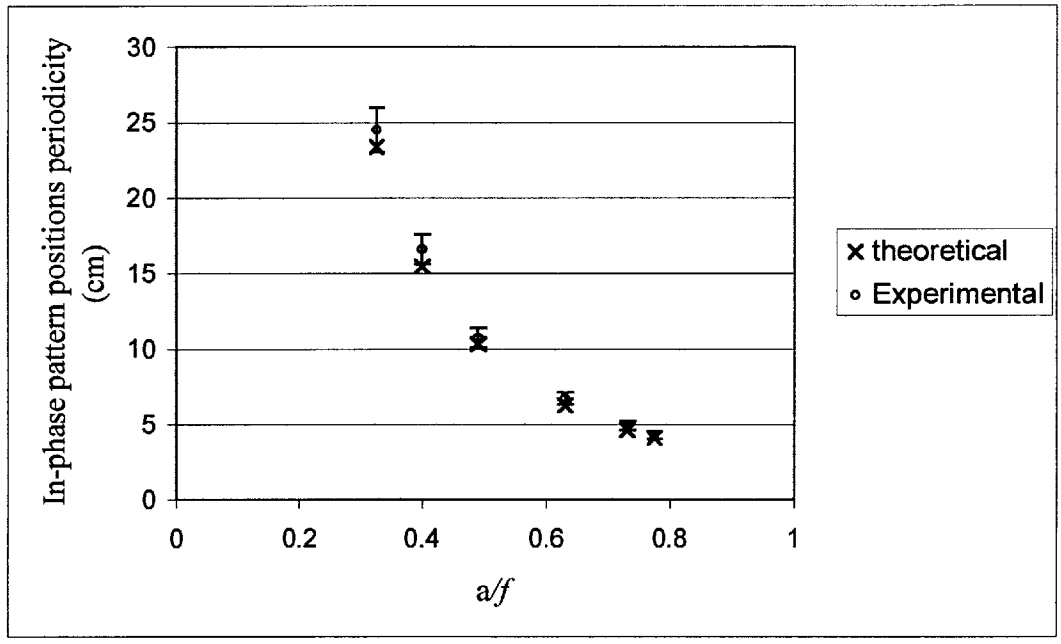

Fig.4.1.2.d. Comparison between theoretical and experimental data of the periodicity of the patterns (f= 15 cm, λ = 633 nm).

4.1.3 Limitations.

The limitations of the Grating Projection System are twofold: a decrease in intensity and a successive degradation of the fringe patterns.

- Loss of intensity

The laser beam used in the GPS is focused through the microscope and collimated by the lens. Therefore a loss of intensity is expected due to its magnification. The initial laser beam intensity I_L is proportional to its power P divided by $\pi\sigma^2$ (σ is

approximated as the radius of the beam; it is in fact the $\frac{1}{e^2}$ beam radius). After expansion of the initial beam, its radius is then $M\sigma$ (M being the magnifying factor of the optical system constituted by the microscope and the collimating lens) leading to an intensity I_L' of the beam:

$$I_L' \propto \frac{P}{\pi\sigma^2 M^2} \qquad \text{(Eq.4.1.3.a)}$$

Therefore the ratio of the two intensities is:

$$\frac{I_L}{I_L'} = M^2 \qquad \text{(Eq.4.1.3.b)}$$

The intensity of the beam has decreased by a factor M^2. The consequence of this reduction of intensity is a limitation in the range of particle sizes detectable. However, as mentioned before, the GPS system allows the user to set the position of the patterns and the fringe spacing by adjusting the grating position, for which only the ratio a/f is significant. Therefore, it is possible to obtain a compromise between the loss of intensity and the number of fringes needed for the experiment. A lower magnifying factor means a smaller beam diameter, therefore a smaller number of observable fringes. Conversely, a smaller beam diameter will lower the maximum distance at which the fringe patterns are clearly observed.

- Successive degradation of the fringes.

We showed in paragraph 4.1.1 that the GPS produces a set of collimated plane waves with a direction at an angle θ_p related to the diffracted order for the grating. Given the magnifying factor M, most orders overlap at $z = 0$ (front of the collimating lens) but then separate out according to θ_p. This means that further along the optical

axis, higher diffracted orders do not participate in the reproduction of the initial structure of the grating. Ultimately, they are all separated and no further interference is observed. This is illustrated in Fig.4.1.3.a below, showing pictures of the beam after the lens at two distances (a) z = 15.9 cm and (b) z = 68.9 cm from the lens. The degradation of the profile is clearly seen in fig.4.1.3.b.

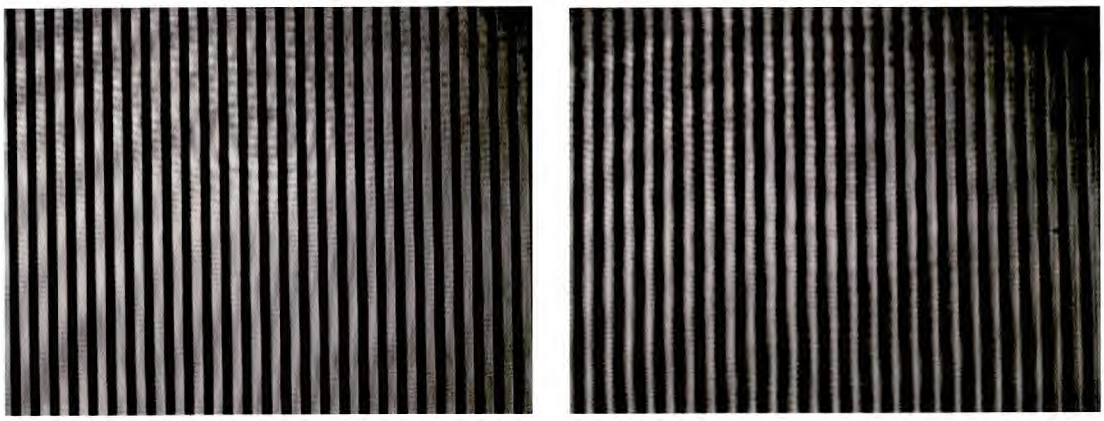

(a) (b)

Fig.4.1.3.a. Beam profile at z = 15.9 cm and z = 68.9 cm from the lens.

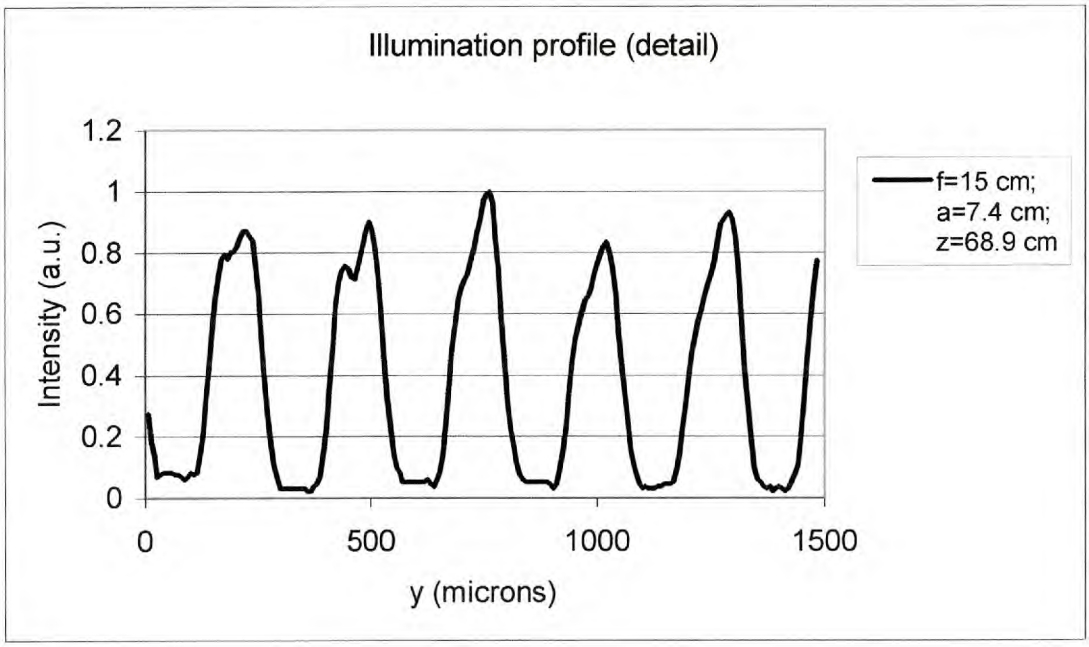

Fig.4.1.3.b. Illumination profile at z = 68.9 cm from the lens.

4.2 Velocity measurements.

Velocity measurements were demonstrated with the set up described in Fig.4.2.a below.

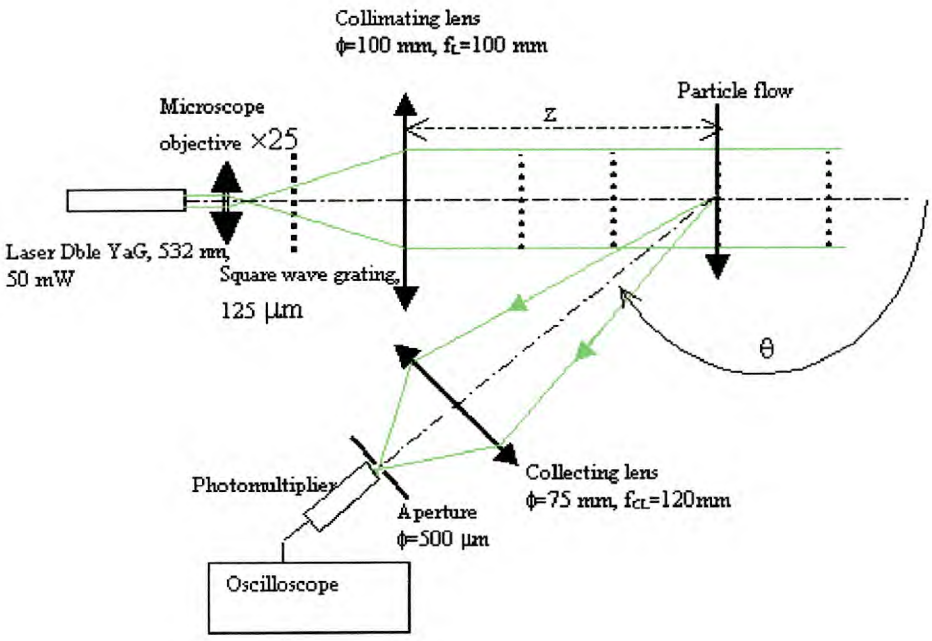

Fig.4.2.a. Optical set up for velocity measurements with the GPS.

The measurements were carried out with a photomultiplier type 9558 operating in its linear range. The angle θ was set to 140°. A Gould 1604 oscilloscope was used to analyse the scattered light signal and compute its Fast Fourier Transform (FFT) with 512 points. The main frequency of the signal was determined by an automated routine integrated within the oscilloscope. The GPS system was set for a fringe spacing of 1.2 mm, allowing the presence of patterns further up to 3 m. Spherical glass Ballotini particles (size distribution 40-90 µm) were blown at 3 positions of the in-phase patterns, namely 15 cm, 130 cm and 300 cm. The maximum velocity achievable in our laboratory

was nearly 20 m/s. The uncertainty on the velocity measurement was determined by the minimum frequency observable in the FFT spectrum, which was around 1 kHz for an average frequency of 13 kHz. Thus an estimation of the error on the velocity measured with the oscilloscope was approximately ±7%. Fig.4.2.b below shows the distributions of the velocity measurements at z = 15 cm, 130 cm and 300 cm.

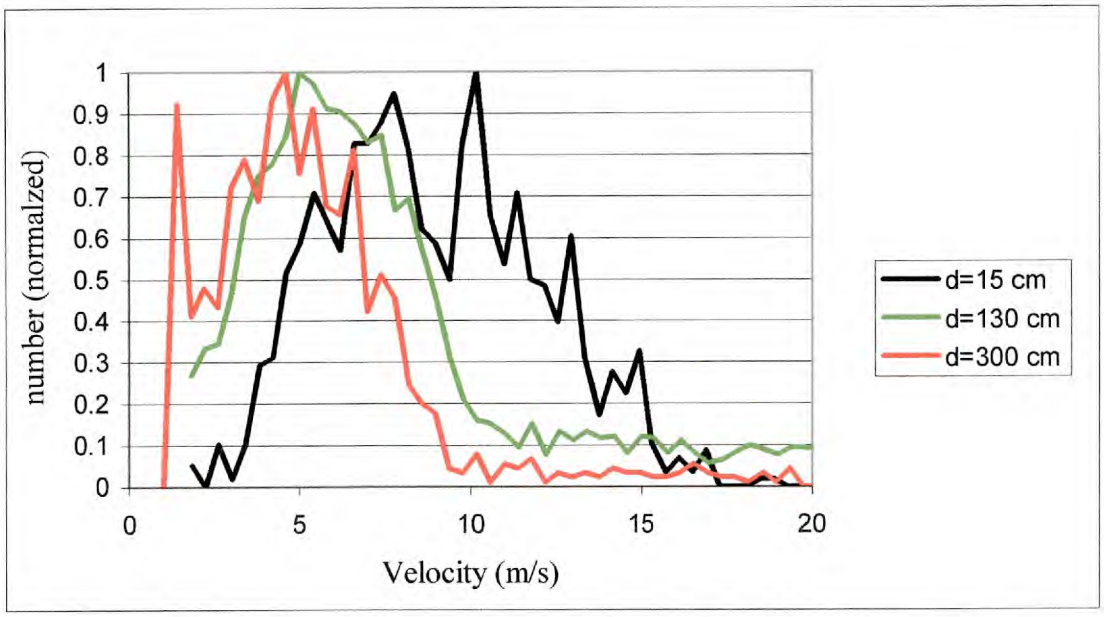

Fig.4.2.b.Distributions of the velocity measurements at z = 15 cm, 130 cm and 300 cm.

In this graph, we see that the velocity distributions are not identical. This was explained by an improper collimation of the GPS. Indeed, for this particular experiment, the main objective was to demonstrate that it is possible to achieve velocity measurements at long distances with the GPS. The fringe spacing was initially set to be 1.2 mm at 15 cm from the collimating lens. We then expect that it will increase with distance, therefore shifting downward the velocity distributions measured at further positions.

Thus it was demonstrated that the GPS provides a suitable means to measure particle velocity. The uncertainty associated with the measurements presented above can be reduced by using a higher FFT resolution. A proper test of the velocity measurement using this technique by comparison with an independent technique is discussed in section 6.3.

5. Investigation of a new sizing technique: The Total Harmonic Distortion (THD) analysis.

5.1. Principle of the technique.

In this method, we use the grating projection system defined in section 4.1 to illuminate the test space with a truncated square wave monochromatic illumination pattern. The scattered light is analysed and the distortion of the truncated square wave signal induced by the particle is measured with the Total Harmonic Distortion (%THD) parameter (described below in section 5.2.). For homogeneous spherical particles of identical refractive index only the size influences the %THD parameter. This relationship between the %THD and the particle size is the object of the investigation that is presented in this section.

5.2. Definition of the %THD parameter.

Let us consider the square wave signal of amplitude 1 and frequency 1 *Hz*, from $t = 0$ s to $t = 20$ s, represented in Fig.5.2.a, and its associated FFT spectrum (512 points) in Fig.5.2.b. The fundamental frequency of the signal is seen at $f_1 = 1$ Hz, and a set of harmonics are also observed. The DC and harmonics amplitudes are well known and are described by the standard Fourier series decomposition of the square wave:

$$\begin{cases} a_0 = \dfrac{1}{2} \\ a_n = \dfrac{1}{n\pi}\sin\left(\dfrac{n\pi}{2}\right) \quad n = 1,2,3... \end{cases} \qquad \text{(Eq.5.2.a)}$$

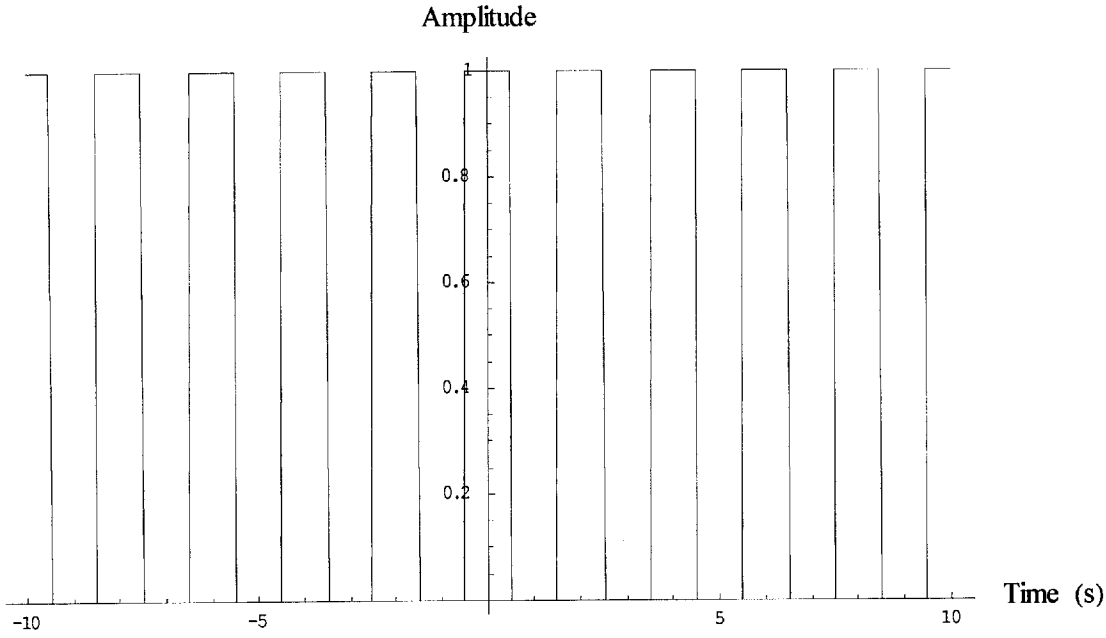

Fig.5.2.a. Square wave signal (amplitude 1, frequency 1 *Hz*).

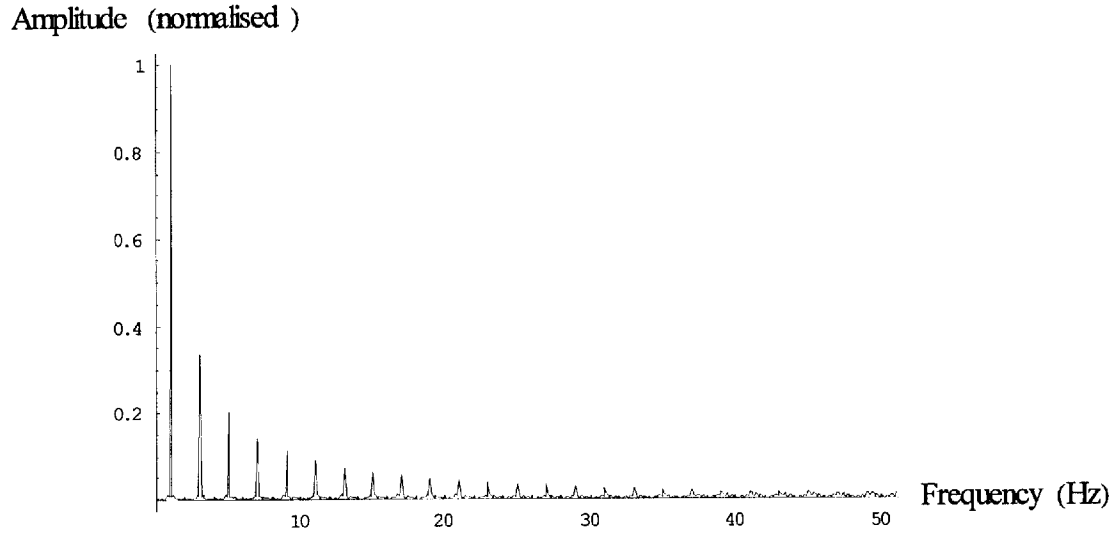

Fig.5.2.b. Normalised FFT spectrum of the square wave signal.

To determine the amount of energy contained in the harmonics of a signal, we use the Total Harmonic Distortion (THD), which is then defined as:

$$THD = \frac{\sqrt{\sum_{n=2}^{\infty} a_n^2}}{a_1} \qquad \text{(Eq.5.2.b)}$$

The THD parameter is then the square root of the ratio of the energy contained in the harmonics and the energy of the fundamental. For practical use, the summation is truncated to N, the number of significant harmonics to be analysed in the signal:

$$THD = \frac{\sqrt{\sum_{n=2}^{N} a_n^2}}{a_1} \qquad \text{(Eq.5.2.c)}$$

In this thesis, we will express the Total Harmonic Distortion in a percentage form more suitable for purpose of clarity, which is:

$$\%THD = 100\frac{\sqrt{\sum_{n=2}^{N} a_n^2}}{a_1} \qquad \text{(Eq.5.2.d)}$$

5.3. Experimental configuration.

5.3.1 Optical set up.

The optical set up used to measure the influence of particle size on the %THD parameter was set identically to the one described previously in Fig.4.2.a. The position of the grating was adjusted to obtain a 200 μm fringe spacing in the test space. The diameter and focal length of the collecting lens were 10 cm. The collection angle was

set to 140°. The test space was 13 cm from the collimating lens of the GPS, a distance at which the square wave pattern was very well resolved.

5.3.2 Automated detection system.

The automated detection system consisted of an electronic part and a data acquisition device, controlled with the data acquisition software LABVIEW 5.1 through a laptop computer.

Electronic system

The frequency bandwidth necessary for THD measurements is a function of the particle velocity, the fringe spacing and the number of harmonics N to be analysed. With an average speed of 1 *m/s*, the frequency generated by a particle crossing a 200 μm fringe pattern is 5 *kHz*. Assuming a maximum number of harmonics $N = 20$, we then have 100 *kHz* as the maximum frequency to be analysed. The amplifier that we used had a cut-off frequency of 500 *kHz*, so we always analysed the full spectrum of the scattered light signal necessary for the THD measurements.

Data acquisition with Labview 5.1

Labview 5.1 software is widely used in industry and research. It is based on a graphical data flow programming language called *G*, which simplifies scientific computation, process monitoring and test and measurement applications.

The visual interface (*VI*) allows the user to control a data acquisition device. In a *VI*, a graphical programming structure called *diagram* organizes the acquisition/display of

data on the Front Panel. In this experiment, the data were acquired using a data acquisition device called DAQCARD 5102, from National Instruments. Its physical characteristics are given in Table 5.3.2.a below.

Analog Inputs	Resolution	Sampling Rate	Input Range
2	8 bits	20 Msamples/s	±0.05 V to ±5 V

Table 5.3.2.a. Physical characteristics of the DAQCARD 5102.

In order to automate the measurements, we created a *VI* which triggered the data acquisition, computed the THD parameter of the acquired signal, stored the processed data and finally displayed them in the form of a distribution. A flow chart of the graphical interface is presented in Fig.5.3.2.a.

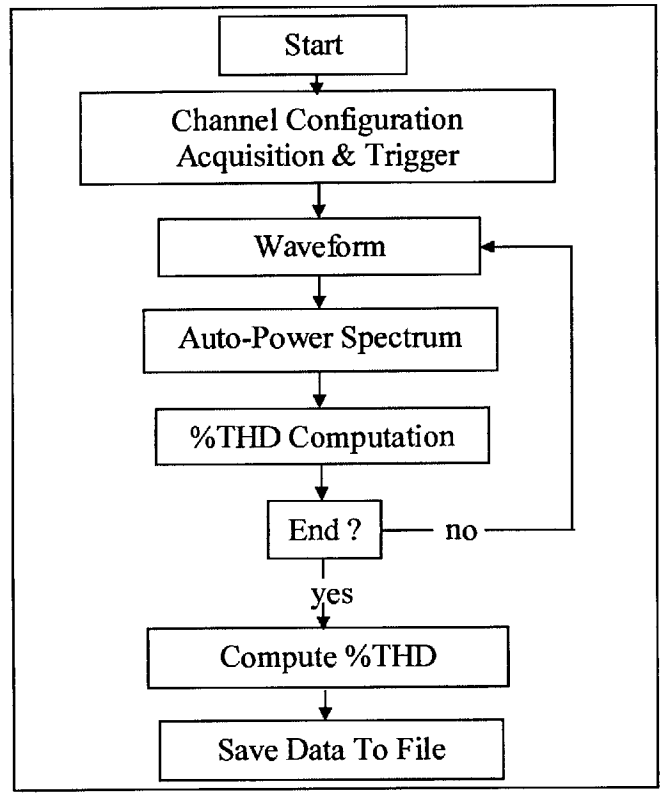

Fig.5.3.2.a. Synoptic of the *VI*'s graphical interface.

The "Auto-Power Spectrum" is a built-in *VI* from Labview that computes the single-sided power spectrum of a signal. This is required before using the "%THD" *VI* that computes the value of the %THD of the acquired signal. The program was then terminated by the user with a simple boolean function that directly triggered the computation of the %THD distribution and its recording to a file.

5.3.3 Particle samples.

To study the variation of the %THD parameter experimentally, we used 6 samples of certified spherical monodisperse particles. These were made of Polymethylmetacrylate (PMMA), of refractive index m=1.52 + i0. The mean size and standard deviation of each sample is listed in Table 5.3.3.a below.

Sample number	1	2	3	4	5	6
Mean size(μm)	20.00	25.33	40.15	49.82	73.77	103.53
Standard deviation (μm)	± 0.34	± 0.59	± 0.76	± 0.87	± 2.09	± 1.68

Table 5.3.3.a. Monodisperse particles size distributions characteristics

5.4. Measurement of %THD versus particle size.

The monodisperse PMMA particles were elutriated with a fluidised bed and blown individually through the test space, perpendicular to the fringes. All the optical parts were enclosed to ensure a minimum optical noise level.

5.4.1. Noise influence on the %THD measurements.

To evaluate an appropriate signal-to-noise ratio for the %THD measurements, we ran simulations for a square wave signal with Labview 5.1. In this the original signal

was mixed with a white noise source (WNS) of variable amplitude. The %THD was then computed. For each noise level of the WNS, 100 samples were simulated and their mean value and standard deviation were calculated. Fig.5.4.1.a. below shows the results of the simulation. The mean %THD (calculated with Labview 5.1) is plotted as a function of the signal-to-noise ratio (SNR). The error bars represents the standard deviation of each sample.

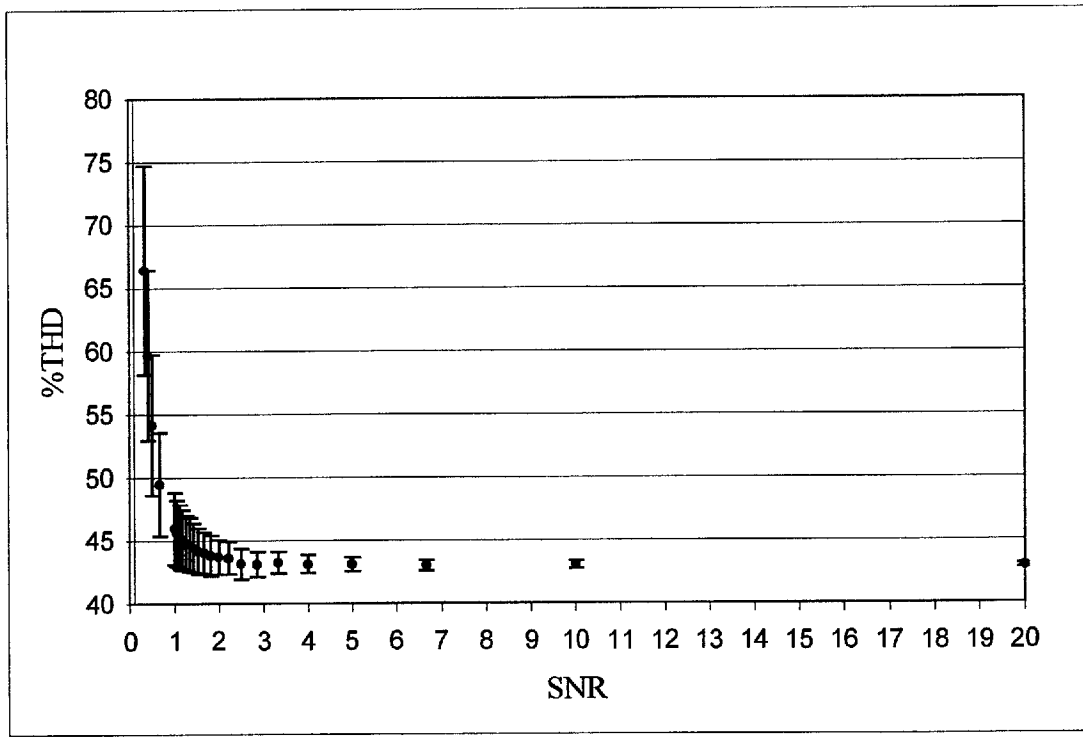

Fig.5.4.1.a. Simulation of %THD measurements of a square wave+WNS, in function of the SNR.

From these simulations, we see that a SNR superior to 3 is a sufficient condition to validate the %THD measurements. This condition was satisfied in all measurements, for which the SNR was approximately 10.

5.4.2. Experimental results of %THD measurements.

Table 5.4.2.a shows the results obtained for the measurements of the %THD from the monodisperse samples presented in Table 5.3.3.a. For each sample, we took 3 sets of 500 values, corresponding to 500 particles. From these 3 sets, we calculated the mean values and the standard deviations of the distributions by applying a gaussian fit. The details of the eighteen %THD measurements distributions are shown in Appendix I. Fig.5.4.2.a below shows the same results, plotted as a function of the respective sample mean size. The errors bars represent the standard deviations of the %THD distributions.

5.4.3. Interpretation.

From the results presented in Fig.5.4.2.a. below, we can conclude that a correlation exists between the %THD value of the sample and its mean size in the size range 20-40 μm. The results for samples #1, #2 and #3 indicate a downward trend. Further than 40 μm, the %THD value is contained between 26% and 32% and appears to be stationary.

The standard deviations of each sample are around the value 2% of the %THD, which accounts for 50% of the %THD mean value fluctuations. This variation cannot be caused by the acquisition process, as the SNR was greater than 10. Also, the sample size distributions having a standard deviation of approximately 2%, the downward trend from sample #1, #2 and #3 cannot be the cause for such discrepancy. It is therefore sensible to assume that the standard deviation values are caused by the scattering process itself. This is studied in section 5.5.

Sample # (mean size μm)	Set	#1	#2	#3
1	%THD mean	32.76	33.49	33.27
20.00	%THD std.dev.	±3.49	±3.26	±3.3
2	%THD mean	31.44	31.95	32.94
25.33	%THD std.dev.	±2.07	±2.1	±2.11
3	%THD mean	29.4	29.59	29.32
40.15	%THD std.dev.	±1.93	±1.95	±1.6
4	%THD mean	29.49	30.00	30.17
49.82	%THD std.dev.	±1.72	±2.54	±2.7
5	%THD mean	28.69	28.97	28.6
73.77	%THD std.dev.	±1.87	±1.71	±1.87
6	%THD mean	27.42	28.79	28.52
103.53	%THD std.dev.	±1.51	±1.52	±1.56

Table 5.4.2.a. %THD measurements results.

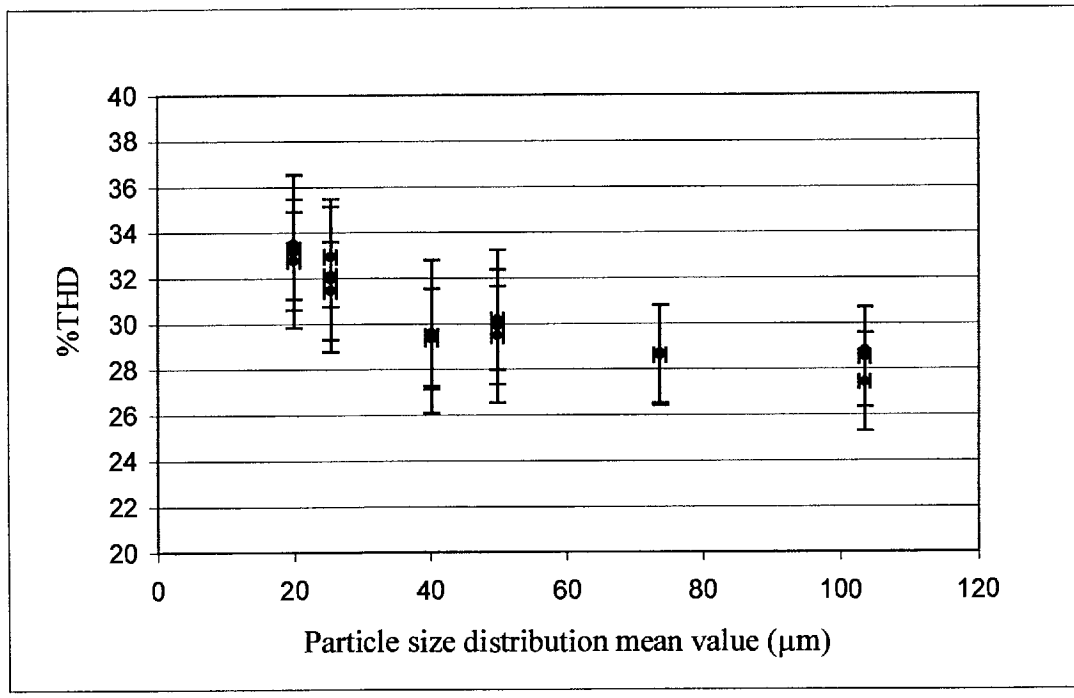

Fig.5.4.2.a. %THD measurements results as a function of particle size distribution mean value.

5.5. Modelling the THD.

We described the Grating Projection System (GPS) in section 4.1 in which the output beam consisted in a set of plane waves interfering together to produce a truncated square wave pattern illumination at certain positions. To treat rigorously the problem of scattering of such illumination by spherical particles, we need to consider the amplitudes scattered by each of the plane waves. By applying a summation of these amplitudes, we can then determine the intensity of the light scattered in any direction. The Mie theory is an exact solution to the problem of scattering of a plane wave by a spherical particle; the detailed treatment can be found in [5.1]. A brief summary is presented in section 5.5.1. At the end of the modelling process, the %THD is obtained from the exact Fourier analysis of the scattered light intensity variation. Thus the expression obtained for the %THD parameter is an exact solution for the case of homogeneous spherical particles.

5.5.1. Scattering theory for monochromatic square wave illumination.

The plane of reference is taken according to the directions of propagation of the incident and scattered fields (c.f Fig.5.5.1.a). We then have for the components of the scattered field [5.2]:

$$\begin{cases} E_l = E_0 \dfrac{e^{ikr}}{-ikr}\cos(\phi)S_{22}(\theta) \\ E_r = E_0 \dfrac{e^{ikr}}{-ikr}\sin(\phi)S_{11}(\theta) \end{cases} \qquad \text{(Eq.5.5.1.a)}$$

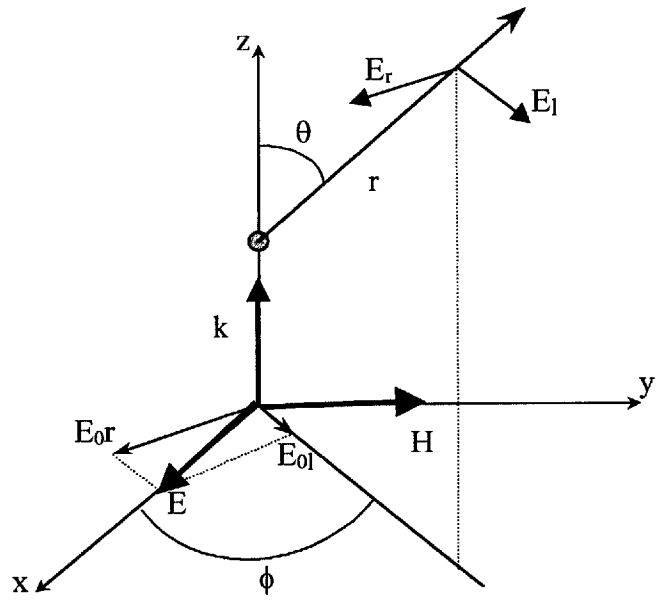

Fig.5.5.1.a.Spherical and Cartesian coordinates reference system.

Where

$$\begin{cases} S_{11}(\theta) = \sum_{p=1}^{\infty} \frac{2p+1}{p(p+1)} \{a_p \tau_p(\cos\theta) + b_p \pi_p(\cos\theta)\} \\ S_{22}(\theta) = \sum_{p=1}^{\infty} \frac{2p+1}{p(p+1)} \{b_p \tau_p(\cos\theta) + a_p \pi_p(\cos\theta)\} \end{cases} \quad \text{(Eq.5.5.1.b)}$$

note : -π_p and τ_p are combinations of Legendre functions.

-a_p and b_p are combinations of spherical Bessel and Hankel functions of the size parameter χ.

$S_{11}(\theta)$ and $S_{22}(\theta)$ are elements of the amplitude scattering matrix [5.2].

As shown previously in Eq.4.1.2.o, the GPS generates an electric field $E_{total}(y,z)$ incident on the particle travelling in the y-direction, described as:

$$E_{total}(y,z) = \frac{1}{2} e^{ikz} + \sum_{n=1}^{N} \frac{1}{n\pi} \sin(\frac{n\pi}{2}) e^{ikz\cos(\gamma_n)} (e^{ky\sin(\gamma_n)} + e^{-ky\sin(\gamma_n)}) \quad \text{(Eq.5.5.1.c)}$$

Eq.5.5.1.c accounts for a set of plane waves incident in the (y,z) plane, each of them having an angle of incidence γ_n relatively to the z-axis. Therefore, the angle ϕ will have different values ϕ_n for each incident plane wave. We can then express these angles ϕ_n as a function of the initial spherical coordinates and the incidence angle. This is illustrated in Fig.5.5.1.b below.

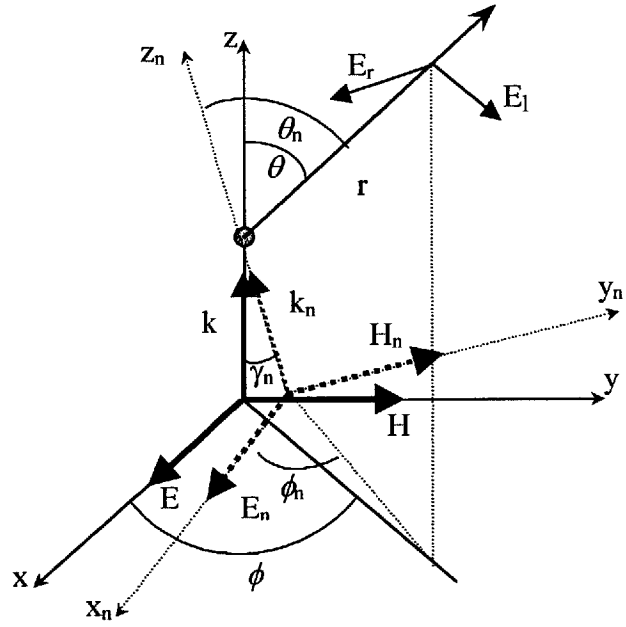

Fig.5.5.1.b. Determination of the angle ϕ_n.

It can be shown (c.f. Appendix II.) that:

$$\begin{cases} \sin(\theta_n)\cos(\phi_n) = \sin(\theta)\cos(\phi) \\ \sin(\theta_n)\sin(\phi_n) = \sin(\theta)\sin(\phi)\cos(\gamma_n) - \cos(\theta)\sin(\gamma_n) \\ \cos(\theta_n) = \cos(\theta)\cos(\gamma_n) + \sin(\theta)\sin(\phi)\sin(\gamma_n) \end{cases} \quad \text{(Eqs.5.5.1.d)}$$

Combining Eq.5.5.1.d(1) and Eq.5.5.1.d(2) gives:

$$\phi_n = Arc\tan\left(\frac{\sin(\theta)\sin(\phi)\cos(\gamma_n) - \cos(\theta)\sin(\gamma_n)}{\sin(\theta)\cos(\phi)}\right) \quad \text{(Eq.5.5.1.e)}$$

and Eqs.5.5.1.d(3) is rearranged as:

$$\theta_n = Arc\cos(\cos(\theta)\cos(\gamma_n) + \sin(\theta)\sin(\phi)\sin(\gamma_n)) \quad \text{(Eq.5.5.1.f)}$$

$$\text{Note: } \begin{cases} \theta = 0 \Rightarrow \begin{cases} \phi_n \to \frac{\pi}{2} \\ \theta_n = \gamma_n \end{cases} \\ \phi = \frac{\pi}{2} \Rightarrow \phi_n = \pm\frac{\pi}{2} \end{cases}$$

Having determined the angles ϕ_n and θ_n, we can now express the total amplitude of the scattered field in the scattering plane coordinates (l,r) at any angular position (θ, ϕ) (the scattering coefficients $S_{11}(\theta)$ and $S_{22}(\theta)$ are only a function of θ):

$$\begin{cases} E_l(\theta,\phi,y,z) = -\frac{i}{k} e^{-ikr+i\omega t} \left(\frac{1}{2} e^{ikz} \cos(\phi_0) S_{22}(\theta_0) + \right. \\ \qquad \sum_{n=1}^{\infty} \frac{1}{n\pi} \sin\left(\frac{n\pi}{2}\right) e^{ikz\sqrt{1-\frac{n^2\lambda^2}{\lambda_f^2}}} \left(e^{ky\sin(\gamma_n)} \cos(\phi_n) S_{22}(\theta_n) \right. \\ \qquad\qquad \left. + e^{-ky\sin(\gamma_n)} \cos(\phi_{-n}) S_{22}(\theta_{-n})\right)\Big)\hat{l} \\ E_r(\theta,\phi,y,z) = -\frac{i}{k} e^{-ikr+i\omega t} \left(\frac{1}{2} e^{ikz} \sin(\phi_0) S_{11}(\theta_0) + \right. \\ \qquad \sum_{n=1}^{\infty} \frac{1}{n\pi} \sin\left(\frac{n\pi}{2}\right) e^{ikz\sqrt{1-\frac{n^2\lambda^2}{\lambda_f^2}}} \left(e^{ky\sin(\gamma_n)} \sin(\phi_n) S_{11}(\theta_n) \right. \\ \qquad\qquad \left. + e^{-ky\sin(\gamma_n)} \sin(\phi_{-n}) S_{11}(\theta_{-n})\right)\Big)\hat{r} \end{cases}$$

(Eqs.5.5.1.g)

The resulting intensity is then:

$$I_{total}(\theta,\phi,y,z) = \left|E_l(\theta,\phi,y,z)\right|^2 + \left|E_r(\theta,\phi,y,z)\right|^2 \qquad \text{(Eq.5.5.1.h)}$$

Eq.5.5.1.h was calculated with Fortran77 and its validity was checked by considering that the intensity scattered by a particle with a radius a very small compared to the fringe spacing λ_f should reproduce a square wave profile, as the phase variation of the light scattered inside the particle is very small.

The following parameters were chosen for these calculations: $\begin{cases} z = 0\,m \\ \lambda = 0.5\,\mu m \\ \lambda_f = 100\,\mu m \\ m = 1.52 + 0i \\ \theta = 10^\circ \\ \phi = 10^\circ \end{cases}$

Fig.5.5.1.c below is the intensity variation (a.u.) of the light scattered by a 0.01 μm radius particle crossing the truncated square wave pattern illumination. For these calculations, we considered only 10 diffracted orders, which explains the small ripples at the edges.

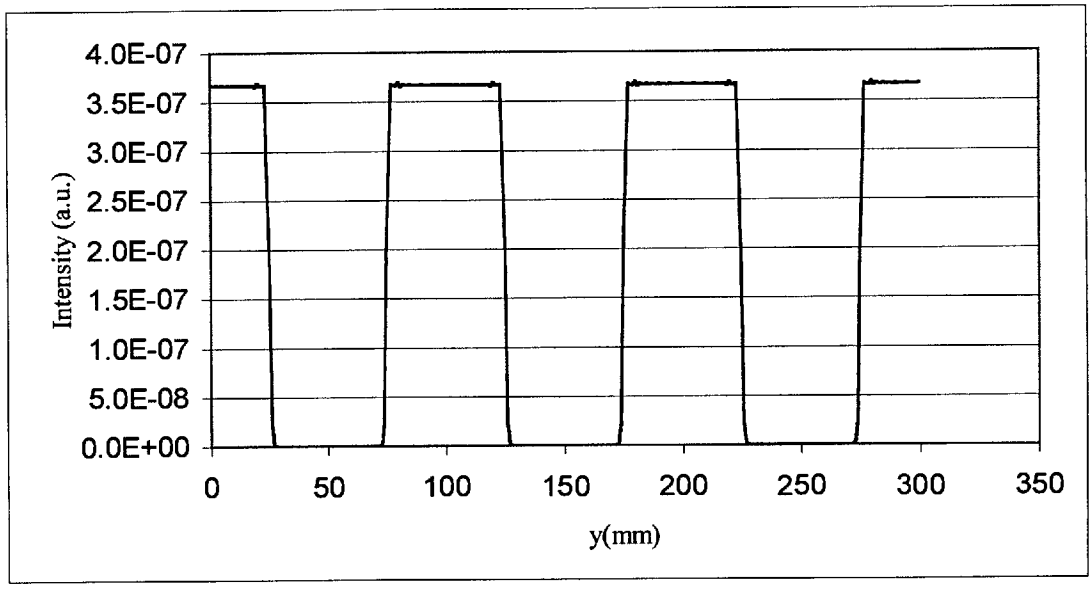

Fig.5.5.1.c. Calculated intensity variation of the light scattered by a 0.01 μm particle crossing the 100 μm fringe pattern.

5.5.2. %THD theory.

The theoretical modelling of the %THD is based on the determination of the harmonic weights of the distorted square wave intensity variation represented in the Fourier space. Each incident plane wave generates a scattered field. Being coherent, these waves will all interfere to produce an intensity distribution, the profile of which is a distorted square wave along an axis parallel to the diffraction grating lines. Each pair of the 2N interfering beams produces a spatial intensity variation which participates in creating the distorted square wave. The %THD, as described in Eq.5.2.d, takes into

account the harmonic weights, which correspond to the spatial intensity variation described previously. In the following treatment, we consider that the scattered field $E_{sca}(\theta,\phi,y,z)$ can be written as:

$$E_{sca}(\theta,\phi,y,z=0)=\sum_{n=-N}^{N}E_n^{(0)}e^{iky\sin(\gamma_n)}f_n(\theta,\phi) \qquad \text{(Eq.5.5.2.a)}$$

Where $E_n^{(0)}$ is the nth incident field amplitude and $\sin(\gamma_n)=\frac{n\lambda}{\lambda_f}$. The term $e^{ikz\sqrt{1-\frac{n^2\lambda^2}{\lambda_f^2}}}$ is taken at $z=0$, to simplify the calculations. Indeed, for the %THD calculations, we need to consider the amplitude of the harmonics of the signal, which are the same for any y. The position $z=0$ corresponds to an in-phase pattern.

The complex scattering function is obtained from Eq.5.5.1.g:

$$f_n(\theta,\phi)=\cos(\phi_n)S_{22}(\theta_n)\hat{l}+\sin(\phi_n)S_{11}(\theta_n)\hat{r} \qquad \text{(Eq.5.5.2.b)}$$

To determine the harmonic weights, we write the scattered intensity:

$$\begin{aligned}I_{sca}(\theta,\phi,y,z=0)&=\left|\sum_{n=-N}^{N}E_n^{(0)}e^{iky\sin(\gamma_n)}f_n(\theta,\phi)\right|^2\\&=\sum_{n=-N}^{N}(E_n^{(0)})^2|f_n(\theta,\phi)|^2\\&\quad+\sum_{n=-N}^{N}\sum_{\substack{m=-N\\m\neq n}}^{N}E_n^{(0)}E_m^{(0)}e^{iky(\sin(\gamma_n)-\sin(\gamma_m))}f_n(\theta,\phi)f_m^*(\theta,\phi)\end{aligned} \qquad \text{(Eq.5.5.2.c)}$$

We can transform the double summation by considering that each pair of interfering beams has a symmetric equivalent (with different complex scattering function):

$$I_{sca}(\theta,\phi,y,z=0) = \sum_{n=-N}^{N}(E_n^{(0)})^2|f_n(\theta,\phi)|^2 + \sum_{n=-N}^{N}\sum_{m>n}^{N}\{ E_n^{(0)}E_m^{(0)}(e^{iky(\sin(\gamma_n)-\sin(\gamma_m))}f_n(\theta,\phi)f_m^*(\theta,\phi) + e^{-iky(\sin(\gamma_n)-\sin(\gamma_m))}f_m(\theta,\phi)f_n^*(\theta,\phi)) \}$$

(Eq.5.5.2.d)

To simplify the formal calculation, let us assign:

$$\begin{cases}\omega_{nm} = k(\sin(\gamma_n)-\sin(\gamma_m)) \\ f_n = f_n(\theta,\phi) \\ f_m = f_m(\theta,\phi)\end{cases}$$

and rewrite Eq.5.5.2.d as:

$$I_{sca}(\theta,\phi,y,z=0) = \sum_{n=-N}^{N}(E_n^{(0)})^2|f_n|^2 + \sum_{n=-N}^{N}\sum_{m>n}^{N}E_n^{(0)}E_m^{(0)}(\cos(\omega_{nm}y)(f_nf_m^* + f_n^*f_m) + i\sin(\omega_{nm}y)(f_nf_m^* - f_n^*f_m))$$

(Eq.5.5.2.e)

Further, let us write:

$$\begin{cases}f_nf_m^* + f_n^*f_m = 2(\mathrm{Re}(f_n)\mathrm{Re}(f_m) + \mathrm{Im}(f_n)\mathrm{Im}(f_m)) = \alpha_{nm}(\theta,\phi) \\ f_nf_m^* - f_n^*f_m = -2i(\mathrm{Re}(f_n)\mathrm{Im}(f_m) - \mathrm{Im}(f_n)\mathrm{Re}(f_m)) = -i\beta_{nm}(\theta,\phi)\end{cases}$$

(Eq.5.5.2.f)

we can then express Eq.5.5.2.d as:

$$I_{sca}(\theta,\phi,y,z=0) = \sum_{n=-N}^{N}(E_n^{(0)})^2|f_n|^2 + \sum_{n=-N}^{N}\sum_{m>n}^{N}E_n^{(0)}E_m^{(0)}(\alpha_{nm}(\theta,\phi)\cos(\omega_{nm}y) + \beta_{nm}(\theta,\phi)\sin(\omega_{nm}y))$$

(Eq.5.5.2.g)

In the following calculations, we will consider only the dynamic part of $I_{sca}(\theta,\phi,y,z=0)$, which is the second part of Eq.5.5.2.g, as the first summation is a DC component and therefore does not participate in the intensity variation.

The power incident $P(y)$ on the collecting lens is then the double integral of $I_{sca}(\theta,\phi,y,z=0)$ over θ and ϕ:

$$P(y)=\sum_{n=-N}^{N}\sum_{m>n}^{N}C_{nm}\iint_{(\theta,\phi)}\{\alpha_{nm}(\theta,\phi)\cos(\omega_{nm}y)+\beta_{nm}(\theta,\phi)\sin(\omega_{nm}y)\}\sin(\theta)\,d\theta\,d\phi \qquad \text{(Eq.5.5.2.h)}$$

with $C_{nm}=E_n^{(0)}E_m^{(0)}$

The integrand can be written as:

$$\alpha_{nm}(\theta,\phi)\cos(\omega_{nm}y)+\beta_{nm}(\theta,\phi)\sin(\omega_{nm}y)=A_{nm}\cos(\omega_{nm}y+\varphi_{nm}) \qquad \text{(Eq.5.5.2.i)}$$

$$\text{with}\begin{cases}A_{nm}=\sqrt{\alpha_{nm}^2(\theta,\phi)+\beta_{nm}^2(\theta,\phi)}\\ \tan(\phi_{nm})=-\dfrac{\beta_{nm}(\theta,\phi)}{\alpha_{nm}(\theta,\phi)}\end{cases}$$

leading to the final form of the incident power $P(y)$:

$$P(y)=\sum_{n=-N}^{N}\sum_{m>n}^{N}C_{nm}\iint_{(\theta,\phi)}A_{nm}\cos(\omega_{nm}y+\varphi_{nm})\sin(\theta)\,d\theta\,d\phi \qquad \text{(Eq.5.5.2.j)}$$

The computation of the %THD with Labview is achieved by passing the signal through the Auto-Power Spectrum *VI* (c.f. paragraph 5.3.2), which output is:

$$\frac{FFT(P(y))FFT(P(y))^*}{(N_p)^2}$$

where N_p is the number of points used in the FFT.

The equivalent formulation of the FFT is the Fourier integral, which applied to $P(y)$ is:

$$\mathsf{F}\{P(y)\} = \sum_{n=-N}^{N}\sum_{m>n}^{N}\frac{C_{nm}}{\sqrt{2\pi}}\iint_{(\theta,\phi)}A_{nm}\int_{-\infty}^{+\infty}\cos(\omega_{nm}y+\varphi_{nm})e^{i\omega y}dy\sin(\theta)\,d\theta\,d\phi$$

(Eq.5.5.2.k)

we have:

$$\int_{-\infty}^{+\infty}\cos(\omega_{nm}y+\varphi_{nm})e^{i\omega y}dy = \pi\left\{e^{i\varphi_{nm}}\delta(-\omega_{nm}-w)+e^{-i\varphi_{nm}}\delta(\omega_{nm}-w)\right\}$$

Physically, only $\delta(-\omega_{nm}-w)$ is possible (m>n, $\rightarrow$ $\omega_{nm}<0$, see Eq.5.5.2.m below), therefore we can express $\mathsf{F}\{P(y)\}$ as:

$$\mathsf{F}\{P(y)\} = \sqrt{\frac{\pi}{2}}\sum_{n=-N}^{N}\sum_{m>n}^{N}C_{nm}\iint_{(\theta,\phi)}A_{nm}e^{i\varphi_{nm}}\sin(\theta)\,d\theta\,d\phi\delta(-\omega_{nm}-\omega) \qquad \text{(Eq.5.5.2.l)}$$

We remark that the Dirac function $\delta(-\omega_{nm}-\omega)$ characterize physically the harmonics locations. These are expressed in function of the difference *n-m* (c.f. Eq.4.1.2.j, replacing θ by γ_n):

$$\omega_{nm} = \frac{2\pi}{\lambda}(\sin(\gamma_n)-\sin(\gamma_m))$$

$$\Rightarrow\omega_{nm} = \frac{2\pi}{\lambda_f}(n-m) \qquad \text{(Eq.5.5.2.m)}$$

However, an inclination factor has to be considered relatively to the half angle of the beams. The projected $\omega_{nm}^{(p)}$ then becomes:

$$\omega_{nm}^{(p)} = \frac{2\pi}{\lambda}(n-m)\cos(\frac{\gamma_n+\gamma_m}{2}) \qquad \text{(Eq.5.5.2.n)}$$

Nevertheless, in our case the diffraction angles are very small, leading to the following approximation:

$$\cos(\frac{\gamma_n + \gamma_m}{2}) \approx 1$$

We know that:

$$\mathsf{F}\{P(y)\}\mathsf{F}^*\{P(y)\} = \mathrm{Re}^2(\mathsf{F}\{P(y)\}) + \mathrm{Im}^2(\mathsf{F}\{P(y)\}) \qquad \text{(Eq.5.5.2.o)}$$

so we can write the real and imaginary parts squared taking into account the dependence of ω_{nm} with $(n\text{-}m)$:

$$\begin{cases} \mathrm{Re}^2[\mathsf{F}\{P(y)\}] = \frac{\pi}{2}\sum_{j=1}^{2N}\sum_{n=-N}^{N-j}\sum_{m=-N}^{N-j} C_{n,n+j}C_{m,m+j}J_{n,n+j}(\theta_0,\phi_0)J_{m,m+j}(\theta_0,\phi_0) \\ \qquad\qquad *\delta(-\omega_{n,n+j}-\omega)\delta(-\omega_{m,m+j}-\omega) \\ \mathrm{Im}^2[\mathsf{F}\{P(y)\}] = \frac{\pi}{2}\sum_{j=1}^{2N}\sum_{n=-N}^{N-j}\sum_{m=-N}^{N-j} C_{n,n+j}C_{m,m+j}K_{n,n+j}(\theta_0,\phi_0)K_{m,m+j}(\theta_0,\phi_0) \\ \qquad\qquad *\delta(-\omega_{n,n+j}-\omega)\delta(-\omega_{m,m+j}-\omega) \end{cases} \qquad \text{(Eq.5.5.2.p)}$$

with:

$$\begin{cases} J_{n,n+j}(\theta_0,\phi_0) = \iint_{(\theta,\phi)} A_{n,n+j}\cos(\varphi_{n,n+j})\sin(\theta)\,d\theta\,d\phi \\ K_{n,n+j}(\theta_0,\phi_0) = \iint_{(\theta,\phi)} A_{n,n+j}\sin(\varphi_{n,n+j})\sin(\theta)\,d\theta\,d\phi \end{cases} \qquad \text{(Eq.5.5.2.q)}$$

Where (θ_0, ϕ_0) are the mean integration angles.

Thus the auto power spectrum of $P(y)$ is defined as:

$$\mathsf{F}\{P(y)\}\mathsf{F}^*\{P(y)\} = \frac{\pi}{2}\sum_{j=1}^{2N}\sum_{n=-N}^{N-j}\sum_{m=-N}^{N-j} C_{n,n+j}C_{m,m+j}\{J_{n,n+j}(\theta,\phi)J_{m,m+j}(\theta,\phi) + K_{n,n+j}(\theta,\phi)K_{m,m+j}(\theta,\phi)\}*\delta(-\omega_{n,n+j}-\omega) \qquad \text{(Eq.5.5.2.r)}$$

we can write the fundamental frequency amplitude a_1 for $n=0, m=\pm 1$ using Eq.5.5.2.r above, and the total energy contained within the harmonics as (recalling Eq.5.5.2.d):

$$a_1^2 = \frac{\pi}{2}\sum_{n=-1}^{0}\sum_{m=-1}^{0} C_{n,n+1}C_{m,m+1}\{J_{n,n+1}(\theta,\phi)J_{m,m+1}(\theta,\phi) + K_{n,n+1}(\theta,\phi)K_{m,m+1}(\theta,\phi)\}*\delta(-\omega_{n,n+1}-\omega) \qquad \text{(Eq.5.5.2.s)}$$

$$\sum_{p=2}^{N} a_p^2 = \frac{\pi}{2} \sum_{j=2}^{2N} \sum_{n=-N}^{N-j} \sum_{m=-N}^{N-j} C_{n,n+j} C_{m,m+j} \left\{ J_{n,n+j}(\theta,\phi) J_{m,m+j}(\theta,\phi \right. \\ \left. + K_{n,n+j}(\theta,\phi) K_{m,m+j}(\theta,\phi) \right\}^* \delta(-\omega_{n,n+j} - \omega) \\ + \frac{\pi}{2} \sum_{\substack{n=-N \\ n\neq -1,0}}^{N-1} \sum_{\substack{m=-N \\ m\neq -1,0}}^{N-1} C_{n,n+1} C_{m,m+1} \left\{ J_{n,n+1}(\theta,\phi) J_{m,m+1}(\theta,\phi) \right. \\ \left. + K_{n,n+1}(\theta,\phi) K_{m,m+1}(\theta,\phi) \right\}^* \delta(-\omega_{n,n+1} - \omega)$$

(Eq.5.5.2.t)

And finally we obtain the expression for the %THD:

$$\%THD = 100 \sqrt{\frac{\sum_{p=2}^{N} a_p^2}{a_1^2}} \qquad \text{(Eq.5.5.2.u)}$$

which is identical to Eq.5.2.d, but rewritten here for sake of clarity.

This concludes the theoretical treatment of the %THD.

5.5.3. FORTRAN77 program structure.

The calculations of the %THD were performed using FORTRAN77. They were based on Eq.5.5.2.q which provided the theoretical basis for the calculation of the harmonic weights. In this program, the scattered electric field was first computed using Mie theory, for each incident diffraction order at discrete values of (θ, ϕ) within the integration aperture. The Mie theory algorithm was provided by Prof. A.R. Jones from Imperial College, London. The database containing the information of $\vec{E}_n(\theta,\phi)$ was then stored. The second part of the program retrieved this information in order to calculate the expressions of Eq.5.5.2.q:

$$\begin{cases} J_{n,n+j}(\theta_0,\phi_0) = \iint_{(\theta,\phi)} A_{n,n+j}\cos(\varphi_{n,n+j})\sin(\theta)\,d\theta\,d\phi \\ K_{n,n+j}(\theta_0,\phi_0) = \iint_{(\theta,\phi)} A_{n,n+j}\sin(\varphi_{n,n+j})\sin(\theta)\,d\theta\,d\phi \end{cases}$$

Afterwards, the terms a_1 and $\sum_{p=2}^{N} a_p^2$ from Eq.5.5.2.s and Eq.5.5.2.t were calculated and the %THD was deduced using Eq.5.5.2.u. The FORTRAN77 code of this program is given in Appendix III.

5.5.4. Results.

The following parameters were used for the %THD calculations in the FORTRAN77 program structure:

$$\begin{cases} \text{WVL} = 532\,nm & (\equiv \lambda) \\ \text{FRNG} = 200\,\mu m & (\equiv \lambda_f) \\ \text{RIP} = (1.52, 0) & (\equiv m) \\ N = 5 & \\ \text{ANGLEINIT} = 140^\circ & (\equiv \theta_0) \\ \text{ANGLEINIP} = 90^\circ & (\equiv \phi_0) \\ \text{DELTA} = 5^\circ & \end{cases}$$

The integration parameter DSPC (c.f. Appendix II, 145), which accounts for the average number of divisions within a lobe of the scattering pattern, was proven to give good convergence for the %THD when set to 20. However, this constrained the integration angle parameter DELTA to 5°. Beyond this value, the number of integration steps outweighed the memory capacity of the UNIX station we used for these calculations, at particle diameters larger than 100 μm. However, it was verified that the difference between DELTA= 5° and DELTA= 15° for small sizes was not significant. We therefore assumed DELTA= 5° to be a valid parameter for our calculations to be

comparable to the experiments presented in paragraph 5.4.2. The results of these calculations are presented in Fig.5.5.4.a below.

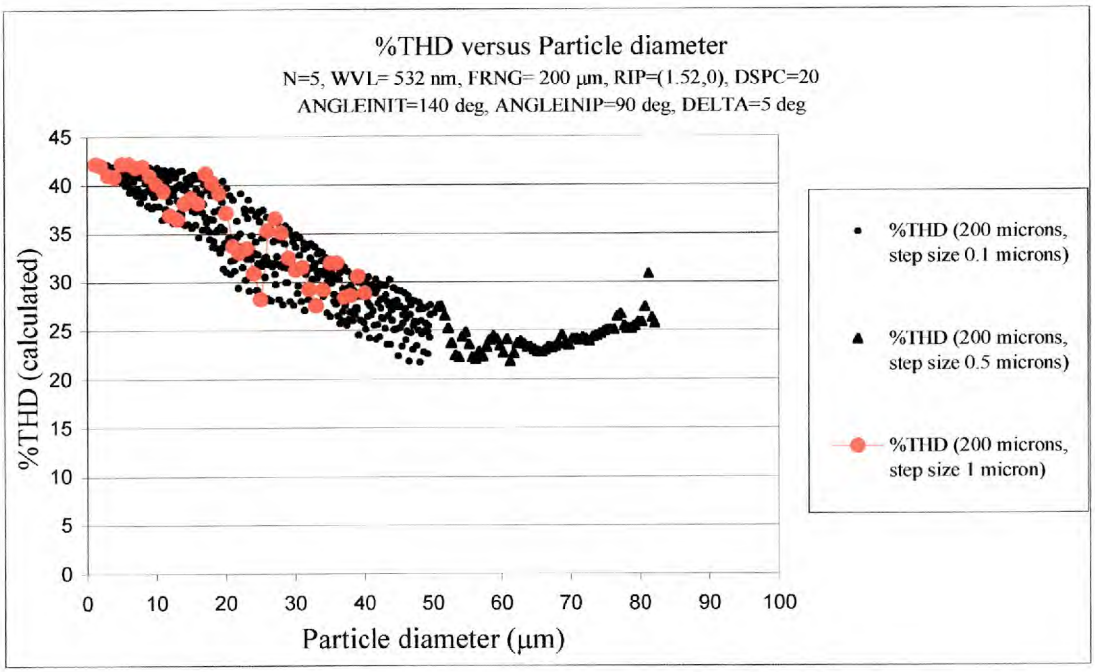

Fig.5.5.4.a. %THD versus particle diameter – FORTRAN77 calculations.

In this graph, two parts can be distinguished (black dots and black triangles). The first part of the %THD, ranging from 0 to 50 µm, was calculated with a step size of 0.1 µm. At around 50 µm, we had to reduce the step size to 0.5 µm, as the calculation time was too long. After 80 µm, one point was calculated in approximately 30 hours.

From the %THD variation up to 50 µm, we can see that it oscillated quite strongly relatively to size. Further than 50 µm, these oscillations were reduced. In order to determine if these oscillations were a genuine effect due to the nature of the %THD parameter or due to calculations errors, we plotted on the same graph the %THD from 1 µm to 40 µm with a step size of 1 µm (red dots on Fig.5.5.4.a). We observed that

the oscillations are still present. We can see also from Fig.5.5.4.b below which shows a zoom of the %THD variation in Fig.5.5.4.a between 20 μm and 40 μm, that the oscillation frequency changed with the step size (0.1 μm in Fig.5.5.4.b). If we now compare these oscillations with the behaviour of the %THD for a size superior to 50 μm (c.f. Fig.5.5.4.a), for which the step size is then 0.5 μm, we do not observe any more oscillations, but instead an almost linear upward trend. This suggest that the oscillatory nature of the %THD parameter was genuine and not a calculation artefact.

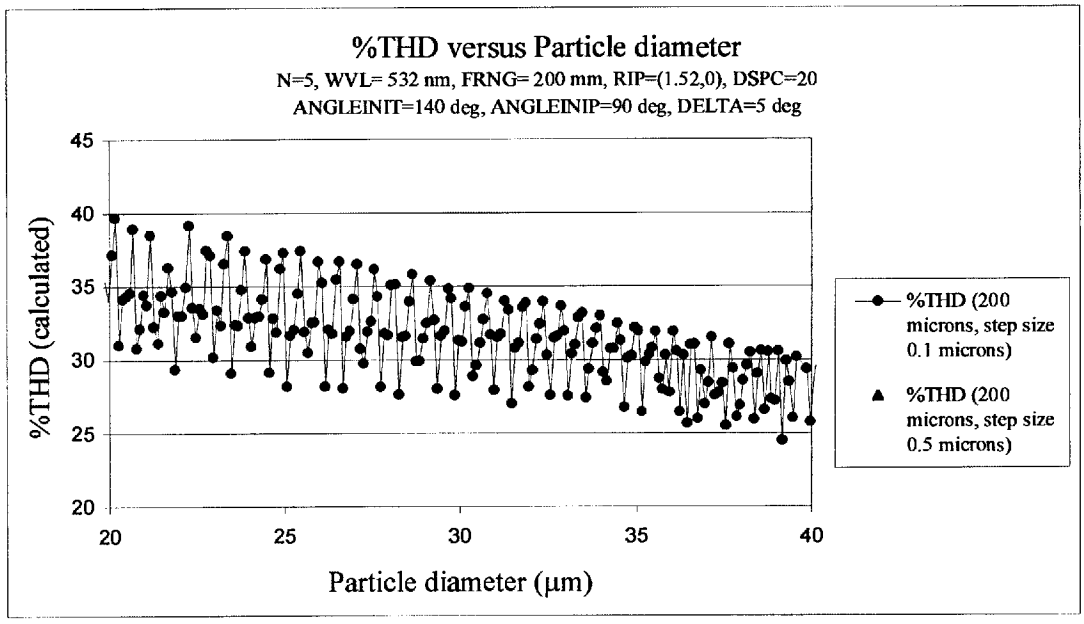

Fig.5.5.4.b. %THD versus particle diameter (20 μm to 40 μm)
-FORTRAN77 calculations.

From Fig.5.5.4.a, we can determine the average amplitude of the %THD oscillations to be approximately 7% . This constitutes 20% of the mean value. For example, at around a particle size of 30 μm, the %THD mean value is 31% and the %THD oscillates between 27% and 34%.

Fig.5.5.4.c below compares the theoretical calculations of the %THD with the experimental data points obtained with the monodisperse particle samples.

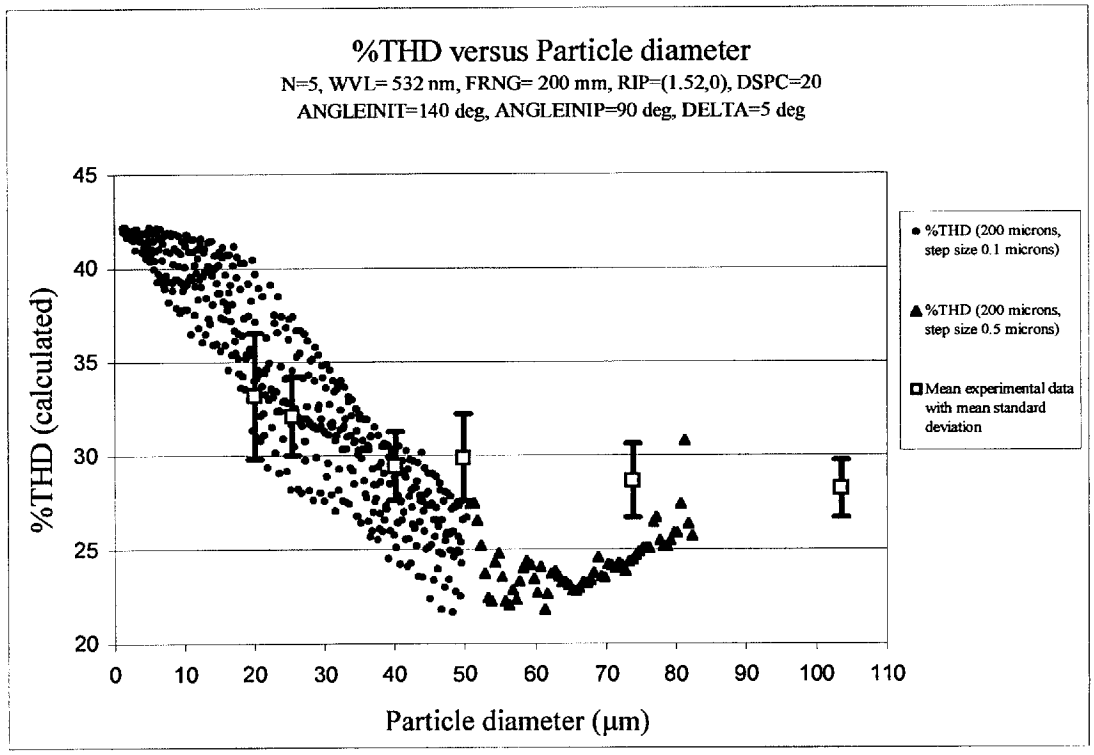

Fig.5.5.4.c. %THD versus particle diameter and experimental data points (mean values and mean standard deviations) -FORTRAN77 calculations.

It can be seen from this graph that the first three experimental points fall approximately within the predicted value of the %THD. The amplitude of the oscillations from 0 μm to 50 μm can be considered to be maximum given the step size of 0.1 μm. If we compare the mean amplitude at each corresponding experimental point, we remark as well that the standard deviations are in agreement with the spread of the calculated %THD values (the standard deviation of the distributions were obtained by applying a gaussian fit).

Above 50 μm, the experimental data points do not fall within the expected range of %THD valued. Additionally, the limitations of the computing process did not allow the region above 82 μm to be explored theoretically. However an extension of the %THD

trend between 60 μm and 80 μm suggest that the experimental %THD value for the monodisperse particle sample #6 would fall within that trend.

5.5.5. Limitations.

The limitations of this method are numerous, in view of the experimental results correlated with the theoretical calculations. The %THD theory being exact from the point of view of calculus, computing errors would appear to be a potential cause to explain the discrepancy of these calculations. However between 50 μm and 60 μm the general trend of the %THD is inverted, making the computing error assumption dubious. To check this possibility, we ran other calculations with 4 different values for the parameter FRNG, which sets the value of the fringe spacing of the light pattern illuminating the spherical particle. The step size was set to 1 μm and the calculations were performed up to 58 μm. The results are presented in Fig.5.5.5.a (the dashed lines do not represent the calculations, but are used to show its variation more clearly). From this graph we note that the %THD variation is the same for each value of FRNG. This was expected as the %THD theory explained in paragraph 5.5.2 shows that the harmonic weights are function of the scattering functions of the particle and of the phases of the incident diffracted orders (considered as plane waves). The result of using a different fringe spacing is then to simply affect, with a corresponding weight, the trend of the %THD variation with respect to particle diameter. This phenomenon could be seen as an advantage, as one can observe on Fig.5.5.a that the amplitude of the oscillations of the %THD decreases with increasing fringe spacing. However, the

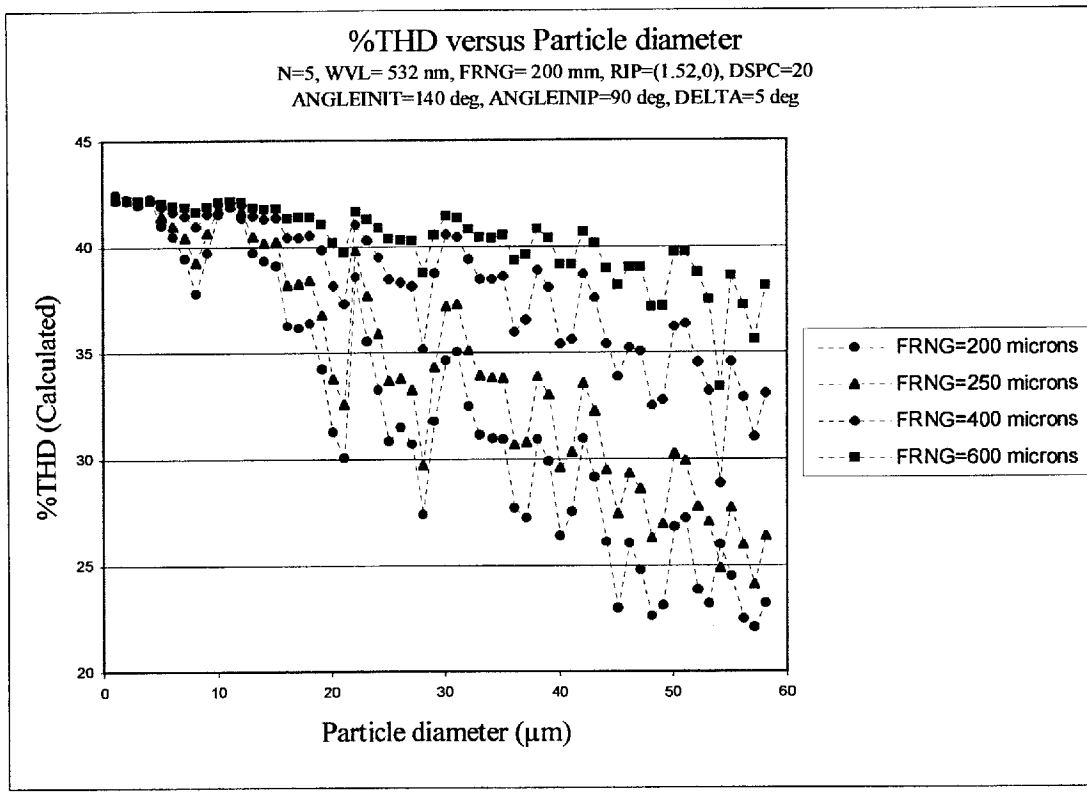

Fig.5.5.5.a. Comparison of %THD variation for different fringe spacing.

associated trend decreases as well. On one hand, the uncertainty on the %THD value would be reduced, but on the other hand the error on the particle diameter would be augmented. Therefore increasing the fringe spacing would not change the measurement errors of this method. Nevertheless, if one was to cope with the uncertainty of this sizing technique, then increasing the fringe spacing would certainly be an advantage in order to expand the range of the downward %THD trend.

Six samples to test this technique were obviously not enough to characterize such a system properly. The cost of monodisperse particle samples, as well as their availability were an obstacle to complete this study in depth. However, a controlled droplet generator that allows the user to produce individual water droplet within the size range

of the %THD measurements has been considered for use. This would constitute a project in itself, where it would then be possible to investigate more precisely the relationship between the weight of each diffracted order and its influence on the %THD variation. Having already proven a correlation between the %THD and the particle diameter within 20 μm and 50 μm, the study of a new parameter defined on the basis the %THD might reveal a more subtle relationship with the size.

Since the %THD method was proven too problematic and insensitive, an alternative method was explored. This is the object of the following section 6.

6. An alternative technique based on intensity measurements.

The scattering of a monochromatic plane wave by homogeneous spherical particles has been solved exactly and is described by the Mie theory. The mathematical formulation of this theory has been presented by authors such as Bohren and Huffman [5.1], Van de Hulst [6.1] and Kerker [6.2]. From this formulation, diverse light scattering instruments have been designed, aiming at measuring the velocity, size and refractive index of particles. Nowadays, the most widely used instruments are those based on the Phase Doppler Anemometry (c.f. literature 1.1). With this method, one relies on the measurement of the phase difference between two or more light scattering signals at different angles. Other methods such as Pulse Displacement Technique (c.f. section 1.1.6), forward lobe scattering (c.f. section 1.1.1), Dual Beam sizing systems [1.17], Top-Hat beam techniques (c.f. section 1.1.3) are also used for particle sizing. We mentioned earlier on in this thesis (cf. section 4.) that operating PDA technique was difficult if not impossible due to many factors such as the depth of the furnace, the connecting aperture to the instrument and temperature gradients within the duct. The GPS sizing technique described previously in section 5 was proven to induce high uncertainties for sizing spherical particles. It had nevertheless the advantage to be operated in the backward direction using only one detector.

In the same line of thought, we designed a technique based on the measurement of the intensity scattered from a spherical particle to determine its size. This type of technique refers to angular light scattering measurements, which can be categorised as either relative or absolute [6.3]. In relative intensity measurements, the ratio of the light scattered at an angle θ and the light scattered at a reference angle ξ is determined to yield the particle size. Comparatively, in absolute intensity measurements, the angle

ξ=0, therefore the light scattered at this angle is the incident light on the particle. A common instrument for such angular light scattering experiments is called a nephelometer (a detail description of it is given in [6.4]). The theoretical description of the size-intensity relationship is then provided by exact Mie theory calculations. Nowadays lasers are the most widely used source of light in single particle light scattering experiments and a well know problem for intensity measurements is the non-uniform Gaussian nature of the incident beam profile. This is illustrated in Fig.6.a below. Two identical particles A and B crossing the beam at two different positions generate different scattered intensities.

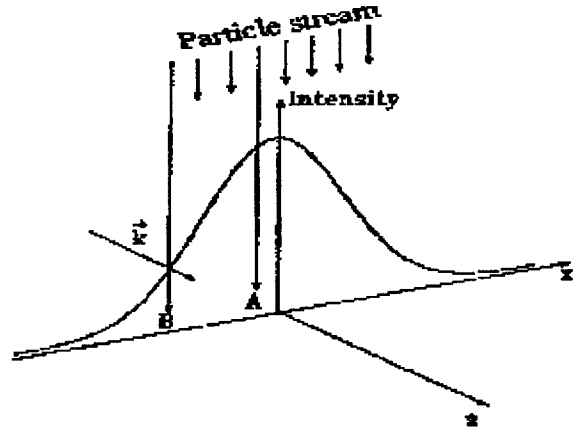

Fig.6.a. Illustration of the Gaussian beam uncertainty [1.4].

Few techniques have been designed to remove the so called Gaussian beam uncertainty. These are the Dual Beam technique (c.f. section 1.1.2) and the Top-Hat beam technique. For the latter, many systems aiming at the production of a flattened intensity distribution have been studied by different authors. However almost all these techniques result in a decrease of the incident intensity, therefore limiting the detecting capability of the system. Nevertheless, the most promising is due to Liu and Gu (c.f.

section 1.1.3) where a Gaussian irradiance of circular polarisation is transformed into a top hat irradiance by a laser beam shaping method using polarisation selective diffractive phase elements (PDPE). The loss of light in then simply due to reflection/absorption by the PDPE.

Shodl [6.5] designed a Laser-Two-Focus Velocimetry technique, consisting in two highly focused laser beams. The light scattered from the particles provided two pulses, the relative time delay of which gave the velocity perpendicular to the laser beams. This technique does not provide particle size measurements, but nevertheless allows for velocity measurements of very small particles in high speed applications.

The technique we studied aims at avoiding the loss of light that is induced by traditional top hat profile production systems (typically 90%). In this technique, that we called arbitrarily the Two Beam System (TBS), a simple birefringent prism is used to separate the incident laser beam into two orthogonally polarised parallel beams, separated in space by a distance d such that they overlap. Two photomultipliers analyse the scattered intensities of the orthogonal polarisations, the relative delay and amplitudes of which are indicative of the particle direction. The determination of the amplitude under which the particle was illuminated is achieved with a specific algorithm designed to retrieve the information on the velocity and trajectory of the particle. Mie theory calculations are carried out in order to determine the intensity variation with particle size and a calibration of the system is provided with certified spherical particles. Having obtained the trajectory of the particle within the coupled laser beams, we can then deduce the particle size from the Mie theory calculations.

6.1 Theoretical calculation of the scattered intensity using Mie theory.

The Mie theory was briefly summarised in section 5.5.1. We used for these calculations the same FORTRAN77 program provided by Pr.A.R.Jones, implemented with an integration routine.

6.1.1 Effect of angular integration.

In this study, we focused our attention on non-absorbing particles with a refractive index m=1.52+0i. The reason for this limitation is that it corresponded to the refractive index of the particles that were available for the calibration of the instrument. In all calculations, we give the theoretical variation of both scattered intensities I_p^{th} and I_s^{th} as a function of either the scattering angle θ or as a function of the size parameter $\chi = \frac{\pi d}{\lambda}$. Here the size parameter χ range considered was 6-670, corresponding to an approximate diameter d range of 1-115 μm, with λ= 0.532 nm. The reason for the upper size limitation was that the Mie theory calculations became increasingly time consuming with increasing size parameter. We were then limited by the computational power of the Unix workstations we used. In the figs.6.1.1.a,b and c below are plotted I_p^{th} and I_s^{th} as a function of the scattering angle θ respectively for $\chi = 6$, 16 and 25, to illustrate the angular variation with increasing size parameter. We can see that the complexity of the scattering pattern increases with the size parameter and that I_p^{th} and I_s^{th} exhibit the same behaviour in the small angle region (forward scattering). However this similarity breaks at higher angles and they can even differ by more than 1 order of magnitude. This is seen in fig.6.1.1.a and fig.6.1.1.c. The relationship between the two

orthogonal polarisations at a particular angle (for our measurements at 140 degrees) will be characterized later in section 6.2.2. The effect of angular integration over a solid angle Ω is to smooth out the scattered intensities curves. However, for small size parameter (<10), the average width of the lobes in the scattering pattern is similar to the collection aperture angle, and therefore significant residual oscillations are present (cf. fig.6.1.1.a).

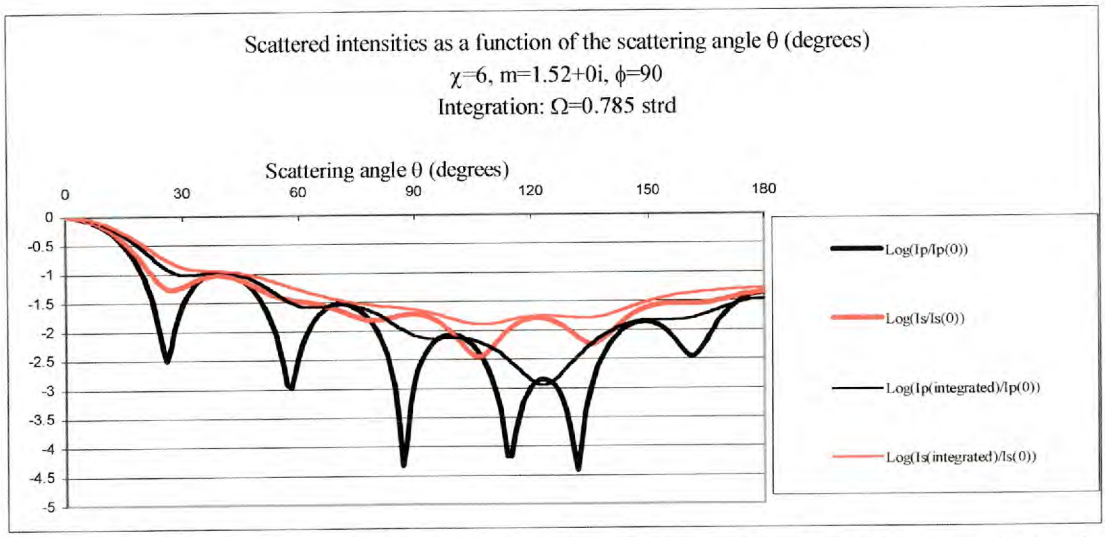

Fig.6.1.1.a. Scattered intensities angular variation(integrated and non-integrated) $\chi = 6$.

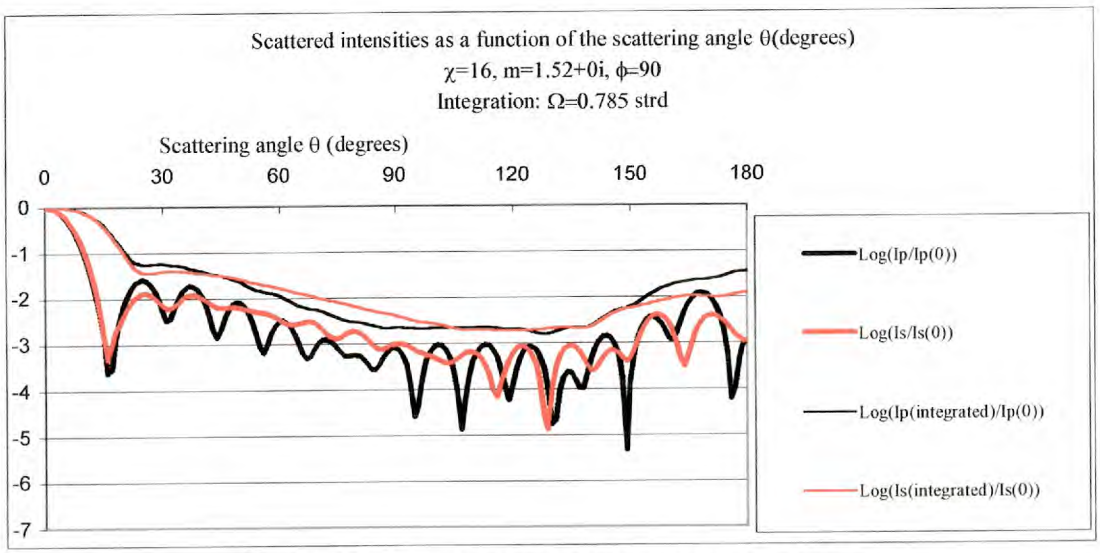

Fig.6.1.1.b. Scattered intensities angular variation (integrated and non-integrated) for $\chi = 16$.

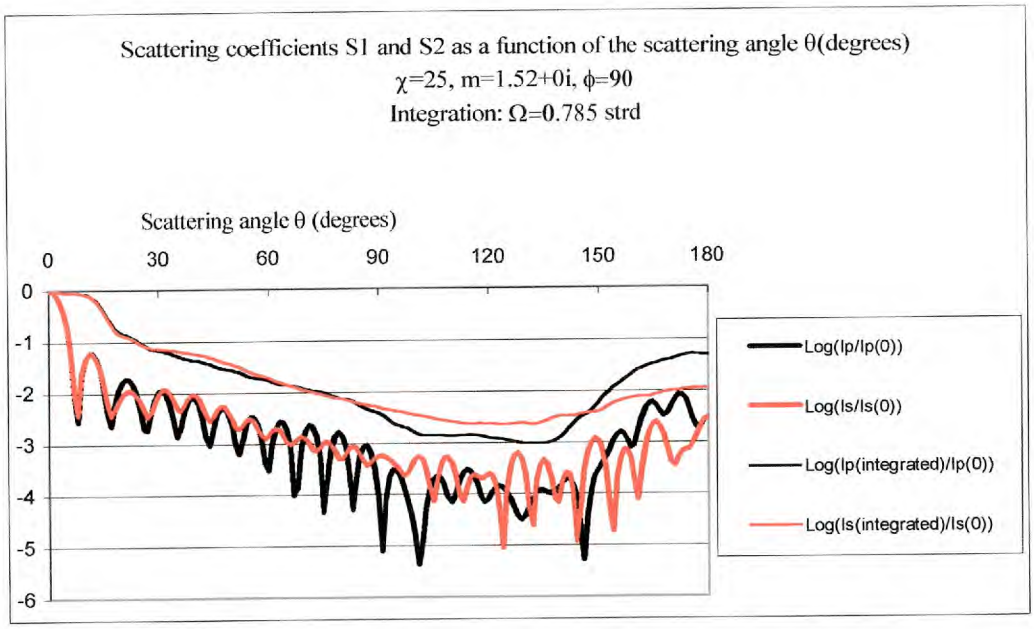

Fig.6.1.1.c. Scattered intensities angular variation (integrated and non-integrated) for $\chi = 25$.

6.1.2 Intensity-size relationship.

With regards to intensity measurements, the intensity-size relationship is of major importance as it provides the calibration curve to deduce the particle size. Having pointed out the effect of angular integration in the previous section 6.1.1, we now have to consider the effect of angular integration around a main angle (that according to which the scattered light collecting system is aligned) with respect to the particle size parameter. With the same parameters m=1.52+0i, ϕ=90 degrees and Ω=0.785 strd, we looked at the variation of the scattered intensities with size at a main angle θ_0=140 degrees. In order to observe the angular integration effect, we plotted in fig.6.1.2.a below the intensity-size curve without integration and with integration in fig.6.1.2.b.

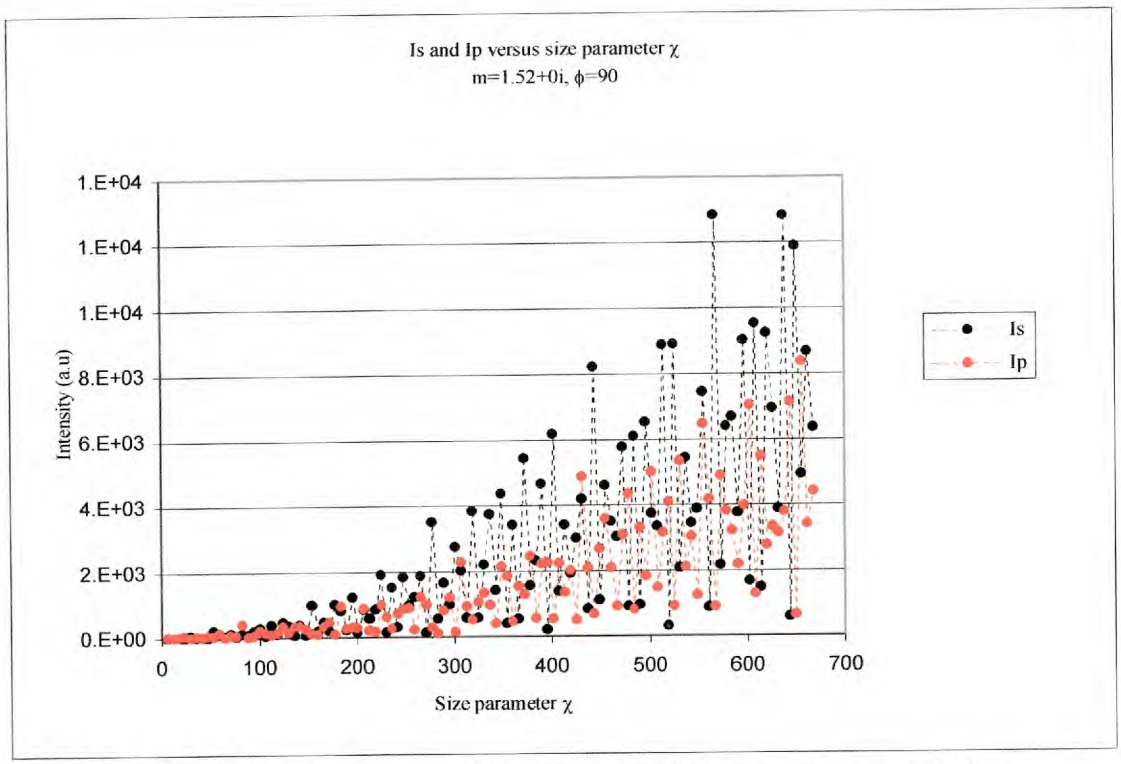

Fig.6.1.2.a. Intensity-size relationship at θ_0=140 degrees - no integration.

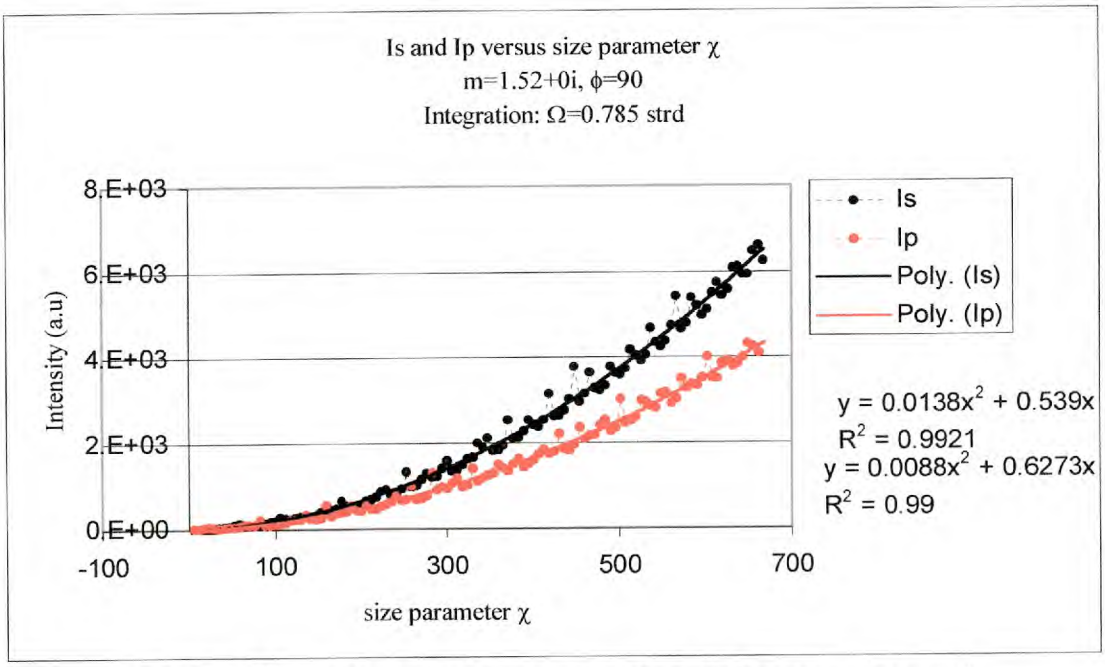

Fig.6.1.2.b. Intensity-size relationship at θ_0=140 degrees- integrated.

It is seen in fig.6.1.2.a that the scattered intensities at θ_0=140 degrees exhibit considerable oscillations with respect to the size parameter. Such oscillations are smoothed out with angular integration, which reduces the oscillations of the scattering pattern, therefore reducing the difference between I_p^{th} and I_s^{th}. Fig.6.1.2.b illustrates the theoretical integrated intensity variation for both orthogonal polarisation components with respect to the size parameter. In these calculations, the scattering geometry parameters used correspond to those of the experiment for particle sizing with the TBS, presented in section 6.4. It is observed that I_p^{th} and I_s^{th} differ, although they have quasi monotonic trends. This effect will be later taken into account in a correction scheme applied in the calculations to retrieve particle size, the theoretical development of which is presented in section 6.2.2.

6.2 Two Beam System (TBS) to estimate the particle trajectory, velocity and location within the Gaussian beam.

6.2.1 Principle of the technique.

The following set up in fig.6.2.1.a was used to produce two orthogonally polarized laser beams propagating along the z-axis, being separated by a distance d. The incident laser beam had to be polarisation shifted at an angle of 45 degrees relatively to the optical axis of a birefringent prism. In this configuration, the prism caused the separation of the incident beam into two orthogonally polarized beams of equal amplitudes propagating at an angle inferior to 2 mrad. When the diameter ϕ of the incident laser beam is bigger than the separation d induced by the prism, then the two orthogonally polarized laser beams overlap without interfering.

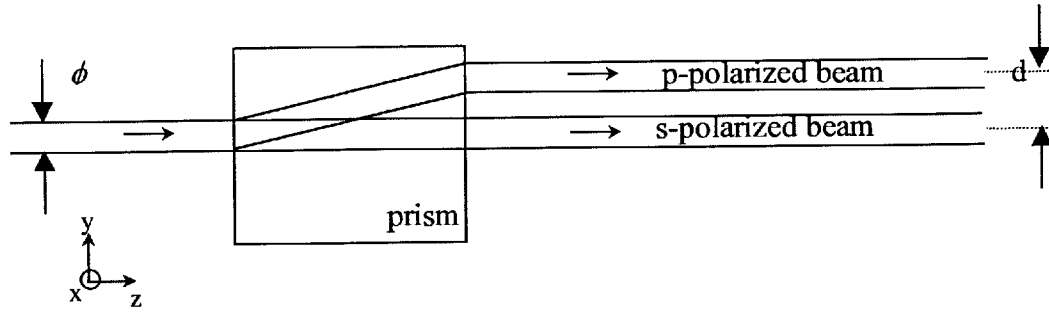

Fig.6.2.1.a. Optical set up for the Two-Beam System.

This is illustrated on fig.6.2.1.b below, which is a 3-dimensional theoretical representation of the intensity distribution of a cross section of the two overlapping beams. Given that the size of the particle crossing the test space is much smaller than ϕ, there is a unique relationship between the position of the particle and the scattered polarized intensities.

The intensity distribution $I(x,y)$ is given by:

$$I(x,y) = e^{-\frac{x^2+(y-y_0)^2}{2\sigma^2}} + e^{-\frac{x^2+(y-y_1)^2}{2\sigma^2}} \qquad \text{(Eq.6.2.1.a)}$$

Where : $-y_0$ and y_1 are the transverse displacements of each beam relatively to the y-axis.

$-\sigma$ is the $\frac{1}{e^2}$ radius of the incident laser beam.

We assumed the incident laser beam to have a Gaussian intensity distribution and a null divergence.

For the sake of simplicity, we treated the case of a particle of diameter small relatively to ϕ, crossing the laser beams with an absolute transverse velocity v according to the trajectory:

$$y = \tan(\alpha)x + b \qquad \text{(Eq.6.2.1.b)}$$

Where α is the trajectory angle of the particle.

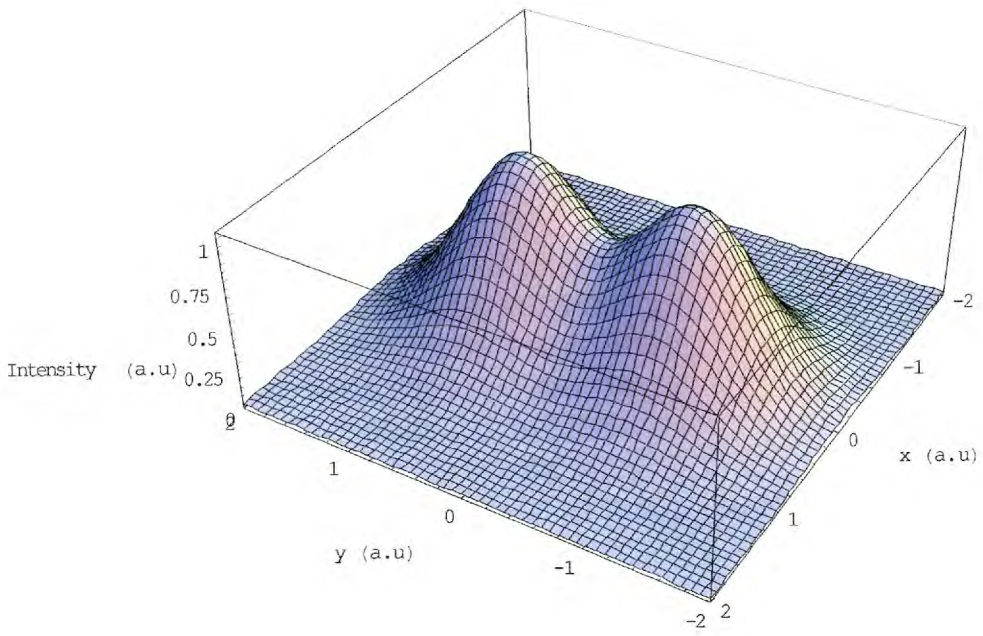

Fig.6.2.1.b. Intensity distribution of a cross section of the beams (a.u).

The scattered intensities of s- and p-polarisations are illustrated in Fig.6.2.1.c.(a),(b) and (c) for different trajectories. In each example, it was assumed that the scattering coefficients of the particle were identical. This is not the case in reality, but this will be assumed in this section to simplify the explanation of the principle underlying the Two Beam System.

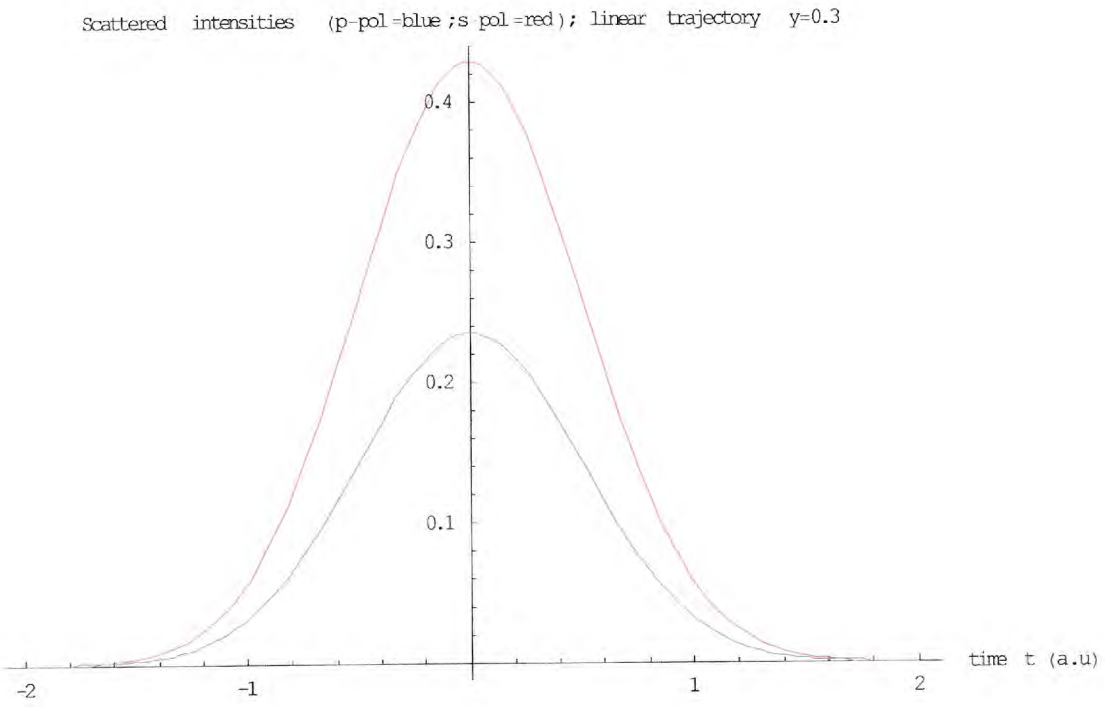
Scattered intensities (p-pol=blue ; s pol=red); linear trajectory y=0.3
0.4
0.3
0.2
0.1
-2
-1
1
2
time t (a.u)

(a)

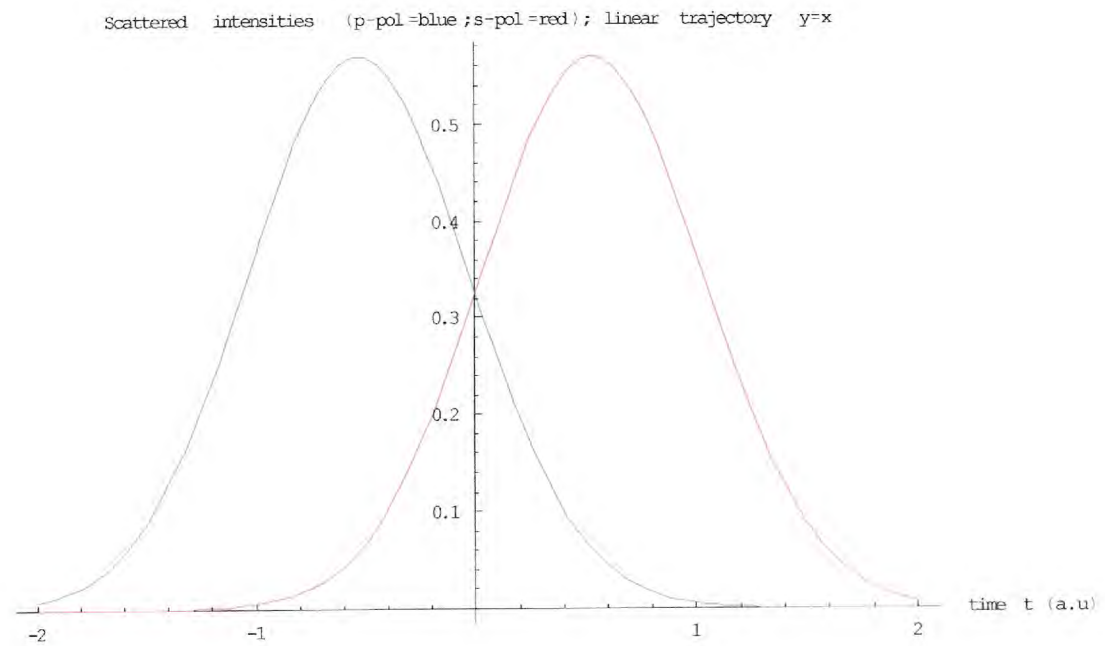
Scattered intensities (p-pol=blue ; s-pol=red); linear trajectory y=x
0.5
0.4
0.3
0.2
0.1
-2
-1
1
2
time t (a.u)

(b)

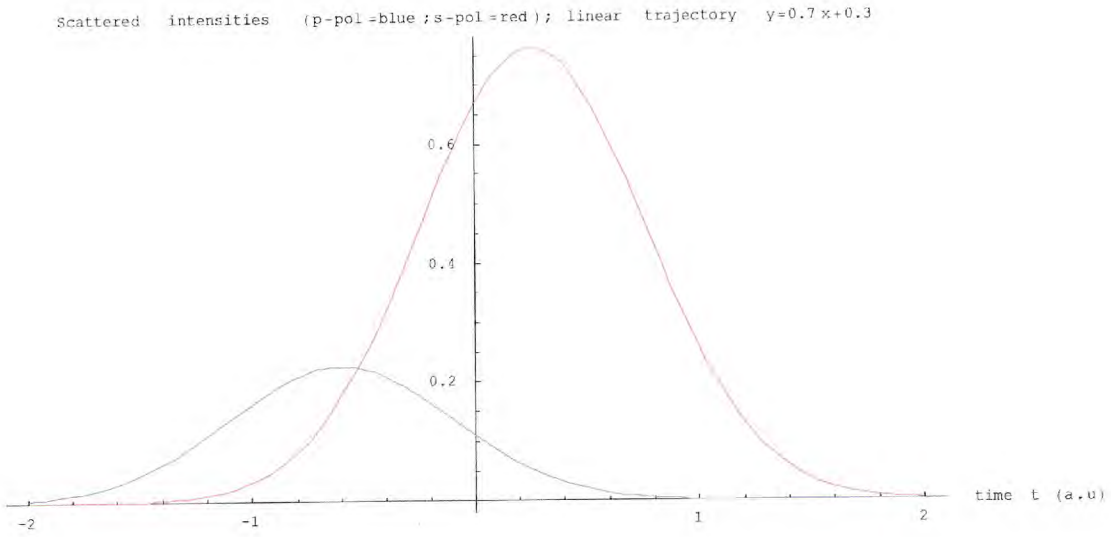

(c)

Fig.6.2.1.c.Scattered intensities of s- and p-polarized beams by a small particle crossing the test space with different trajectories (a) y = 0.3, (b) y = x, (c) y = 0.7x + 0.3.

From such graphs, we can see that information on the trajectory of the particle can be gained by measuring the ratio of the heights of the two signals and their relative delay. Because the laser beams intensity distribution is Gaussian, we shall expect a scattered intensity having a Gaussian variation in time for any particle of diameter small comparatively to σ. A Gaussian fit applied to the data then allows us to characterize the scattered intensity with two parameters: The mode of the Gaussian distribution and its $\frac{1}{e^2}$ radius (note: the mode is expressed in seconds because we measured the scattered intensity time variation). Fig.6.2.1.d illustrates the Gaussian fit obtained with Labview 5.1 for the scattered intensities from a small particle crossing the beams with an arbitrary trajectory.

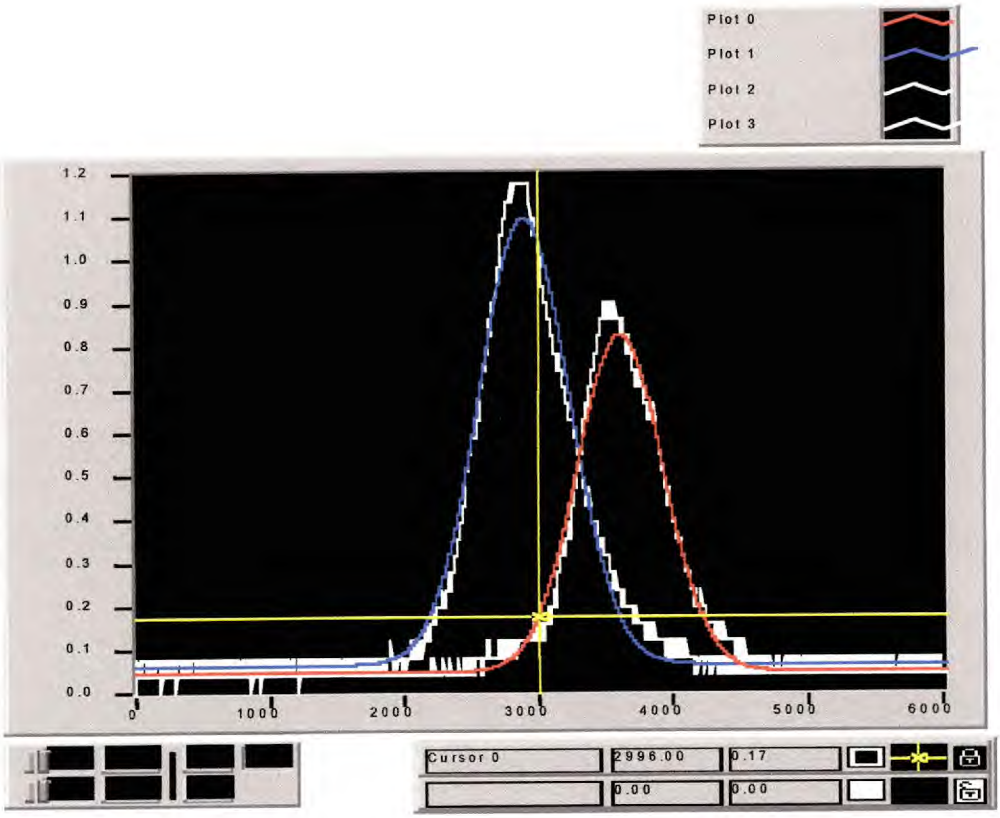

Fig.6.2.1.d. Gaussian fits (red and blue curves) applied to the intensity variations of the light scattered by a particle crossing the TBS with an arbitrary trajectory.

6.2.2 Theoretical modelling of the TBS.

Let us establish the variables I_p^m and I_s^m as being the scattered intensities of orthogonal polarisations analysed through the photomultipliers. Let us also write the corrected intensity values of I_p^m and I_s^m as being I_p^c and I_s^c. The correction applied to I_p^m and I_s^m is twofold. Firstly, in order to be able to measure the particle size using the scattered intensity, we have to consider the trajectory of the particle within the Gaussian intensity distribution. The further away the trajectory of the particle will be from the centre of the Gaussian beam, the less the intensity of the illumination of the particle. Therefore, to compensate for this effect, we have to apply a correction factor that

accounts for this decrease in intensity. What we obtain after applying this correction factor is then the "virtual" scattered intensity that would have been scattered by the particle if it had gone exactly through the centre of the beam. Let us call the intensity correction factors C_s and C_p. We can then write the following relationship:

$$\begin{cases} I_s^c = C_s I_s^m \\ I_p^c = C_p I_p^m \end{cases} \qquad \text{(Eq.6.2.2.a)}$$

where $C_i = \exp(\frac{r_i^2}{2\sigma^2})$, with r_i the minimal distance from the trajectory to the centre of the beam and σ the standard deviation of the Gaussian intensity distribution (identical for the two orthogonal polarisation beams) – see fig.6.2.2.a on page 116. Secondly, as seen previously in fig.6.1.2.b, the scattered intensities both exhibit a monotonic trend, but they differ. The second order polynomial fit applied to the calculated data suggest that the relationship between them is non-linear. Therefore we have to define another coefficient $\beta(\chi)$ that will take into account this non-linear relationship. We can then finally rewrite Eq.6.2.2.a as:

$$\begin{cases} I_s^c = C_s I_s^m \\ I_p^c = C_p I_p^m \beta(\chi) \end{cases} \qquad \text{(Eq.6.2.2.b)}$$

$\beta(\chi)$ is the ratio of the 2nd order polynomial fits of I_p^{th} and I_s^{th} obtained from the Mie theory calculations. $\beta(\chi)$ is then defined as:

$$\beta(\chi) = \frac{w_0^s + w_1^s \chi + w_2^s \chi^2}{w_0^p + w_1^p \chi + w_2^p \chi^2} \qquad \text{(Eq.6.2.2.c)}$$

Thus, having defined the two correction factors, we can write, as $I_s^c = I_p^c$:

$$\exp(\frac{r_s^2}{2\sigma^2}) I_s^m = \exp(\frac{r_p^2}{2\sigma^2}) I_p^m \beta(\chi) \qquad \text{(Eq.6.2.2.d)}$$

Using mono-disperse particles of size parameter χ_R, we know the value of $\beta(\chi_R)$ to be used for the correction and therefore determine from the measurements the calibration factor K_f. This calibration factor is defined as:

$$\begin{cases} I_s^c(\chi) = \dfrac{K_f}{I_s^{th}(\chi_R)} I_s^{th}(\chi) \\ I_p^c(\chi) = \dfrac{K_f}{I_s^{th}(\chi_R)} I_p^{th}(\chi)\beta(\chi) \end{cases} \qquad \text{(Eq.6.2.2.e)}$$

Therefore, replacing $I_s^{th}(\chi)$ and $I_p^{th}(\chi)$ by $I_s^{th}(\chi_R)$ and $I_p^{th}(\chi_R)$ when using the mono-disperse particles of size parameter χ_R, we obtain:

$$\begin{cases} I_s^c(\chi_R) = K_f \\ I_p^c(\chi_R) = K_f \end{cases} \qquad \text{(Eq.6.2.2.f)}$$

which satisfies the condition $I_s^c = I_p^c$.

Using Eq.6.2.2.d and Eq.6.2.2.e, we obtain a system of 2 equations with three unknown variables (χ, r_s, r_p):

$$\begin{cases} \dfrac{K_f}{I_s^{th}(\chi_R)} I_p^{th}(\chi) = \exp(\dfrac{r_p^2}{2\sigma^2}) I_p^m \\ \dfrac{K_f}{I_s^{th}(\chi_R)} I_s^{th}(\chi) = \exp(\dfrac{r_s^2}{2\sigma^2}) I_s^m \end{cases} \qquad \text{(Eq.6.2.2.g)}$$

It is however possible to deduce a relationship between r_p and r_s, using a geometrical description of the trajectory of the particle within the two beams. This is illustrated in fig.6.2.2.a, where the two circles represent the Gaussian beam intensity profiles of the two orthogonally polarised beams. The minimal distances from the trajectory to the centre of each beam, namely r_s and r_p, are represented by the thick lines. The distance δ_{sp} is given by the following equation:

$$\delta_{sp} = \frac{\sigma}{\sigma_m}(t_s - t_p) \qquad \text{(Eq.6.2.2.h).}$$

In Eq.6.2.2.h σ is the physical $\frac{1}{e^2}$ radius of the laser beams expressed in metres, σ_m is the measured $\frac{1}{e^2}$ width of scattered intensity Gaussian fits expressed in second and $t_s - t_p$ is the time delay between the two fits.

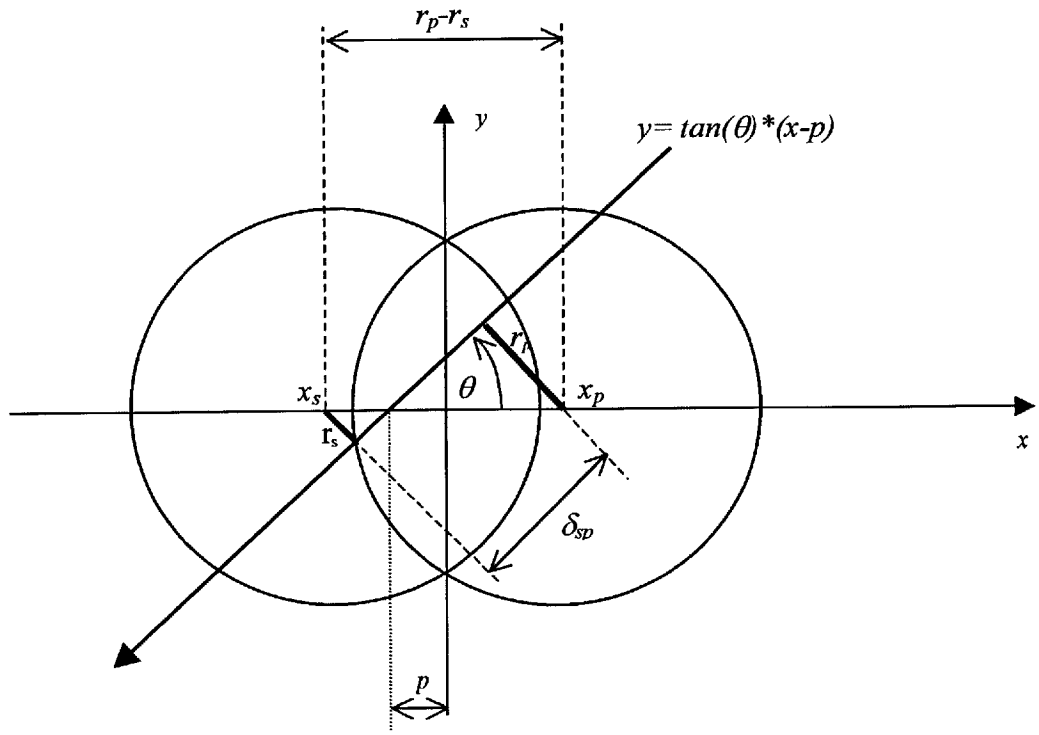

Fig.6.2.2.a. 2-dimensional geometrical representation of the particle trajectory within the TBS.

By simple geometrical considerations, we can write:

$$(r_p + r_s)^2 + (\frac{\sigma}{\sigma_m})^2 (t_s - t_p)^2 = (x_p - x_s)^2$$
$$\rightarrow r_s = \pm\sqrt{(x_p - x_s)^2 - (\frac{\sigma}{\sigma_m})^2 (t_s - t_p)^2} - r_p \qquad \text{(Eq.6.2.2.i)}$$

Let us assume:

$$K = \sqrt{(x_p - x_s)^2 - (\frac{\sigma}{\sigma_m})^2 (t_s - t_p)^2}$$

and rewrite Eq.6.2.2.i as:

$$r_s = \pm K - r_p \qquad \text{(Eq.6.2.2.j)}$$

Replacing Eq.6.2.2.j in Eq.6.2.2.g gives:

$$\begin{cases} \frac{K_f}{I_s^{th}(\chi_R)} I_p^{th}(\chi) = \exp(\frac{r_p^2}{2\sigma^2}) I_p^m \\ \frac{K_f}{I_s^{th}(\chi_R)} I_s^{th}(\chi) = \exp(\frac{r_p^2}{2\sigma^2}) \exp(\frac{K^2 \mp 2Kr_p}{2\sigma^2}) I_s^m \end{cases} \qquad \text{(Eq.6.2.2.k)}$$

The ratio of these equations is:

$$\frac{I_p^{th}(\chi)}{I_s^{th}(\chi)} = \frac{1}{\beta(\chi)} = \frac{I_p^m}{I_s^m} \exp(-\frac{K^2 \mp 2Kr_p}{2\sigma^2}) \qquad \text{(Eq.6.2.2.l)}$$

Therefore:

$$r_p = \pm(-\frac{\sigma^2}{K} \ln(\beta(\chi)) + \frac{\sigma^2}{K} \ln(\frac{I_s^m}{I_p^m}) + \frac{K}{2}) \qquad \text{(Eq.6.2.2.m)}$$

From the first term of Eq.6.2.2.k, we can write as well:

$$r_p^2 = 2\sigma^2 \ln(\frac{K_f I_p^{th}(\chi)}{I_s^{th}(\chi_R) I_p^m}) \qquad \text{(Eq.6.2.2.n)}$$

Identifying Eq.6.2.2.n with Eq.6.2.2.m, we obtain:

$$\left(-\frac{\sigma^2}{K} \ln(\beta(\chi)) + \frac{\sigma^2}{K} \ln(\frac{I_s^m}{I_p^m}) + \frac{K}{2}\right)^2 = 2\sigma^2 \ln(\frac{K_f I_p^{th}(\chi)}{I_s^{th}(\chi_R) I_p^m})$$

(Eq.6.2.2.o)

The right and left hand parts of Eq.6.2.2.o constitute the equations for two curves the intersection point of which gives a value for the size parameter χ.

6.3 Estimation of velocity and position.

In this section, we talk about "estimation" rather than measurement. In section 6.1.2 was presented the function used to fit each of the analysed scattered intensities data of the two orthogonally polarised beams. Various factors affected the quality of the fit, such as the electronic noise, the oscillations in the scattering process due to spherical shape inhomogeneities of the particles and multiple light scattering. In the later case, it was impossible to differentiate whether there was one or more particles in the test space. However, we assumed that the blown particles were in sufficiently low concentration so as to have single light scattering. Nevertheless, it is probable that most errors were caused by multiple scattering. Additionally, we detected the particles with a special algorithm which allowed the program to select the fits for which the error from the original signal was below a particular value. Consequently, the Gaussian fits applied to the data were selected according to their accuracy, but the occurrence of multiple scattering was not discriminated from single scattering.

The set up used to estimate the particle velocity and trajectory was similar to the one presented earlier in fig.4.2.a. The GPS system was set with a He-Ne laser (3mW) and its collecting optics were adjusted at an angle of 140 degrees. The TBS was inserted in conjunction with the GPS, but at different angles relatively to each other. The TBS was also set with its collecting optics at 140 degrees. The schematic of the set up is illustrated below in fig.6.3.a.

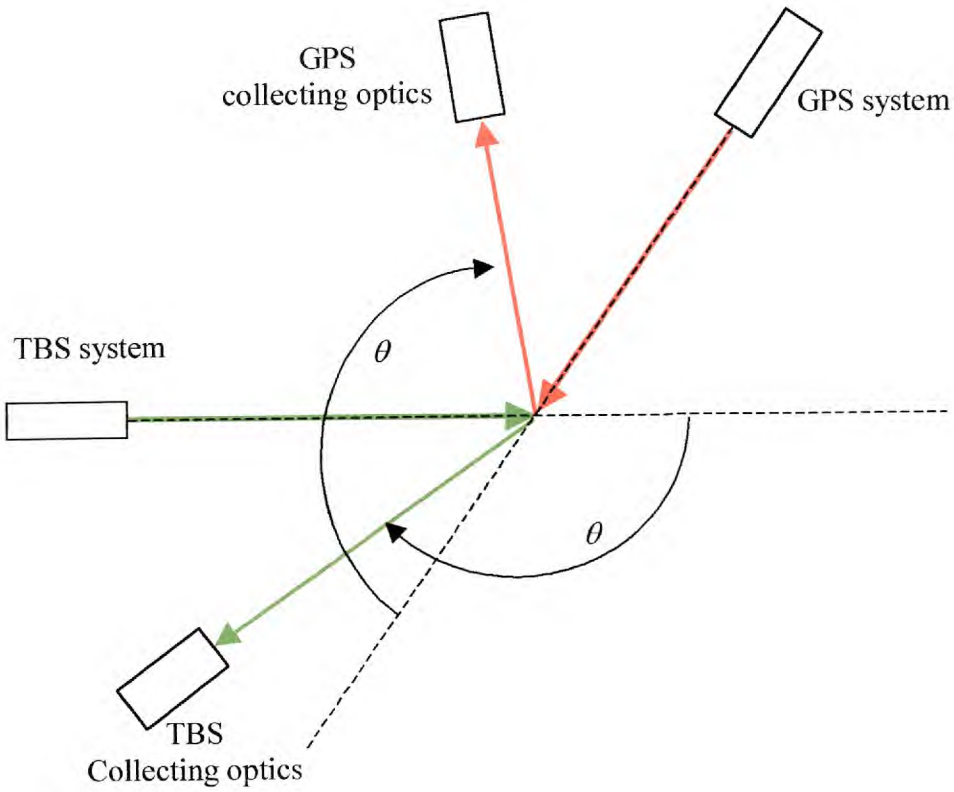

Fig.6.3.a. Schematic diagram of the set up configuration.

The angle between the GPS and the TBS system was set approximately to 120 degrees. The precision of this angle was not crucial in this case, as each system was independent of each other. The TBS collecting optics consisted of a polarisation splitting cube similar to the one used in the optical instrument which was described in section 2 (50:1 polarisation ratio). This cube had its polarisation axis aligned respectively to the polarisation axis of the TBS beams. Two miniature photomultipliers detected the orthogonally polarised components. The photomultipliers were coupled to an amplifier (times 10) and their signals were analysed through a data acquisition device DaqPad from National Instruments, using the software Labview 5.1. The GPS signal was also acquired through this instrument, which had 8 input/output channels mounted

in differential mode. The resolution of the DaqPad was 12 bits, over a variable range from +/-.05V to +/-10V.

Because the velocity of the particles crossing the two beams was determined by applying a Gaussian fit to the scattered intensity data, we had first to characterise the laser beam divergence. The value of its $\frac{1}{e^2}$ radius at any position was then deduced with the beam divergence, provided the test space position was known with sufficient accuracy. We characterized the laser beam $\frac{1}{e^2}$ radii at two locations along the optical axis at $z = 93$ cm and $z = 163$ cm. We obtained the intensity profile using a fine thread (thickness very small compared to the beam diameter) reflecting the laser light as we moved it along the axis from which we wanted to obtain the beam profile. The standard two-dimensional Gaussian distribution function,

$$I(x,y) = I_0 \exp(-\frac{(x-x_0)^2 + (y-y_0)^2}{2\sigma^2}) \qquad \text{(Eq.6.3.a)}$$

was assumed to represent adequately the laser beam cross section intensity distribution. When integrating $I(x,y)$ along the x-axis, it is found that the intensity is simply a function of y and is still a Gaussian distribution function. With the assumption that the thread width was constant over its length, the scattered intensity would then be described by a one-dimensional Gaussian distribution function:

$$I(y) = I_0^{(x)} \exp(-\frac{(y-y_0)^2}{2\sigma^2}) \qquad \text{(Eq.6.3.b)}$$

We then applied the following procedure to obtain the information relative to the $\frac{1}{e^2}$ radius:

1/ The logarithm of the collected data ln*(data)* was calculated, i.e. for the intensity of light scattered by the thread at each position along the y-axis.

2/ A 2nd order polynomial fit $\ln(data) = w_0 + w_1 y + w_2 y^2$ was applied so as to identify $\ln(data)$ with:

$$\ln(I(y)) = \ln(I_0^{(x)}) - \frac{y_0^2}{2\sigma^2} - \frac{y^2}{2\sigma^2} + \frac{yy_0}{2\sigma^2} \qquad \text{(Eq.6.3.c)}$$

3/ The $\frac{1}{e^2}$ factor was then obtained by equalizing the coefficient w_2 of the fit with $\left(-\frac{1}{2\sigma^2}\right)$:

$$\sigma = \sqrt{-\frac{1}{2w_2}} \qquad (w_2<0) \qquad \text{(Eq.6.3.d)}$$

The beam profiles at $z = 93$ cm and $z = 163$ cm are plotted in fig.6.3.b below.

We obtain then :

z (cm)	σ (μm)
93	449 ±5
163	873 ±8

The polynomial approximations fit the data quite reasonably. The beam divergence was calculated from the linear approximation between the calculated values of σ (c.f. fig.6.3.c below). The divergence was then approximated to 0.523 mrad, the value of the coefficient of the linear fit.

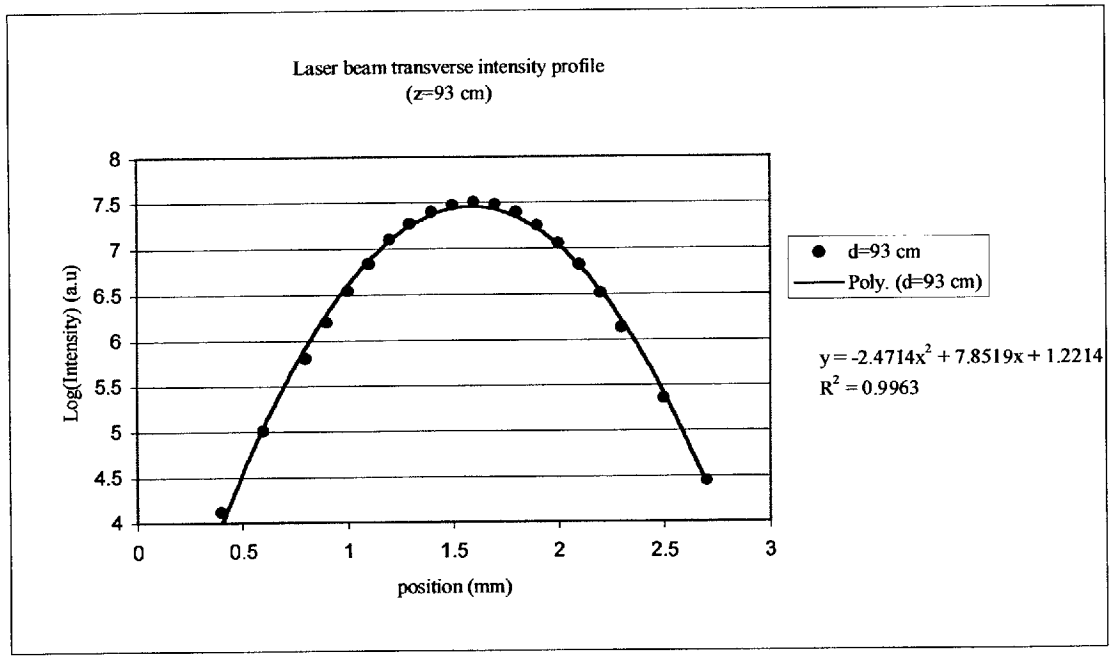

(a)

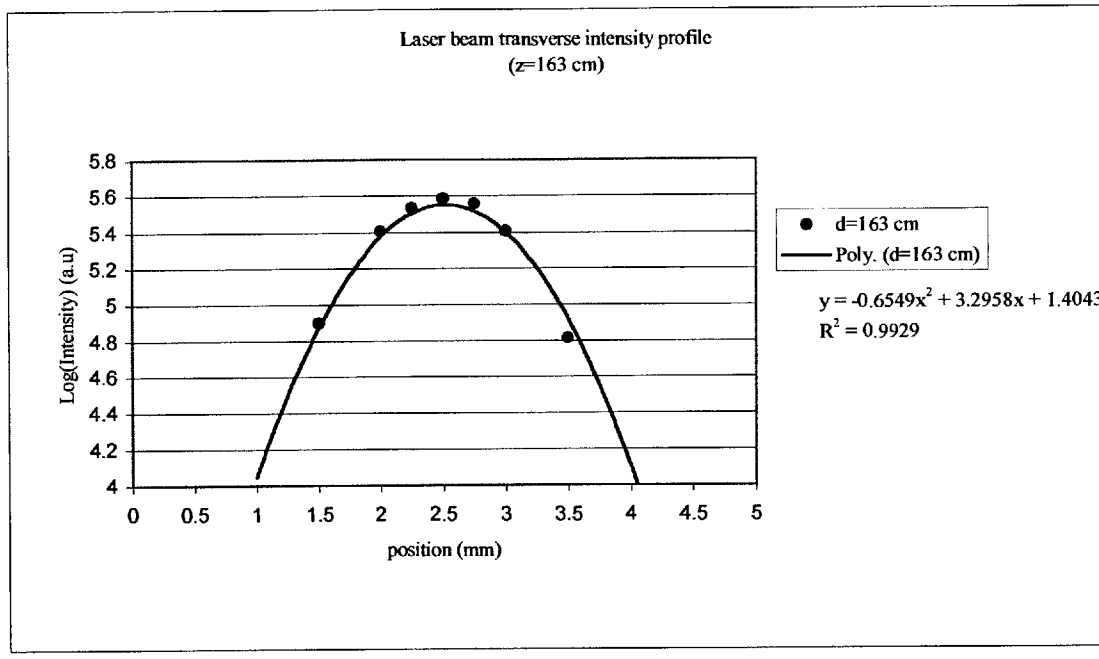

(b)

Fig.6.3.b. Laser beam intensity profile at (a) $z = 93$ cm and (b) $z = 163$ cm.

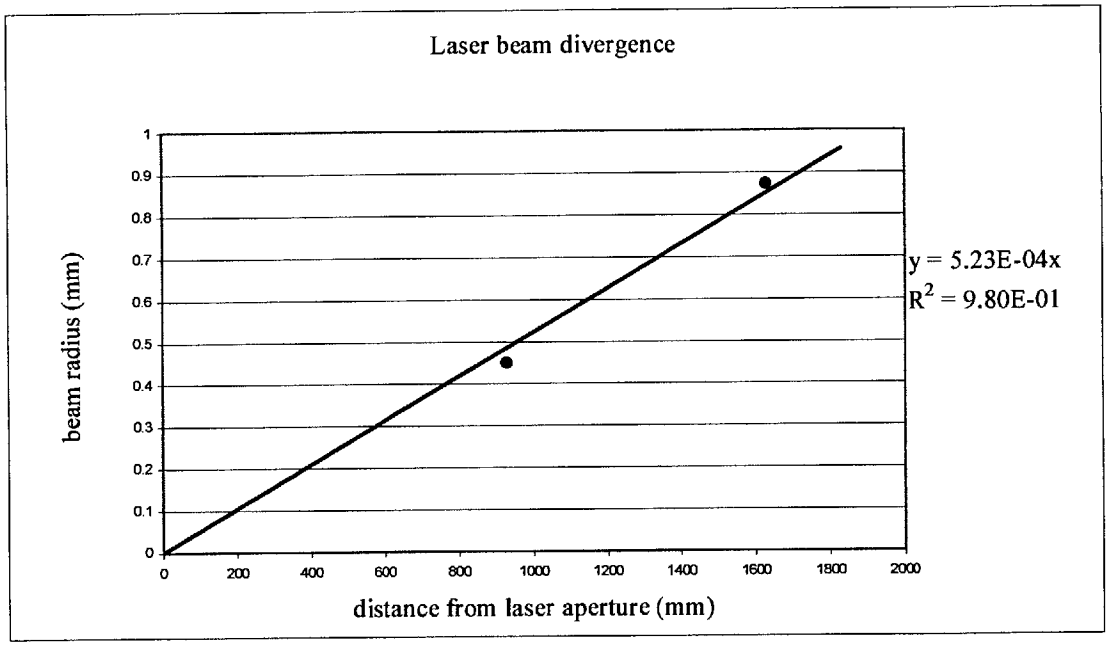

Fig.6.3.c Laser beam divergence.

In our measurements, the test space was located at a distance z = 1m, for which the values of the beams radii were then 523 μm. The particles were blown with a fluidised bed in the same way as in the GPS experiment described in section 4.1.2. The intersecting volume of the two systems (thereby constituting the test space) was 2 mm in width and 5 mm in height. The data were acquired with the trigger from the GPS signal. The information on the velocity v was obtained from the following relationship between the measured physical radius σ (expressed in metres) of the laser beams and the approximated $\frac{1}{e^2}$ value σ_m (expressed in second) of the Gaussian fit applied to the data collected from the TBS signals:

$$v = \frac{\sigma}{\sigma_m} \qquad \text{(Eq.6.3.e)}$$

The results are presented in fig.6.3.d below, where a linear correlation between the GPS velocity measurement and the TBS velocity measurement is clearly observed. Given the uncertainty for the GPS regarding velocity measurements was established to be ±7% when using Labview 5.1 to compute the FFT, the discrepancy from the linear correlation was thought to appear because of the quality of the fit and other factors previously mentioned. While we assumed to have one particle at a time in the test space, multiple light scattering processes have certainly occurred. This is thought to be caused by the aggregates of particles in clusters created by charge accumulation inside the fluidised bed. Apart from observing these aggregates on a microscope slide, it has not been possible to prove this hypothesis. Therefore we obtained an estimation of the particle velocity, as the uncertainty associated with it was not systematic. The trajectory was, for sake of simplicity, defined by the angle of incidence of the particle α and derived from the velocity estimation. From fig.6.2.2.a and Eq.6.2.2.h, we can deduce that:

$$\cos(\alpha) = \frac{\delta_{sp}}{x_s - x_p} = \frac{\frac{\sigma}{\sigma_m}(t_s - t_p)}{x_s - x_p}$$

therefore:

$$\alpha = \arccos\left(v \frac{t_s - t_p}{x_s - x_p} \right) \qquad \text{(Eq.6.3.f)}$$

The time difference $t_s - t_p$ being measured from the Gaussian fits applied to the data and $x_s - x_p$ being the physical separation between the two laser beams, the trajectory angle was then recovered, but was nevertheless affected by the uncertainty associated with the velocity v.

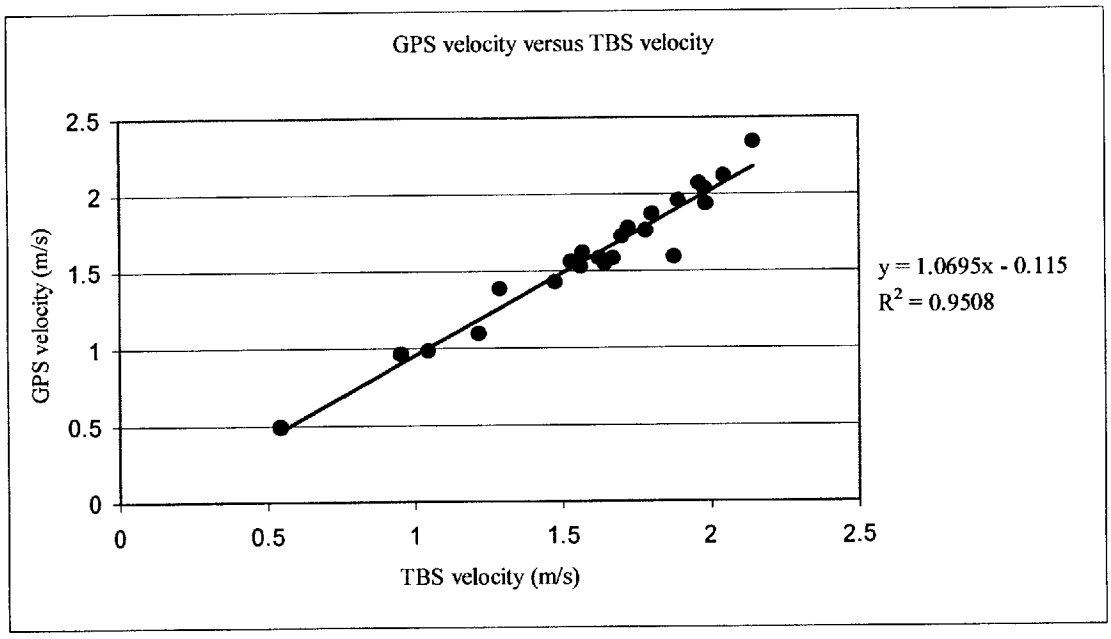

Fig.6.3.d. Correlation between GPS and TBS velocity measurements.

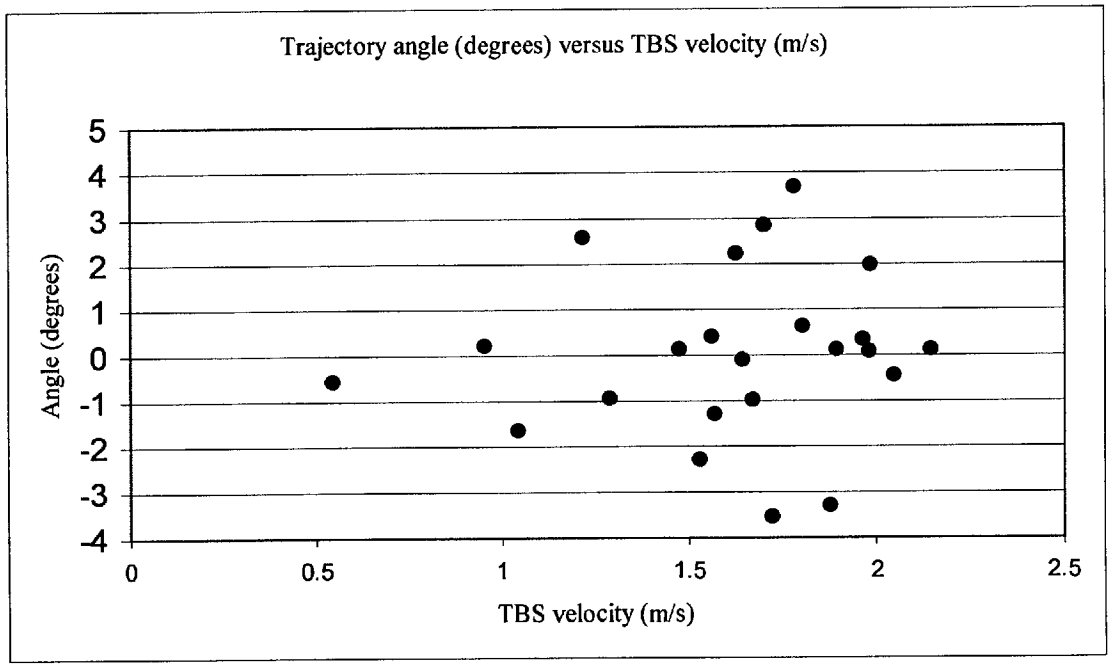

Fig.6.3.e. Trajectory angle versus TBS velocity.

Because in our experiments we lacked of a means to control the direction of incidence of the particles, the calculated values of α cannot be correlated with any reference.

However we present in fig.6.3.e the results for α corresponding to the velocity measurements from fig.6.3.d. In this experiment the particles were blown downwards and therefore we expect the mean value of α to be equal to 0. This is observed and the spread in α is seen to be within ±4 degrees. The uncertainty on the angle α was estimated to be ±5 degrees.

Thus it was demonstrated that the TBS provides an adequate method to estimate the velocity of spherical particles. The correlation in the velocity measurements obtained with the GPS system is quite acceptable.

6.4 Intensity measurements for particle sizing using the TBS.

The determination of particle size by measuring the scattered intensity depends upon the estimation of the particle trajectory. The theoretical development of the TBS technique for particle sizing has been described previously in section 6.2.2. We adapted this theory with Labview 5.1, which allows for the manipulation of data and complex mathematical operations. We simulated, using the theoretical calculations from the Mie theory, the intensities scattered by different particle size distributions with a random trajectory. The particle size distributions were arbitrarily described by a Gaussian distribution function, for which the centred values and standard deviations were varied. These simulations were done in order to characterize the influence of the discrepancies in the integrated scattered intensities variations. When using the 2nd order polynomial fits to establish $\beta(\chi)$, this later exhibits a monotonic relationship with the size parameter χ. However, when using the calculated values of the Mie theory, we found that $\beta(\chi)$ has no longer a monotonic behaviour but presents rather heavy oscillations

around the curve calculated from the polynomial fits. This is illustrated in fig.6.4.a below.

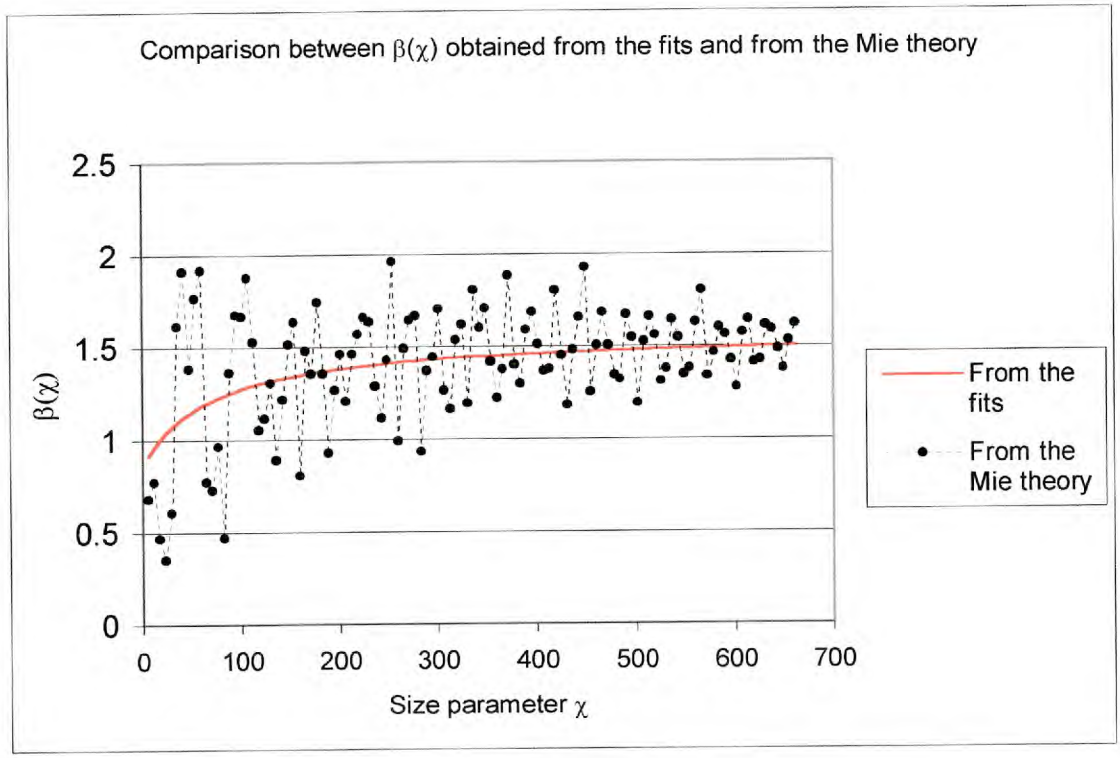

Fig.6.4.a. Comparison between the approximated and real values of $\beta(\chi)$.

We solved Eq.6.2.2.o numerically for the simulations. The detailed results are presented in Annexe IV. The original simulated size distributions are correctly recovered by the algorithm. However, increasing discrepancies are observed with decreasing mean size, which is thought to be due to the larger oscillations of $\beta(\chi)$ for decreasing size. Fig.6.4.b and fig.6.4.c below show the summary of these results. The recovered mean particle size obtained with the algorithm versus the original mean particle size is plotted in fig.6.4.b. Fig.6.4.c shows the standard deviations for different mean particle sizes. Thus form these graphs, it is seen that the algorithm is successful in retrieving the mean

particle size distribution. However the smallest standard deviation recovered was 2 μm, which contrasts by 100% with its original value of 1 μm. Nevertheless, this effect is seen to disappear for higher standard deviations.

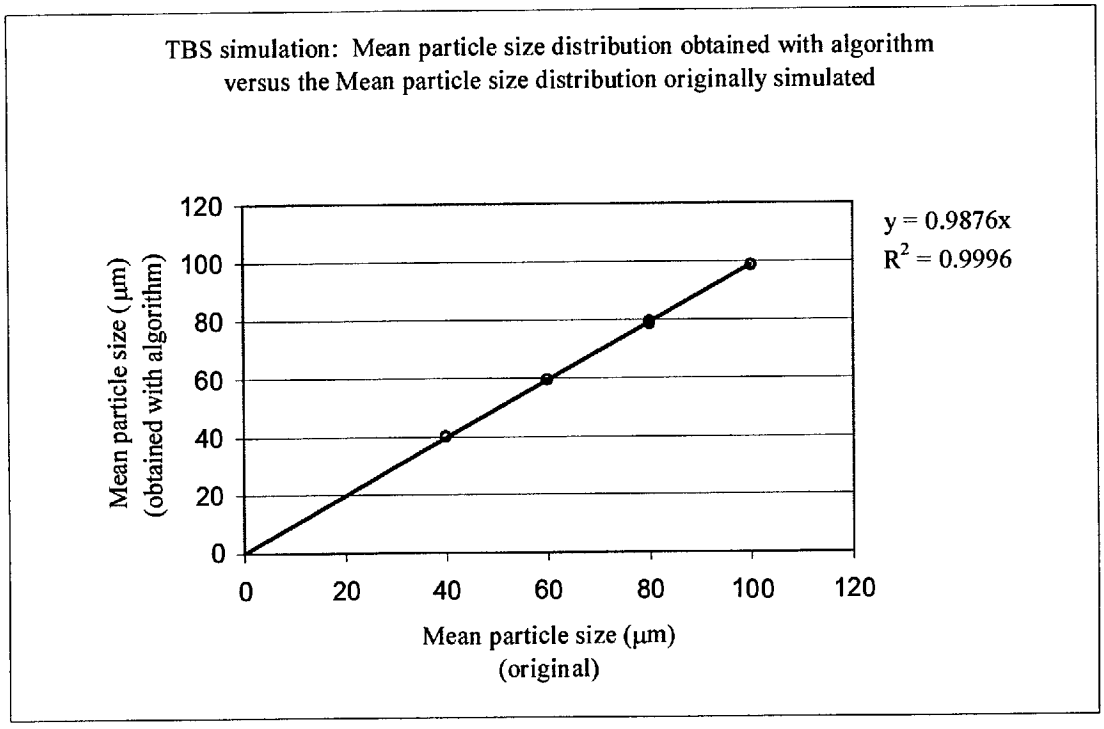

Fig.6.4.b. Mean particle size distribution (algorithm) versus original mean particle size distribution.

Because $\beta(\chi)$ is included in the left hand side term of Eq.6.2.2.o, it could be thought that its fit (c.f. Eq.6.2.2.c) used to calculate $\beta(\chi)$ introduces a large uncertainty in the determination of χ. This is not so, as the simulations proved. Nevertheless, this would be the case if the determination of χ was entirely based on $\beta(\chi)$. Rather, the precision of the algorithm should be seen from the point of view of the fits themselves (c.f. fig.6.1.2.b) which are very close to the Mie theory calculated values.

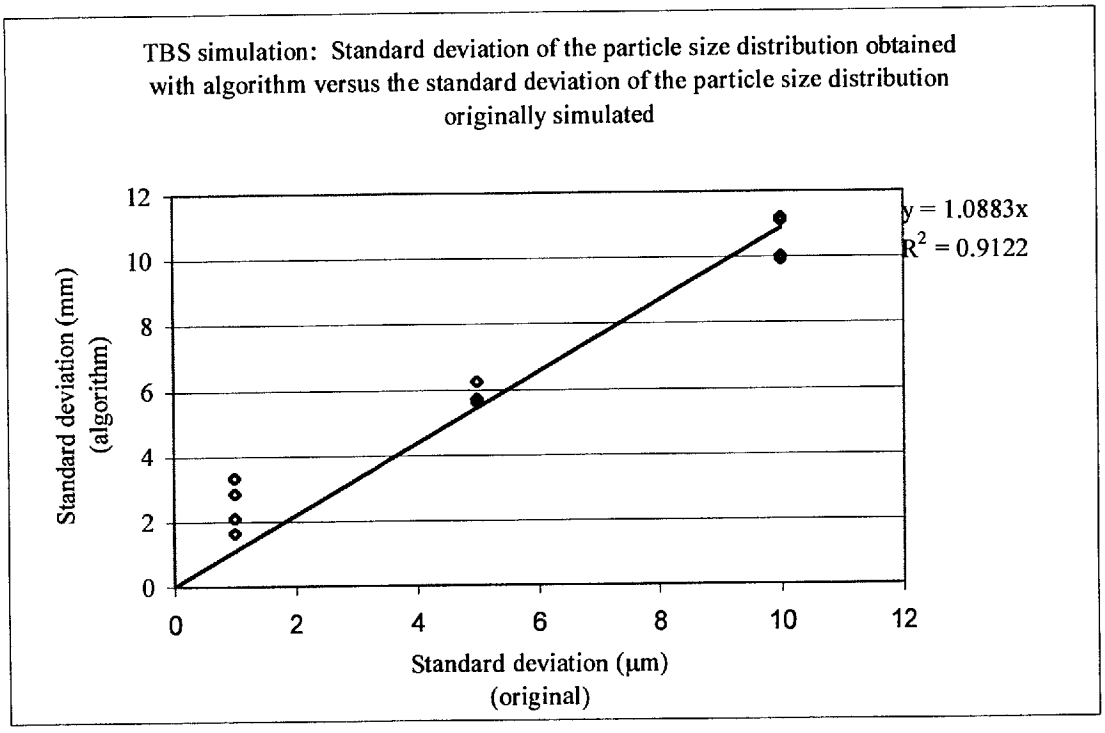

Fig.6.4.c. Standard deviations (algorithm) versus standard deviations (original)

Experimental characterization.

The experimental characterization consisted of two procedures. Firstly we needed to calibrate the instrument with mono-disperse spherical particles to obtain the calibration factor K_f. Secondly, the measurements were carried out with a broad size distribution of spherical particles of the same refractive index as the mono-disperse particles used for the calibration. We used the same experimental configuration described in section 6.3, with a light collection solid angle Ω = 0.785 strd. The main scattering angle was 140 degrees. The mono-disperse particles used for the calibration were Polymethylmetacrylate (PMMA) spheres of complex refractive index m = 1.52 + 0i. Their specified mean size was 73.77 μm with a standard deviation of 2.09 μm. The particles used for the measurements were spherical Ballotini particles of complex

refractive index m = 1.52 + 0i, which size distribution ranged approximately from 80 μm to 130 μm. It has to be noted that the mono-disperse particles were certified, whereas the Ballotini particles were not. For both the calibration and the measurements, we collected the particles and determined their size distribution using a microscope coupled to a CCD camera, where a computer calculated the particle area equivalent diameter. The sphericity of the Ballotini particles was determined in the same way. During all the experiments, a laser power meter was used to measure the laser output power. A coefficient taking into account the fluctuations of the laser power was included in the algorithm to compensate for this effect.

Calibration results.

Fig.6.4.d below shows the measured particle size distribution of the mono-disperse particle sample obtained with the microscope technique described before. It is seen that, although the supplier specified a mean particle size of 73.77 μm, the equivalent particle diameter was 81 μm, with a standard deviation of approximately 2 μm (this value agrees with the supplier specification of 2.09 μm). In the calibration, we therefore used the area equivalent diameter of 81 μm. The smaller sizes from 1 to 65 μm are due to dust on the optics and measurement artefacts caused by particles at the edge of the measurement area of the CCD camera. Fig.6.4.e shows the results obtained with the actual TBS technique. The main particle size is observed at approximately 80 μm, with an uncertainty of 8 μm. According to Eq.6.2.2.f, the calibration coefficient K_f for this particular experimental configuration was obtained with the measurement of $I_s^c(\chi)$, which value was 1600. However, given the simulations presented above, we expect the

measured particle size distribution to reflect the original particle size distribution of the mono-disperse sample.

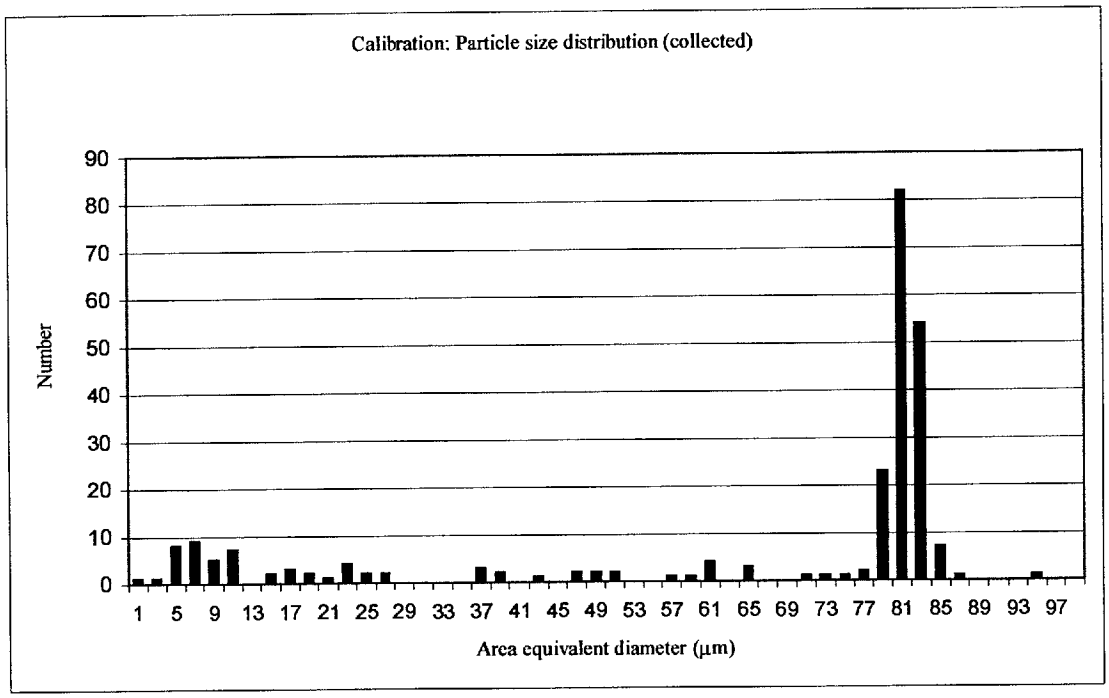

Fig.6.4.d.Mono-disperse particle size distribution (obtained with microscope).

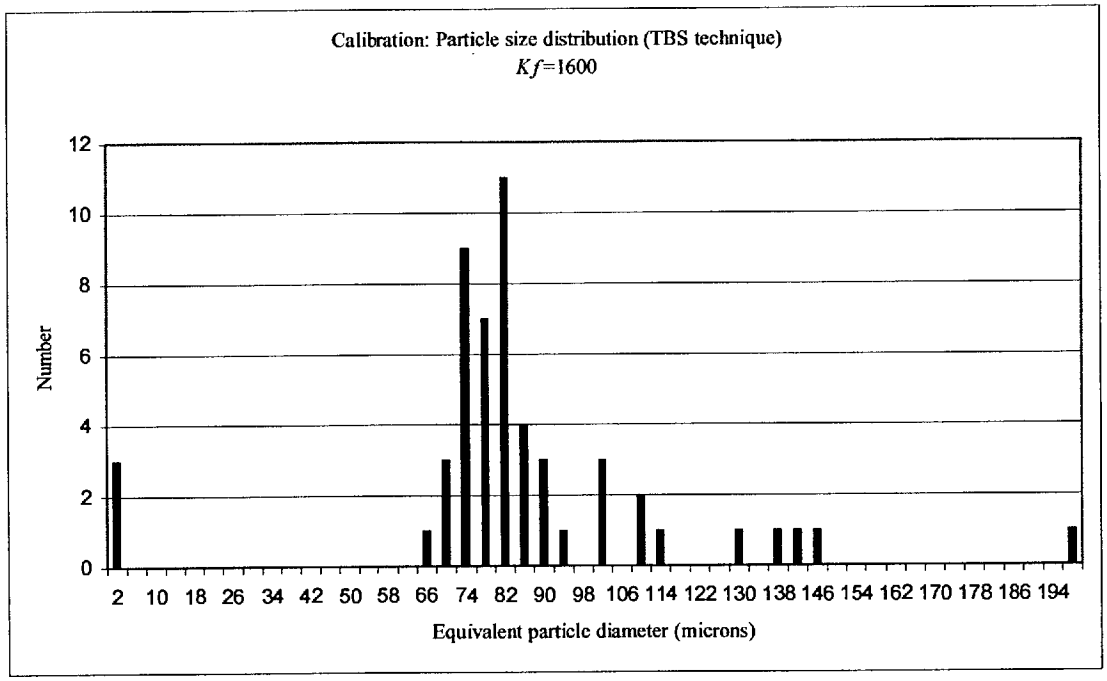

Fig.6.4.e. Mono-disperse particle size distribution (obtained with TBS technique).

It is seen that the standard deviation obtained with the TBS technique is 8 μm, which is 4 times the value of the mono-disperse sample particle size distribution standard deviation. An explanation for this broadening of the recovered size distribution would be that the blowing system did not deliver systematically single particles in the test space. This overestimation could be caused also by small non-sphericity of the certified spherical particles, which is known to introduce quite significant errors relatively to the Mie theory calculations for perfect spheres [2.11].

From these results, we can conclude that the calibration of the instrument is successful, bearing in mind the overestimation of the particle size distribution standard deviation, which is thought to be due to scattering by aggregates or non-spherical particles.

Size measurements

The TBS technique and its algorithm were tested with a broad size distribution, ranging from approximately 80 μm to 130 μm. We carried out the same procedure as in the calibration of the instrument. However, having determined the calibration factor K_f, we were able to measure the particle size with the algorithm of the TBS technique. The particles were also collected and their area equivalent diameter was measured with the same microscope technique. The size distribution of the collected particles is plotted in fig.6.4.f below. Again, the presence of sizes below 73 μm is due to dust on the optics and measurement artefacts caused by particles crossing the edge of the CCD camera measurement area. The particle size distribution is seen to range from 80 μm to 130 μm and a maximum peak is observed at 103 μm. The size measurement of this particular distribution were obtained with the TBS technique and are presented in fig.6.4.g

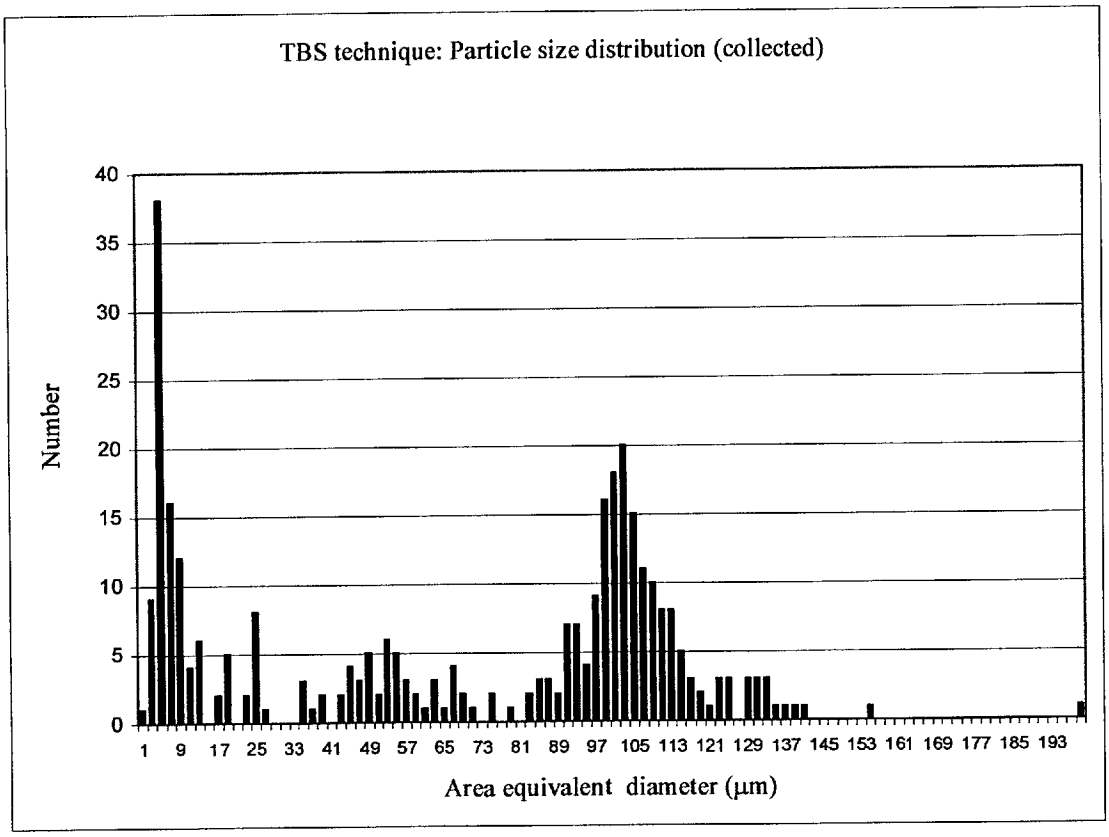

Fig.6.4.f. Broad particle size distribution (obtained with microscope).

The peak of the size distribution obtained with the TBS technique is 102 μm. This measure agrees with the 103 μm peak of the size distribution of the collected particles. Secondly, the sizes range from 74 μm up to 160 μm approximately. When comparing this size distribution with the one presented in fig.6.4.f, we observe a broadening effect. This is similar to the broadening of the distribution which affected the calibration results. The overestimation of the size distribution with the TBS technique is thought to be caused by non-sphericity effects, generating orthogonally polarised scattered intensities different from the one predicted with the Mie theory calculations.

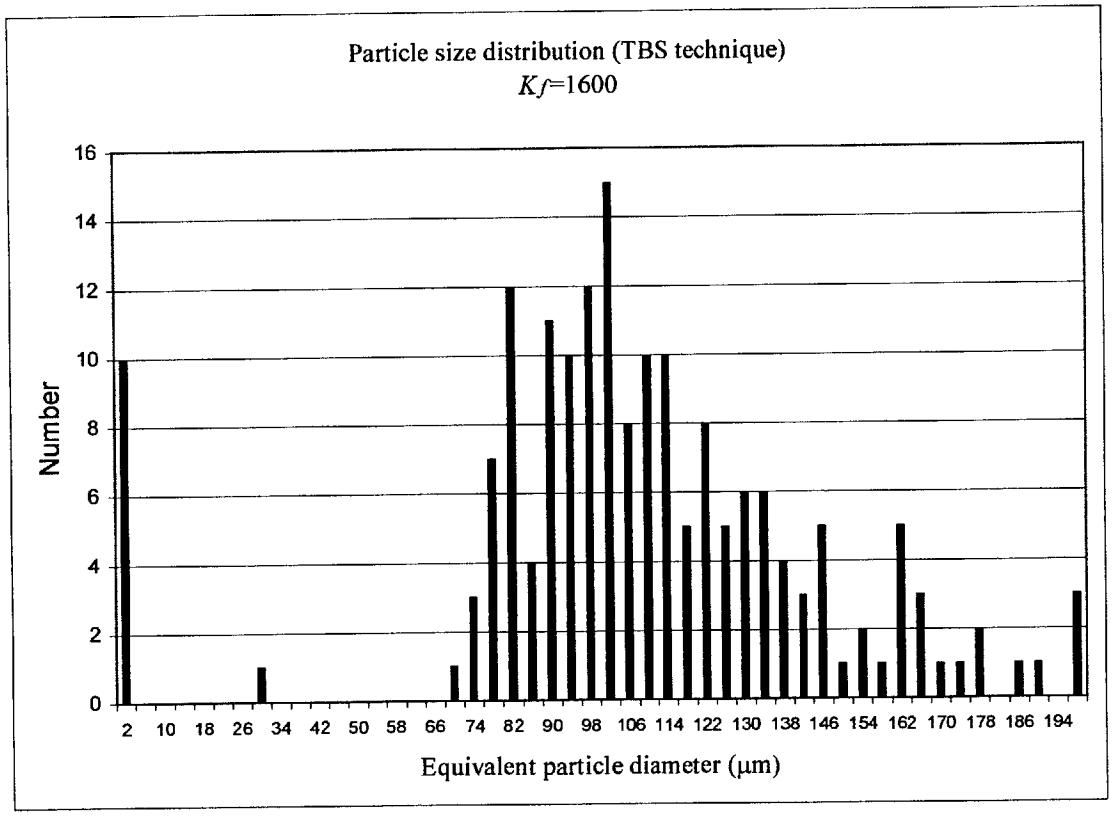

Fig.6.4.g. Size distribution obtained with the TBS technique

The sphericity of the Ballotini particles used for this measurements is plotted in fig.6.4.h. below. This was obtained with the microscope technique mentioned previously. Indeed, we can see that the majority of the particles are nearly perfect spheres (sphericity of 1), while a substantial number of them have values higher than 1.5. There are two main causes for the overestimation of the particle sphericity with the microscope technique. The first one is the genuine non-spherical shape of the particle. The second one is observed when two or more particles are aggregated together on the microscope slide, causing the algorithm to mistake them as one big particle of intricate shape, therefore overestimating the real value of the particle sphericity. However, this latter case was minimised with a special routine in the program.

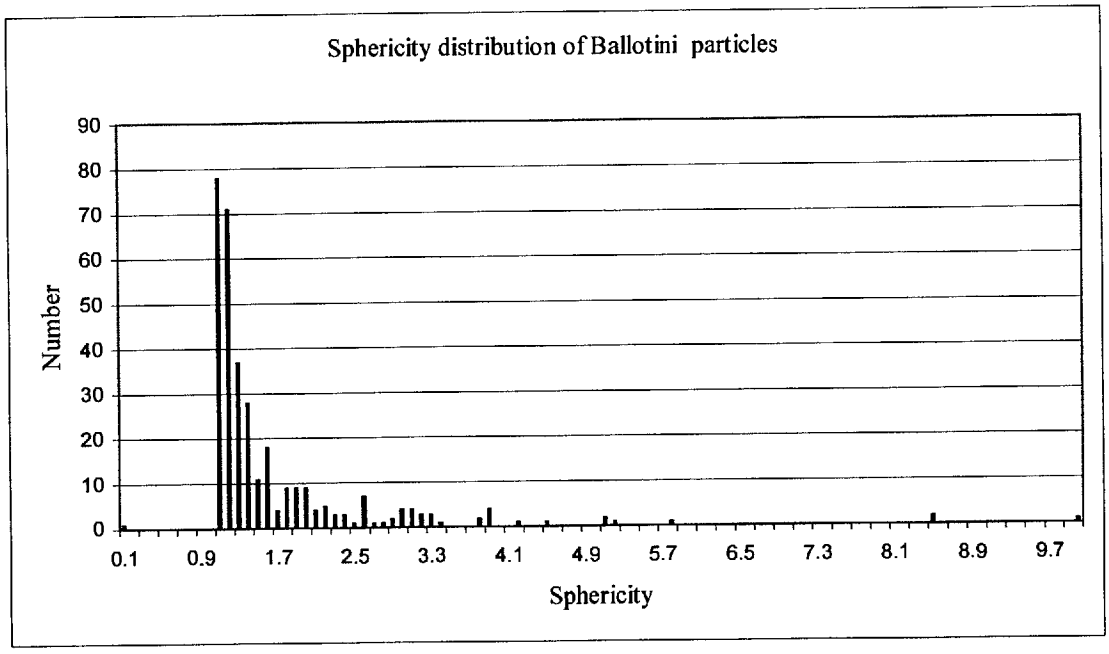

Fig.6.4.h. Sphericity distribution of Ballotini particles.

Thus it can be seen that the presence of non-spherical particles in the test space will induce measured intensities which differ from the Mie theory predicted values. This would be an explanation for the broadening of the size distribution. Note as well that this broadening effect is more emphasized in the result of the Ballotini particle test than in the calibration results, for which the sphericity was certified.

The TBS technique was proven to be successful in estimating particle velocity (<2 m/s) and size (<120 μm). However, because the theory underlying its operating principle is based on the well-known Mie theory, it is restricted to homogeneous spherical particles. Also, it constitutes a simplified optical set up, using a single birefringent crystal and collecting the scattered light at a single angle. Given the oscillations in the calculated scattered intensity relative to particle size are smoothed out due to an appropriate solid angle of collection, this system can be implemented at any angle.

Conclusion.

Summary.

An optical instrument for use in industrial coal-burning furnaces has been designed to measure the carbon content of individual fly ash particles. Using a single laser beam and a simple lens collecting system, this instrument allows the user to target the test space at different locations along the optical axis within the furnace. Because the size of the test space increases with increasing distance, it is best to use it in the range 0-2 m. However, the importance of the size of the test space is also a function of the concentration of the particles in the flow. Because the polarisation ratio technique, to measure the carbon content in fly ash, is aimed at measuring the scattered light signals from individual particles, a bigger test space with a smaller particle flow concentration would yield the same effect as a smaller test space with a bigger particle flow concentration. Thus when using the instrument, one can adapt the size of the test space according to the particle flow concentration by changing the aperture diameter (this determines the width of the test space).

Dr. Karim Ouazzane carried out experiments with the instrument and established a precision of ±1% of carbon-by-mass was achieved for the carbon-in-ash measurements. This precision was improved to ±0.5% of carbon-by-mass when using a Neural Network approach, based on the knowledge a priori of the mineral content of the coal from which the fly ash resulted.

In order to incorporate size and velocity measurements within this instrument, two original techniques were investigated. Firstly, a Grating Projection System (GPS) was designed to produce a square wave illumination pattern in the test space. This was

in order to study the influence of the particle size on the square wave signal generated by its passage through the pattern. The particle velocity was easily deduced from the main harmonic frequency of the scattered light signal. The particle size determination was investigated using the Total Harmonic Distortion (%THD) parameter. The %THD gives a measure of the distortion of the initial square wave by comparing the different weights of the harmonic frequencies in the signal to the weight of the main frequency. Modelling of this parameter was attempted, but its correlation with experimental measurements was uncertain because high oscillations were predicted by the model in the variation of the %THD with particle size. There was evidence that these oscillations were genuine, and the standard deviations in the experimental data were in agreement with the calculations. We did not conclude that this method would be a suitable particle sizing technique, but, nevertheless, is adequate to measure particle velocity.

Secondly, a Two Beam System (TBS) was used to produce an illumination of two orthogonally polarised laser beams, from which the scattered light signal delays and relative amplitudes gave information on the trajectory of the particle. The aim was to avoid the Gaussian beam uncertainty in order to achieve particle sizing by means of an intensity technique. A calibration of the technique was achieved using mono-disperse polymethylmetacrylate (PMMA) spherical particles and an algorithm was used to recover the particle size from the information provided by the scattered signal.

Although well established techniques such as PDA and LDA are commonly used in industrial environment, the conditions to implement these techniques within the carbon-in-ash measurements instrument were not suitable. The particularity of the GPS and TBS techniques is that they can be operated in the backward direction. Also, the

detection system is constituted by a single photomultiplier for the GPS and by two photomultipliers for the TBS. Nevertheless, both techniques collect the scattered light at a single angle.

There is no need to calibrate the GPS to measure the particle velocity, as it is unambiguously directly related to the main harmonic frequency of the scattered light signal. However, its fringe spacing has to be determined accurately. The precision of this technique is then determined by the precision in the positioning of the optics.

The TBS technique allows estimation of the particle velocity and trajectory within the beams. The particle size being recovered through an algorithm based on Mie theory calculations for spherical particles, the precision is therefore dependent on the sphericity of the particles under study. This was discussed previously in section 6. The advantage of this technique is that it can be directly inserted in the carbon-in-ash measurement instrument by adding a simple birefringent prism to produce the Two Beam System. The receiving optics remain unchanged, as in both the polarisation ratio technique and the TBS technique we analyse the two orthogonally polarised light components scattered by the particle.

Suggestions for future work.

Regarding the optical instrument itself, an automated procedure for targeting the test space would be advantageous. Also, special care should be given to the reduction of the instrument weight, through a more compact design of the different optics and internal electronics. A more elaborate visual interface that would incorporate the Neural

Network analysis and the different instrument parameter settings would also reduce considerably the operating time of the instrument. Thus an almost real-time determination of the fly ash carbon content could be achieved.

The %THD technique could be investigated in more depth, by modifying its definition in relation to the different harmonic weights considered. The theory developed in this thesis being exact, it could be the basis of a study to determine a parameter that provides a more linear relationship with respect to the particle size. This could be achieved by analysing different combinations of different harmonic weights, as the %THD theoretical development allows calculation of the weight of each harmonic. Nevertheless, the calibration of the %THD sizing technique would still be restricted to having mono-disperse particle samples. A controlled droplet generator could be considered for this experiment to provide spherical particles of known size.

The Two Beam System was investigated at a fixed angle of 140°. A wider range of scattering angles and related Mie theory calculations would complete the study. Near backward direction angles would be necessary in order to implement the optical probe with this technique. Particles with different absorption coefficients should be investigated as fly ash has generally a higher absorption coefficient than the PMMA particles used in the previous experiments. Also, given that fly ash is not generally of spherical shape, experiments should be carried out with this technique to characterize its response to non-spherical particles.

Appendix I.

%THD distributions

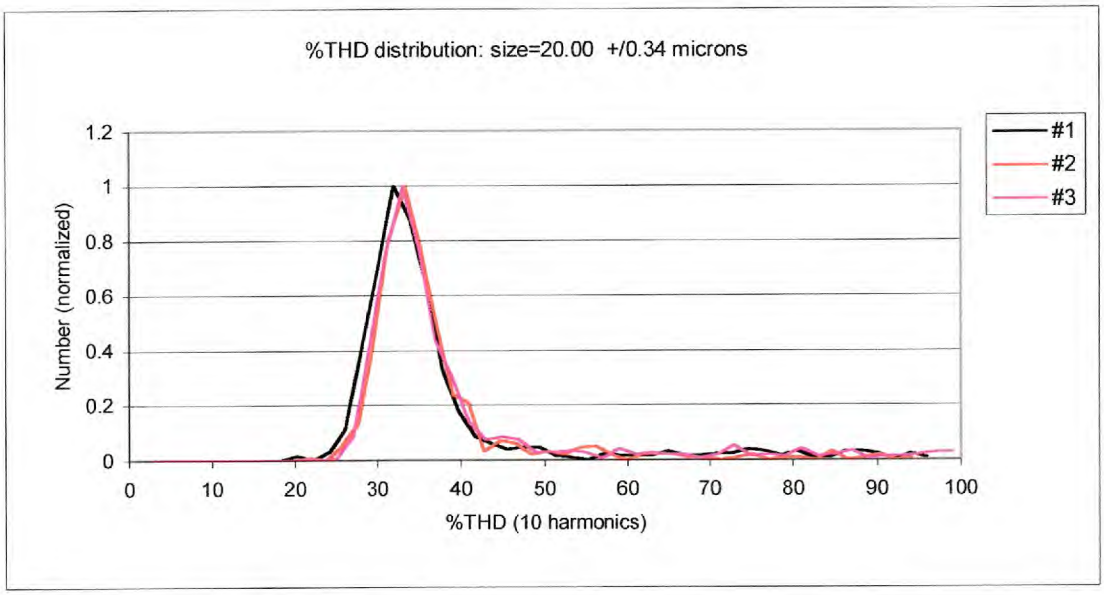

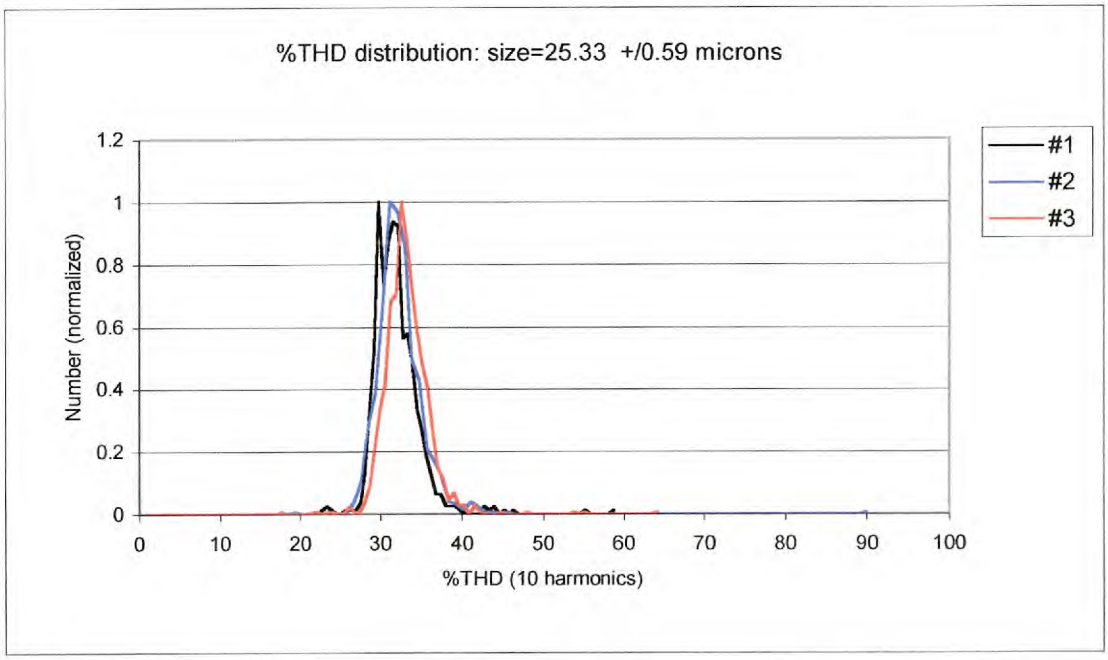

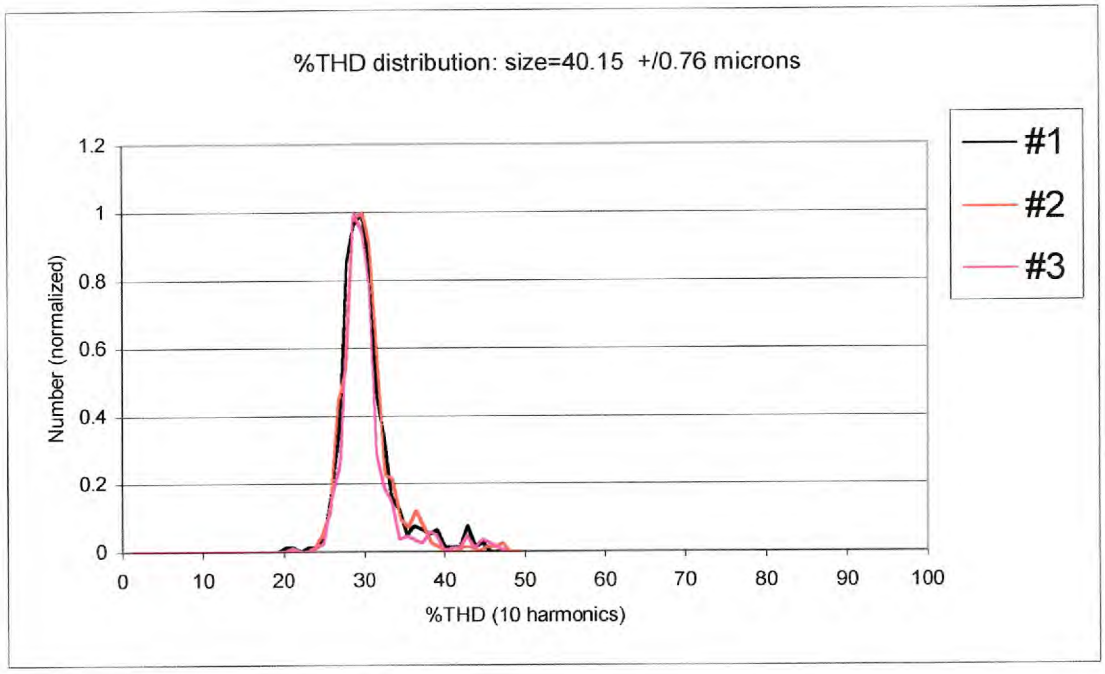
%THD distribution: size=40.15 +/0.76 microns
Number (normalized)
1.2
1
0.8
0.6
0.4
0.2
0
0
10
20
30
40
50
60
70
80
90
100
%THD (10 harmonics)
#1
#2
#3

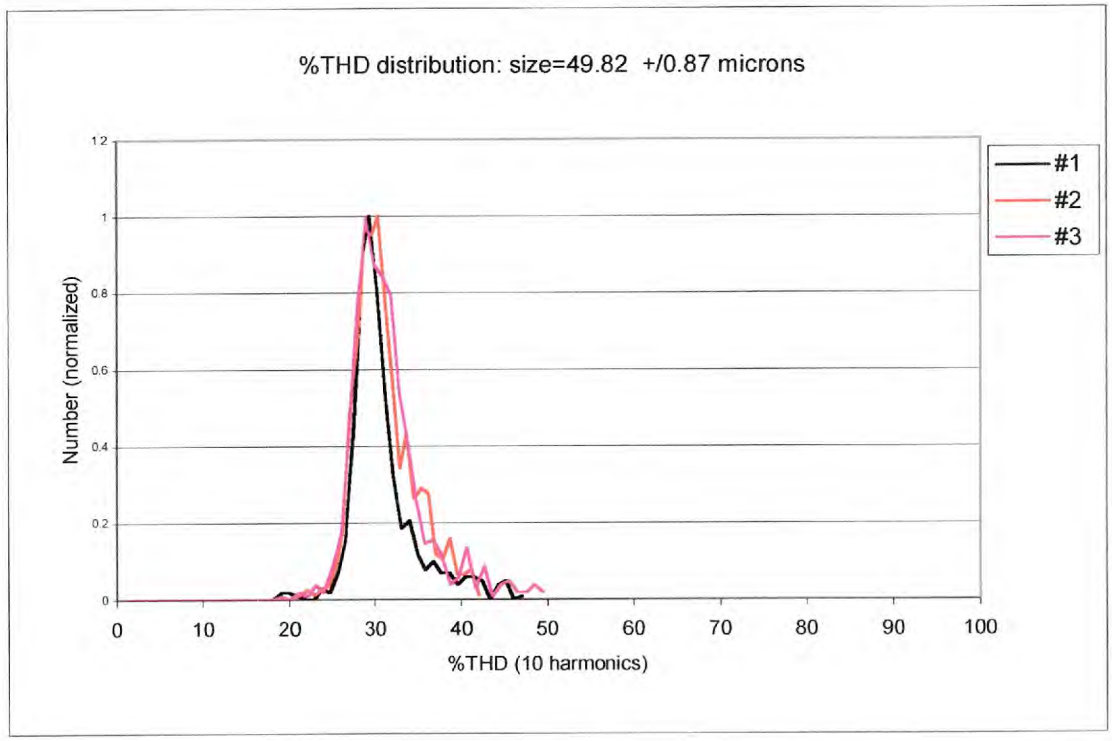
%THD distribution: size=49.82 +/0.87 microns
Number (normalized)
1.2
1
0.8
0.6
0.4
0.2
0
0
10
20
30
40
50
60
70
80
90
100
%THD (10 harmonics)
#1
#2
#3

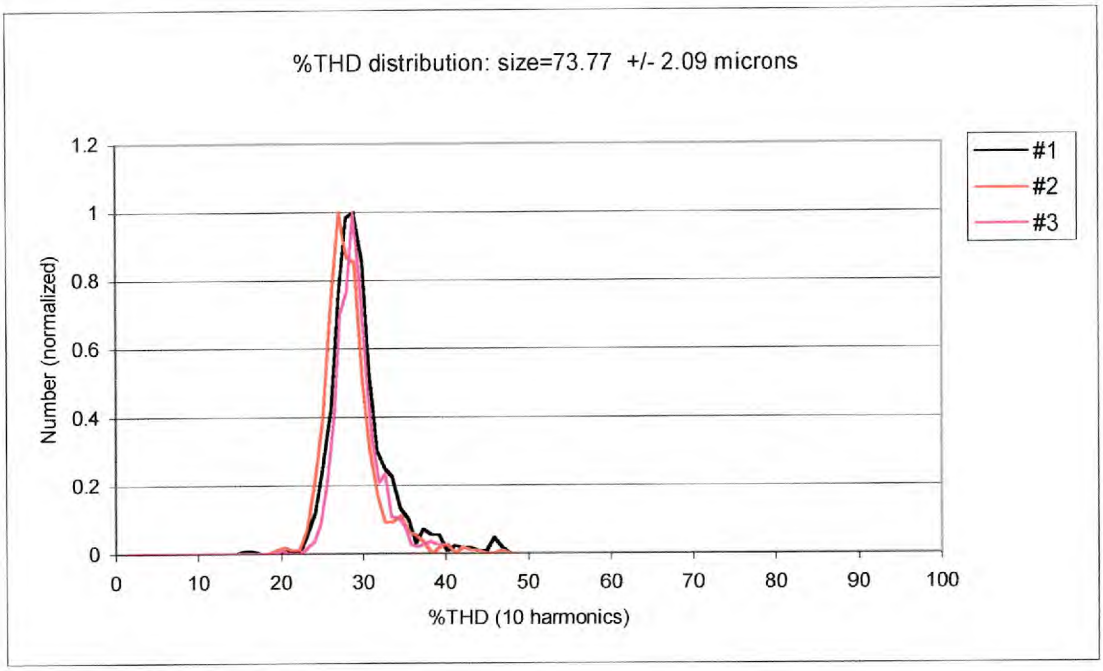
%THD distribution: size=73.77 +/- 2.09 microns
Number (normalized)
1.2
1
0.8
0.6
0.4
0.2
0
0
10
20
30
40
50
60
70
80
90
100
%THD (10 harmonics)
#1
#2
#3

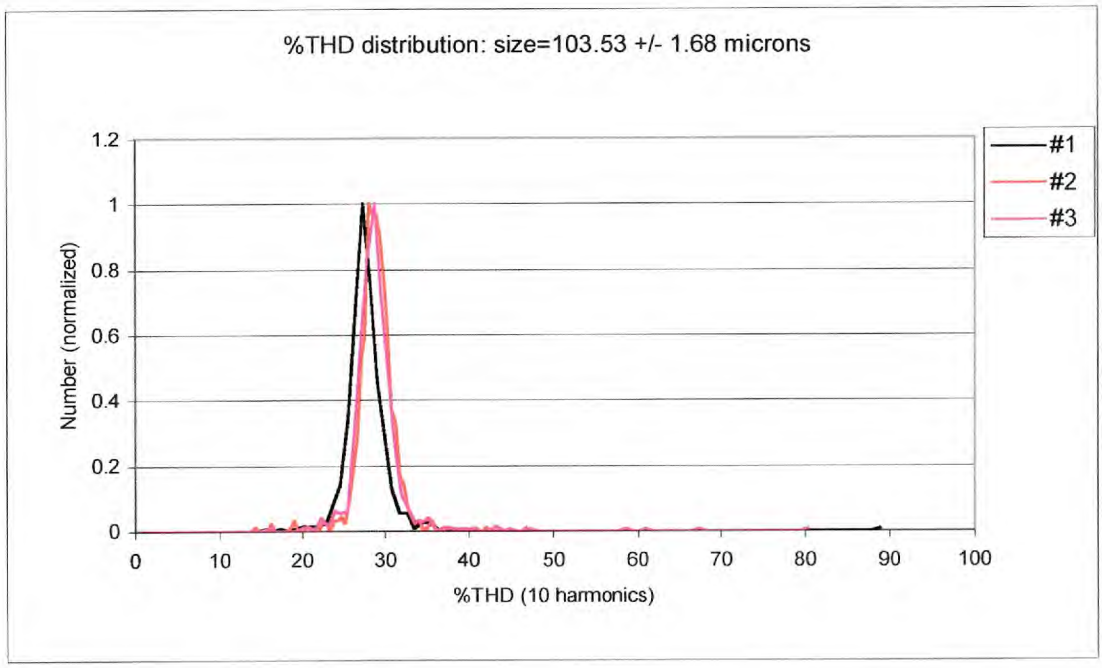
%THD distribution: size=103.53 +/- 1.68 microns
Number (normalized)
1.2
1
0.8
0.6
0.4
0.2
0
0
10
20
30
40
50
60
70
80
90
100
%THD (10 harmonics)
#1
#2
#3

Appendix II.

The Cartesian coordinates (x,y,z) are expressed in terms of spherical coordinates as:

$$\begin{cases} x = r\sin(\theta)\cos(\phi) \\ y = r\sin(\theta)\sin(\phi) \\ z = r\cos(\theta) \end{cases} \quad \text{(Eq.A2.1)}$$

The Cartesian coordinates (x_n,y_n,z_n) are expressed in terms of spherical coordinates as:

$$\begin{cases} x_n = r\sin(\theta_n)\cos(\phi_n) \\ y_n = r\sin(\theta_n)\sin(\phi_n) \\ z_n = r\cos(\theta_n) \end{cases} \quad \text{(Eq.A2.2)}$$

The Cartesian coordinates (x,y,z) are then expressed in function of the Cartesian coordinates (x_n,y_n,z_n) as:

$$\begin{cases} x_n = x \\ y_n = y\cos(\gamma_n) - z\sin(\gamma_n) \\ z_n = z\cos(\gamma_n) + y\sin(\gamma_n) \end{cases} \quad \text{(Eq.A2.3)}$$

Combining Eq.A2.1 and Eq.A2.2 with Eq.A2.3, we find:

$$\begin{cases} x_n = r\sin(\theta)\cos(\phi) \\ y_n = r\sin(\theta)\sin(\phi)\cos(\gamma_n) - r\cos(\theta)\sin(\gamma_n) \\ z_n = r\cos(\theta)\cos(\gamma_n) + r\sin(\theta)\sin(\phi)\sin(\gamma_n) \end{cases} \quad \text{(Eq.A2.4)}$$

Appendix III

```
                        PROGRAM MIESIMTHD
C     **********
C     MIE SCATTERING FROM SQUARE WAVE ILLUMINATION
C     COMPLEX REFRACTIVE INDICES
C     RIP-REF. INDEX PARTICLE
C     RIG-REAL REF. INDEX SURROUNDINGS
C     **********
      IMPLICIT DOUBLE PRECISION (A-H,O-Z)
      PRINT*,'* THIS PROGRAM CALCULATES MIE SCATTERING BY SPHERES *'
      PRINT*,'* ILLUMINATED BY A SQUARE WAVE                      *'
      PRINT*,'* MAXIMUM PARTICLE SIZE PARAMETER IS 1000           *'
      PRINT*,'* COMPLEX INTERNAL REFRACTIVE INDEX                 *'
      PRINT*,'* VARIABLE REAL EXTERNAL REFRACTIVE INDEX           *'

C     ************* MAIN ***************

      OPEN(7,FILE='SCADAT',status='old')
      OPEN(8,FILE='THDfinal_p140t90_400_suite',status='new')
      DO 94 DSP= 83.,100.,0.5
      CALL PARTSIZE(DSP,DS,THD)
      PRINT*,DS,THD
      WRITE(8,*) DS,THD
 94   CONTINUE
      CLOSE(8,STATUS='KEEP')
      STOP
      END

      SUBROUTINE PARTSIZE(DSP,DS,THD)

      IMPLICIT DOUBLE PRECISION(A-H,O-Z)
      COMPLEX*16 RIP,A(2500),B(2500)
      WVL=0.532
      FRNG=200.
      G=DASIN(.5*WVL/FRNG)
      RIP=(1.52,0)
      RIG=1.
      PI=4.*DATAN(1.D+0)
      DS=DSP+0.269345167278
      DSPC=20.
      X=PI*DS/WVL

C     -----INTEGRATION STEP-------
      STEPINT=180./(DSPC*X)
      NSTEPS=10./STEPINT
      RX=2./(X*X)
      IF(X.LE.200.)THEN
      N=2.*X+2.
      ELSE
      N=X+10.
      ENDIF
      TSTEX=0.
      TSTSC=0.
```

```
 2     CALL CABMIE(X,N,RIP,RIG,A,B)
       QEXT=0.
       QSCA=0.
       DO 3 K=2,N
       EN=K-1
       F1=2.*EN+1
       QEXT=QEXT+RX*F1*DBLE(A(K)+B(K))
       F4=A(K)*DCONJG(A(K))+B(K)*DCONJG(B(K))
 3     QSCA=QSCA+RX*F1*F4
       ATST=DABS(TSTEX/QEXT)
       BTST=DABS(ATST-1.)
       CTST=BTST-.1D-06
       IF(CTST)4,4,6
 4     ATST=DABS(TSTSC/QSCA)
       BTST=DABS(ATST-1.)
       CTST=BTST-.1D-06
       IF(CTST)7,7,6
 6     TSTEX=QEXT
       TSTSC=QSCA
       N=N+5
       GO TO 2
 7     QABS=QEXT-QSCA
       CALL FIELDS(WVL,DS,STEPINT,G,FRNG,N,A,B,THD)

 101   FORMAT(5X,1HX,8X,10HREF. INDEX,8X,3HRIG)
 102   FORMAT(2X,F8.3,2(2X,F7.3),2X,F8.5)
 103   FORMAT(6X,4HQEXT,11X,4HQSCA,11X,4HQABS)
 104   FORMAT(3(2X,E13.6))
 110   FORMAT(' ANGLE    INTENSITY')
 120   FORMAT(1X,53(1H*))
 121   FORMAT(1X,1H*,51X,1H*)
 122   FORMAT(1X,53(1H*),///)
       CLOSE(7,STATUS='KEEP')
       RETURN
       END

       SUBROUTINE FIELDS(WVL,DS,STEPINT,G,FRNG,N,A,B,THD)
       IMPLICIT DOUBLE PRECISION (A-H,O-Z)
       CHARACTER*20 FICH(11)
       INTEGER P,MC,NC,M
       COMPLEX*16 A(2500),B(2500)
       DIMENSION FINF(50000),FINI(50000),SUMH(12)
       DIMENSION VINTFC(-5:5,-5:5),VINTFS(-5:5,-5:5),GAMMA(11),TH
      1ETA(50000)
C      ROTATION OF BEAMS IN Y-Z PLANE->1
C      ROTATION OF BEAMS IN X-Z PLANE->2
       IROT=1
C      NUMBER OF PAIRS OF BEAMS TO BE ADDED
C      (UPPER LIMIT OF FOURIER SERIES)?
       NBEAM=5
       PIE=4.*DATAN(1.D+0)
       DO  16 K=-NBEAM,NBEAM
       DO 17 KK=-NBEAM,NBEAM

       VINTFC(K,KK)=0.
       VINTFS(K,KK)=0.
 17    CONTINUE
```

```
 16   CONTINUE
      NSTEPS=5./STEPINT


C     --------PROCEDURE TO SELECT THE PAIR OF BEAMS (MC,NC)-------
      CALL POLAR0(WVL,DS,STEPINT,NBEAM,IROT,G,N,A,B,NSTEPS,PHI,THETA
     1,GAMMA,FICH)
           DO 20 MC=-NBEAM,NBEAM
               DO 21 NC=-NBEAM,NBEAM
                  bn1=0.
                  bn2=0.
             IF(MC.LT.NC) GOTO 21
             CALL PTINTEG(MC,NC,BN1,BN2,NBEAM,NSTEPS,FICH,THETA,GAM
     1MA,stepint,WVL,FRSPC,VINTC,VINTS)
             VINTFC(NC,MC)=VINTC
             VINTFS(NC,MC)=VINTS
21          CONTINUE

20    CONTINUE

C     --------CALCULATION OF THE THD-----------

      SUM0=0.
      DO 56 L=1,2*NBEAM
      SUMH(L)=0.
 56   CONTINUE
      L=0
      DO 25 L=1, 2*NBEAM
      DO 26 M=-NBEAM+L,NBEAM
            DO 27 P=-NBEAM+L,NBEAM
            IF(L.EQ.1) THEN
            SUM0=SUM0+VINTFC(M-1,M)*VINTFC(P-1,P)+VINTFS(M-1,M)*VINT
     1FS(P-1,P)
            GOTO 27
            ENDIF
            SUMH(L)=VINTFC(M-L,M)*VINTFC(P-L,P)+VINTFS(M-L,M)*VIN
     1TFS(P-L,P)+SUMH(L)

 27              CONTINUE
 26          CONTINUE
 25   CONTINUE
      SUMF=0.
      DO 33 L=2,2*NBEAM
      SUMF=SUMH(L)+SUMF
 33   CONTINUE
      THD=DSQRT(SUMF/SUM0)
      RETURN
      END

      SUBROUTINE pOLAR0(WVL,DS,STEPINT,NBEAM,IROT,G,N,A,
     1B,NSTEPS,PHI,THETA,GAMMA,FICH)
C     **********
C     MIE SCATTERING POLAR DIAGRAMS
C     **********
      IMPLICIT DOUBLE PRECISION (A-H,O-Z)
      CHARACTER*20 FICH(11),TFICH
```

```
      COMPLEX*16 A(2500),B(2500),S1,S2,AN,CI,FX1,FY1,FZ1,FX,FY,FZ
      DIMENSION TAU(2500),PI(2500)
      DIMENSION THETA(50000),PHI(50000),GAMMA(21)
      CI=(0.,1.)
      PIE=4.*DATAN(1.D+0)
C     SCATTERING ANGLE (THETA) OF DETECTOR (DEGREES)
      ANGLEINIT=140.
      ANGLEINIP=90.
C     ANGLE OF APERTURE (DELTAD) OF DETECTOR (DEGREES)
      DELTAD=5.
C     VALUE OF INTEGRATION STEP (STEPINT)
      SGA=DSIN(G)
      NN=N+1
      RAD=PIE/180.
      CB=PIE/2.
      Y=0.
      NSTEPS=2.*DELTAD/STEPINT
      DO 20 IANG=1,NSTEPS
      ANGLET=(ANGLEINIT-DELTAD)+DBLE(IANG-1)*STEPINT
      ANGLEP=(ANGLEINIP-DELTAD)+DBLE(IANG-1)*PIE/NSTEPS
      PHI(IANG)=ANGLEP*RAD
      THETA(IANG)=ANGLET*RAD
 20   CONTINUE
      FICH(1)='IMC1'
      FICH(2)='IMC2'
      FICH(3)='IMC3'
      FICH(4)='IMC4'
      FICH(5)='IMC5'
      FICH(6)='IMC6'
      FICH(7)='IMC7'
      FICH(8)='IMC8'
      FICH(9)='IMC9'
      FICH(10)='IMC10'
      FICH(11)='IMC11'
      DO 8 MC=-NBEAM,NBEAM
      IMC=NBEAM+MC+1
      TFICH=FICH(IMC)
      OPEN(6,FILE=TFICH,status='old')
      IF (MC.LT.0) THEN
      SGN=-1.
      ELSE
      SGN=1.
      END IF
      IBEAM=MC
      IMC=NBEAM+MC+1
      XI=DBLE(IBEAM)
      IF(MC.EQ.0) THEN
      AN=.5
      BN=1.
      GAMMA(IMC)=0.
      ELSE
      AN=CDEXP(CI*SGN*(4.*ABS(XI)-2.)*Y)
      CALL SBN(MC,BNC)
      BN=BNC
      GAMMA(IMC)=SGN*DASIN((4.*ABS(XI)-2.)*SGA)
      END IF
      GAMMAP=GAMMA(IMC)
```

```
      DO 23 IANGP=1,NSTEPS
      DO 22 IANGT=1,NSTEPS
      CALL ROTATE(IROT,GAMMAP,THETA(IANGT),PHI(IANGP),THET1,PHI1)
      CALL PITAU(THET1,NN,PI,TAU)
      S1=0.
      S2=0.
      DO 2 K=2,NN
      CAY=K-1
      PROD=(2.*CAY+1.)/(CAY*(CAY+1.))
      S1=S1+PROD*(A(K)*PI(K)+B(K)*TAU(K))
2     S2=S2+PROD*(A(K)*TAU(K)+B(K)*PI(K))
      ct=dcos(thet1)
      st=dsin(thet1)
      cp=dcos(phi1)
      sp=dsin(phi1)
      cg=dcos(GAMMA(IMC))
      sg=dsin(GAMMA(IMC))
      fx1=ct*cp*cp*s2-sp*sp*s1
      fy1=ct*cp*sp*s2+cp*sp*s1
      fz1=-st*cp*s2
      FX=fx1*AN*BN
      FZ=(-fy1*Sg+fz1*Cg)*AN*BN
      FY=(fy1*Cg+fz1*Sg)*AN*BN
     WRITE(6,100)
     DBLE(IANGP),DBLE(IANGT),DBLE(FX),DIMAG(FX),DBLE(FY),D
    1IMAG(FY),DBLE(FZ),DIMAG(FZ)

22    CONTINUE
23    CONTINUE
      REWIND(6)
      CLOSE(6,STATUS='KEEP')
8     CONTINUE
100   FORMAT(8(2X,E13.6))
      RETURN
      END
      SUBROUTINE ROTATE(IROT,GAMP,THETA,PHI,THET1,PHI1)
      IMPLICIT DOUBLE PRECISION (A-H,O-Z)
      PI2=2.*DATAN(1.D+0)
      IF(IROT.EQ.1)THEN
      IF(PHI.EQ.PI2)THEN
      PHI1=PHI
      THET1=THETA-GAMP
      GO TO 1
      ENDIF
      IF(THETA.EQ.0.)THEN
      PHI1=PI2
      THET1=-GAMP
      GO TO 1
      ENDIF
      CS=DSIN(THETA)*DSIN(PHI)*DSIN(GAMP)+DCOS(THETA)*DCOS(GAMP)
      THET1=DACOS(CS)
      TP=DTAN(PHI)*DCOS(GAMP)-DSIN(GAMP)/(DTAN(THETA)*DCOS(PHI))
      PHI1=DATAN(TP)
      ELSE
      CS=DSIN(THETA)*DCOS(PHI)*DSIN(GAMP)+DCOS(THETA)*DCOS(GAMP)
      THET1=DACOS(CS)
```

```
      TP=DTAN(THETA)*DSIN(PHI)/(DTAN(THETA)*DCOS(PHI)*DCOS(GAMP)-
      DSIN(GA
     1MP))
      PHI1=DATAN(TP)
      ENDIF
 1    CONTINUE
      RETURN
      END
      SUBROUTINE CABMIE(X,N,RIP,RIG,A,B)
C     **********
C     CALCULATES MIE EXPANSION COEFFICIENTS
C     **********
      IMPLICIT DOUBLE PRECISION (A-H,O-Z)
      COMPLEX*16 BHZ,ZETAZ,DBH,A(2500),B(2500),A1,A2,B1,B2,DZETAZ
      COMPLEX*16 Y,DBJ,DBY,CI,RIP,RATIO(2500)
      DIMENSION BJZ(2500),BYZ(2500)
      CI=DCMPLX(0.,1.)
      NN=N+1
      Y=RIP*X
      Z=RIG*X
      RZ=1./Z
      CALL BESRAT(Y,NN,RATIO)
      CALL BESSEL(Z,NN,BJZ,BYZ)
      DO 1 K=1,NN
      EN=K-1
      PSIZ=Z*BJZ(K)
      BHZ=DCMPLX(BJZ(K),-BYZ(K))
      ZETAZ=Z*BHZ
      DRJ=EN*RZ*BJZ(K)-BJZ(K+1)
      DRY=EN*RZ*BYZ(K)-BYZ(K+1)
      DPSIZ=Z*DRJ+BJZ(K)
      DBH=DRJ-CI*DRY
      DZETAZ=Z*DBH+BHZ
      B1=RIP*RATIO(K)*PSIZ-RIG*DPSIZ
      B2=RIP*RATIO(K)*ZETAZ-RIG*DZETAZ
      B(K)=B1/B2
      A1=RIG*RATIO(K)*PSIZ-RIP*DPSIZ
      A2=RIG*RATIO(K)*ZETAZ-RIP*DZETAZ
 1    A(K)=A1/A2
      RETURN
      END
      SUBROUTINE BESSEL(X,N,BJ,BY)
C     **********
C     SPHERICAL BESSEL FUNCTIONS OF REAL ARGUMENT
C     ***********
      IMPLICIT DOUBLE PRECISION  (A-H,O-Z)
      DIMENSION BJ(2500),BY(2500)
      EN=N
      NP=N-1
      K=3.*X+3.
 5    KP=K-1
      F=0.
      DO 1 I=1,KP
      S=K-I+1
 1    F=1./((2.*(EN+S)-1.)/X-F)
      BJ(N)=(2.*EN+1.)/X-F
      F=EN
```

```
      DO 2 I=1,NP
      BJ(N-I)=(2.*F-1.)/X-1./BJ(N-I+1)
 2    F=F-1.
      SJ=DSIN(X)/X
      DO 3 I=1,N
      PJ=SJ/BJ(I)
      BJ(I)=SJ
 3    SJ=PJ
      BJ(N+1)=0.
      SJ=DSIN(X)/(X*X)-DCOS(X)/X
      IF(DABS((BJ(2)-SJ)/SJ).LT.1.E-09)GO TO 4
      K=K+3
      GO TO 5
 4    BY(1)=-DCOS(X)/X
      DO 6 I=2,N+1
 6    BY(I)=(BY(I-1)*BJ(I)-1./(X*X))/BJ(I-1)
      RETURN
      END
      SUBROUTINE PITAU(THETA,N,PI,TAU)
C     **********
C     MIE FUNCTIONS PI(COS) AND TAU(COS)
C     **********
      IMPLICIT DOUBLE PRECISION (A-H,O-Z)
      DIMENSION PI(2500),PIP(2500),TAU(2500)
      NN=N+1
      COTH=DCOS(THETA)
      SITH=DSIN(THETA)
      SITH2=SITH*SITH
      PI(1)=0.
      PI(2)=1.
      PI(3)=3.*COTH
      PIP(1)=0.
      PIP(2)=0.
      PIP(3)=3.
      DO 1 K=3,NN
      CAY=K-1
      PI(K+1)=((2.*CAY+1.)*COTH*PI(K)-(CAY+1.)*PI(K-1))/CAY
 1    PIP(K+1)=((2.*CAY+1.)*COTH*PIP(K)-(CAY+2.)*PIP(K-1))/(CAY-1.)
      DO 2 K=1,NN
 2    TAU(K)=COTH*PI(K)-SITH2*PIP(K)
      RETURN
      END

      SUBROUTINE BESRAT(X,NK,RATIO)
C     **********
C     RATIO OF DERIVATIVE OF RICATTI-BESSEL FUNCTION TO
C     RICATTI-BESSEL FUNCTION BY BACKWARD RECURRENCE
C     **********
      IMPLICIT DOUBLE PRECISION (A-H,O-Z)
      COMPLEX*16 X,R,R1,F,TEST,RATIO(2500),CI,A1,A2,RECIP
      Q=DBLE(.5*CDABS(X))/DTAN(DBLE(1.))
      SQ=DBLE(IDINT(Q+.5))
      SD=SQ*2.E-03
      IF(DABS(Q-SQ).LE.SD)THEN
      QTST=.1E-08
      ELSE
      QTST=.1E-11
```

```
      ENDIF
      XX=CDABS(X)
      INT=IFIX(.5*((ALOG(1.E-08)/ALOG(REAL(XX)/(2.*FLOAT(NK))))-1.))
      IF(INT.LT.0)INT=NK/10
      NMAX=NK+INT
      ALPHA=DBLE(X)
      BETA=DIMAG(X)
      CI=(0.,1.)
      A1=CDEXP(CI*ALPHA)
      A2=1./A1
      IF(BETA.GE.0.)THEN
      B1=1.
      B2=DEXP(-2.*BETA)
      ELSE
      B1=DEXP(2.*BETA)
      B2=1.
      ENDIF
      RECIP=1./(A1*B1-A2*B2)
      TEST=CI*(A1*B1+A2*B2)*RECIP
      K=0
1     R1=0.
      N=NMAX
2     F=(1+N)/X
      R=F-1./(F+R1)
      IF(N+1.LE.NK)THEN
      RATIO(N+1)=R
      ENDIF
      R1=R
      N=N-1
      IF(N.GE.0)GO TO 2
      ATST=DABS(CDABS(TEST/R)-DBLE(1.))-QTST
      IF(ATST.LE.0.)THEN
      K=1
      ELSE
      NMAX=NMAX+10
      ENDIF
      IF(K.EQ.0)GO TO 1
      RETURN
      END
      SUBROUTINE PTINTEG(MC,NC,BN1,BN2,NBEAM,NSTEPS,FICH,THETA,GAMMA,
     1STEPINT,WVL,FRSPC,VINTC,VINTS)

      IMPLICIT DOUBLE PRECISION (A-H,O-Z)
      CHARACTER*20 FICH(11),TFICH1,TFICH2
      COMPLEX*16 X1,X2,Y1,Y2,Z1,Z2
      DIMENSION GAMMA(21),BPRFC(50000),PRFC(50000),PRFS(50000),
     1THETA(50000)
      DIMENSION BPRFS(50000),APRFC(50000),APRFS(50000)
      DO 17 K=1,50000
      APRFC(K)=0.
      APRFS(K)=0.
      BPRFC(K)=0.
      BPRFS(K)=0.
17    CONTINUE
      SUMF=0.
      PRFX=(0.,0.)
      PRFY=(0.,0.)
```

```
      PRFZ=(0.,0.)
      PIE=4.*DATAN(1.D+0)
      CB=PIE/2
      IMC=NBEAM+MC+1
      INC=NBEAM+NC+1
      TFICH1=FICH(IMC)
      TFICH2=FICH(INC)
      OPEN(3,FILE=TFICH1,STATUS='OLD')
      OPEN(4,FILE=TFICH2,STATUS='OLD')
      NA=0
      DO 23 IANGP=1,NSTEPS
      DO 22 IANGT=1,NSTEPS
      NA=NA+1
      READ(3,100) ANGP1,ANGT1,XR1,XI1,YR1,YI1,ZR1,ZI1
      READ(4,100) ANGP2,ANGT2,XR2,XI2,YR2,YI2,ZR2,ZI2
      ATX=DATAN((XR1*XI2-XI1*XR2)/(XR1*XR2+XI1*XI2))
      PRFX=DSQRT((XR1*XR2+XI1*XI2)**2+(XR1*XI2-XI1*XR2)**2)
      PRFXC=PRFX*(DCOS(ATX))
      PRFXS=PRFX*(DSIN(ATX))
      RRR=YR1*YR2+YI1*YI2
      IF(RRR.EQ.0.) THEN
      IF((YR1*YI2-YI1*YR2).GE.0.) THEN
      SII=1.
      ELSE
      SII=-1.
      ENDIF
      ATY=SII*PIE/2.
      GO TO 45
      ENDIF
      ATY=DATAN((YR1*YI2-YI1*YR2)/(YR1*YR2+YI1*YI2))
45    PRFY=DSQRT((YR1*YR2+YI1*YI2)**2+(YR1*YI2-YI1*YR2)**2)
      PRFYC=PRFY*(DCOS(ATY))
      PRFYS=PRFY*(DSIN(ATY))
      ATZ=DATAN((ZR1*ZI2-ZI1*ZR2)/(ZR1*ZR2+ZI1*ZI2))
      PRFZ=DSQRT((ZR1*ZR2+ZI1*ZI2)**2+(ZR1*ZI2-ZI1*ZR2)**2)
      PRFZC=PRFZ*(DCOS(ATZ))
      PRFZS=PRFZ*(DSIN(ATZ))
C      PRFC(IANGT)=DBLE(IANGT)/(NSTEPS)
      PRFC(IANGT)=PRFXC+PRFYC+PRFZC
      PRFS(IANGT)=PRFXS+PRFYS+PRFZS

 22   CONTINUE
      VINTPT=0.
      R1=DBLE(IANGP/2.)
      R2=DBLE(IANGT/2.)
      IF((R1-INT(R1)).GT.0.01) THEN
      CALL PTINTF(APRFC,APRFS,BPRFC,BPRFS,PRFC,PRFS,THETA,
     1NSTEPS,VINTPTC,VINTPTS)
      ENDIF
      SUMFC=SUMFC+(1./9.)*VINTPTC*(STEPINT**2)
      SUMFS=SUMFS+(1./9.)*VINTPTS*(STEPINT**2)
      DO 14 IANGTT=1,NSTEPS
      APRFC(IANGTT)=BPRFC(IANGTT)
      APRFS(IANGTT)=BPRFS(IANGTT)
      BPRFC(IANGTT)=PRFC(IANGTT)
      BPRFS(IANGTT)=PRFS(IANGTT)
```

```
 14    CONTINUE
 23    CONTINUE
       VINTC=(SUMFC*CB)
       VINTS=(SUMFS*CB)
       SUMFC=0.
       SUMFS=0.
C      FRSPC=WVL/ABS(DSIN(GAMMA(IMC))-DSIN(GAMMA(INC)))
       CLOSE(3,STATUS='KEEP')
       CLOSE(4,STATUS='KEEP')
 100   FORMAT(8(2X,E13.6))
       RETURN
       END

       SUBROUTINE PTINTF(APRFC,APRFS,BPRFC,BPRFS,PPRFC,PPRFS,THETA,
      1NSTEPS,VINTPTC,VINTPTS)

       IMPLICIT DOUBLE PRECISION(A-H,O-Z)
       dimension PPRFC(50000),PPRFS(50000)
       DIMENSION BPRFC(50000),BPRFS(50000)
       DIMENSION APRFC(50000),APRFS(50000)
       dimension theta(50000)
       SUMPRC=0.
       SUMPRS=0.
       PI=4.*DATAN(1.D+0)
       DO 13 IANGT2=2,NSTEPS-1,2
       SUMPOC=16.*BPRFC(IANGT2)+4.*(BPRFC(IANGT2-1)+BPRFC(IANGT2+1)
      1+PPRFC(IANGT2)+APRFC(IANGT2))+PPRFC(IANGT2-1)+PPRFC(IANGT2+1)
      1+APRFC(IANGT2+1)+APRFC(IANGT2-1)
       SUMPOS=16.*BPRFS(IANGT2)+4.*(BPRFS(IANGT2-1)+BPRFS(IANGT2+1)
      1+PPRFS(IANGT2)+APRFS(IANGT2))+PPRFS(IANGT2-1)+PPRFS(IANGT2+1)
      1+APRFS(IANGT2+1)+APRFS(IANGT2-1)
       ANGLE=THETA(IANGT2)
       CC=(DSIN(ANGLE))
       SUMPRC=SUMPRC+SUMPOC*CC
       SUMPRS=SUMPRS+SUMPOS*CC

 13    CONTINUE
       VINTPTC=SUMPRC
       VINTPTS=SUMPRS

       RETURN
       END
       SUBROUTINE SBN(M,BNC)
       IMPLICIT DOUBLE PRECISION (A-H,O-Z)
       PI=4.*DATAN(1.D+0)
       IF(M.EQ.0) THEN
       BNC=1.
       GOTO 29
       ENDIF
       BNC=((-1)**(ABS(M)-1)/((2.*DBLE(ABS(M))-1.)*PI))
 29    RETURN
       END
```

Appendix IV.

TBS simulations

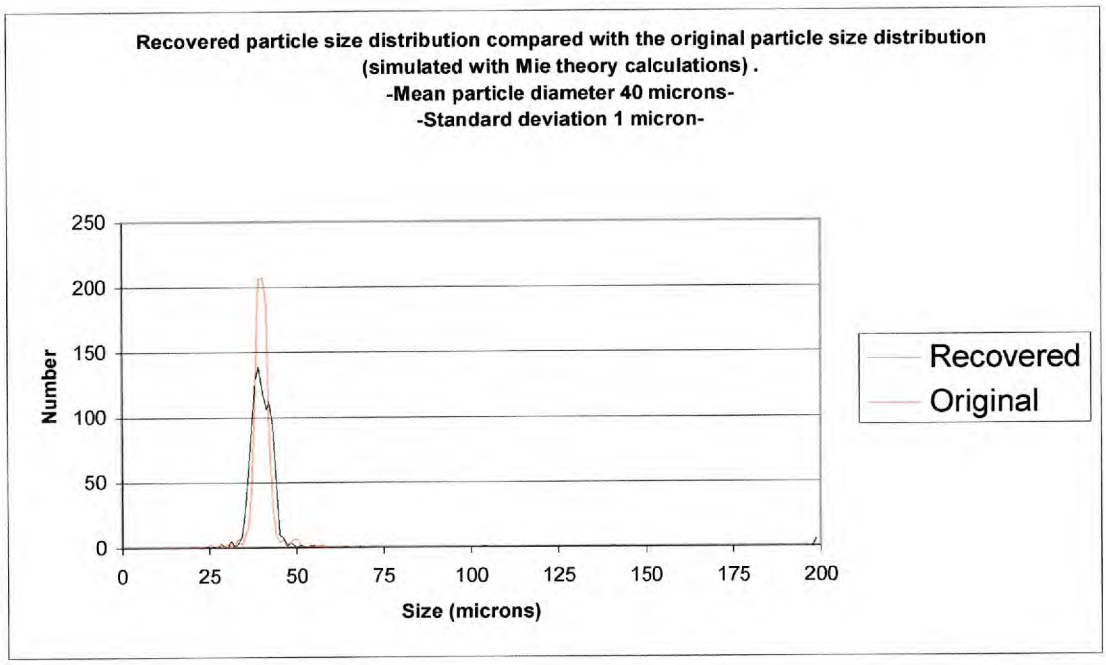

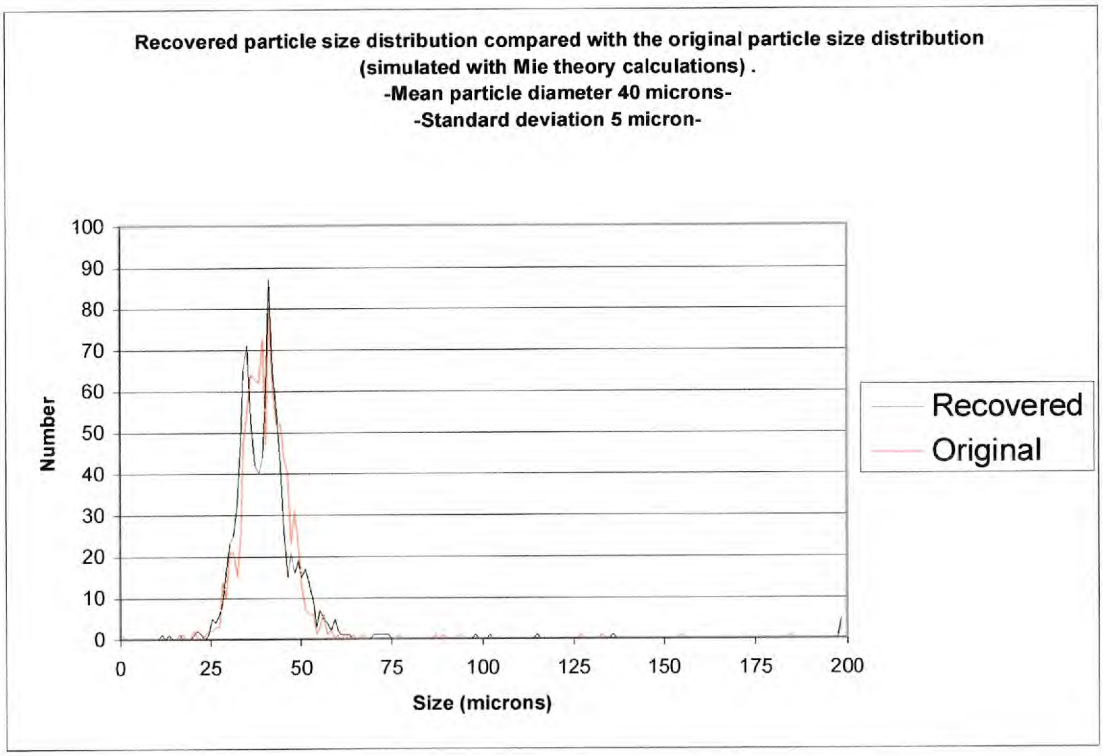

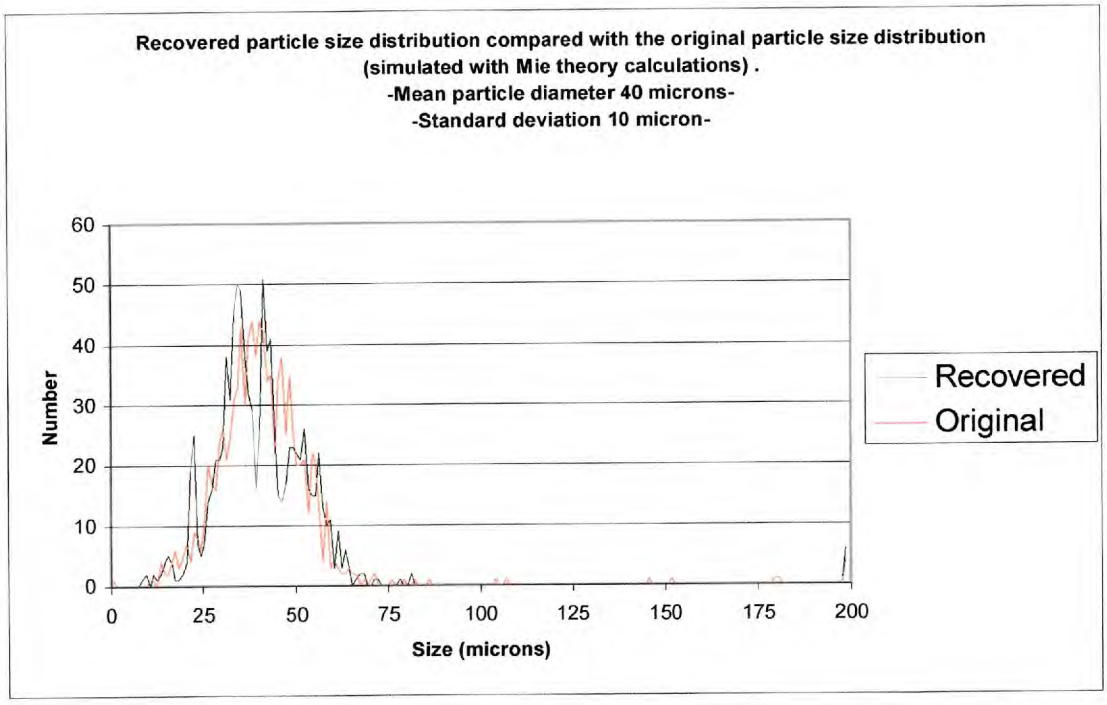
Recovered particle size distribution compared with the original particle size distribution
(simulated with Mie theory calculations) .
-Mean particle diameter 40 microns-
-Standard deviation 10 micron-
Number
Size (microns)
0
10
20
30
40
50
60
0
25
50
75
100
125
150
175
200
Recovered
Original

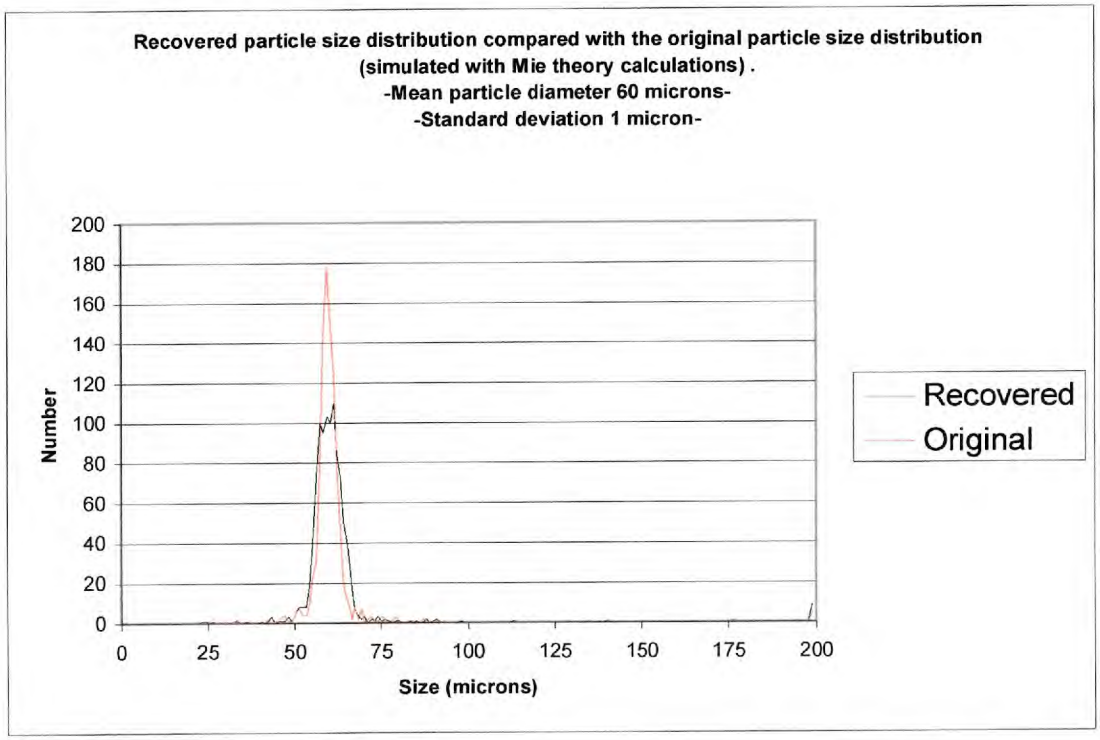
Recovered particle size distribution compared with the original particle size distribution
(simulated with Mie theory calculations) .
-Mean particle diameter 60 microns-
-Standard deviation 1 micron-
Number
Size (microns)
0
20
40
60
80
100
120
140
160
180
200
0
25
50
75
100
125
150
175
200
Recovered
Original

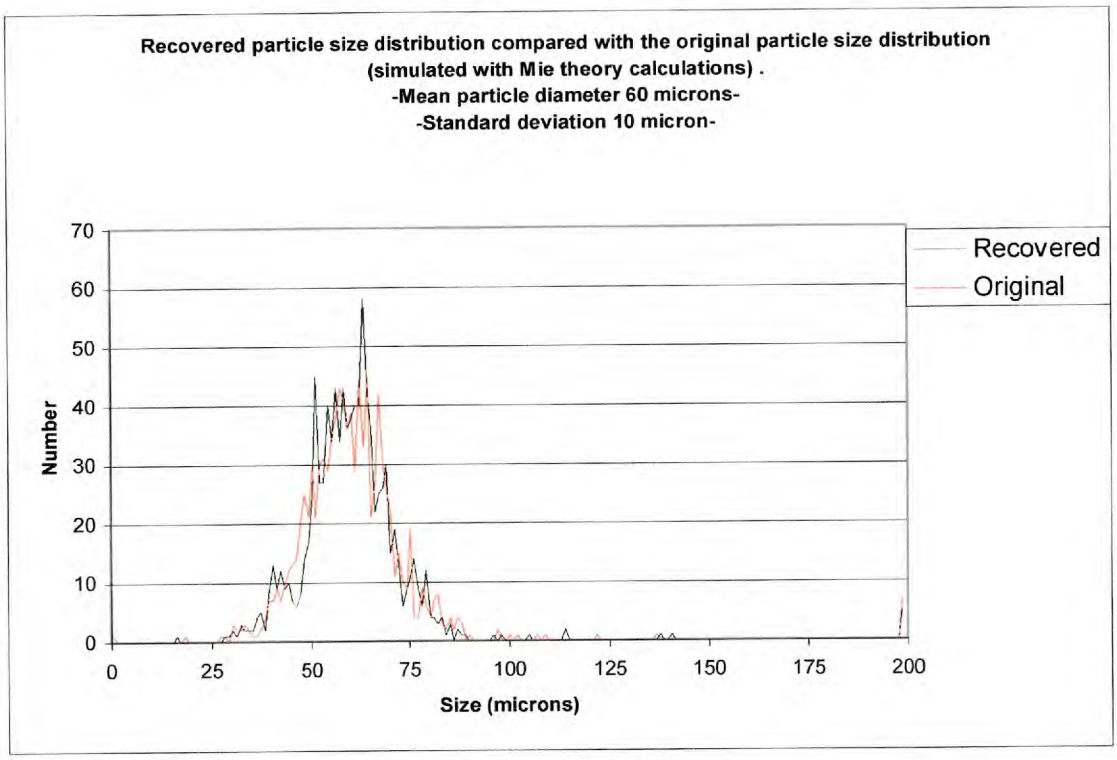
Recovered particle size distribution compared with the original particle size distribution
(simulated with Mie theory calculations) .
-Mean particle diameter 60 microns-
-Standard deviation 10 micron-
Number
Size (microns)
Recovered
Original
0
10
20
30
40
50
60
70
0
25
50
75
100
125
150
175
200

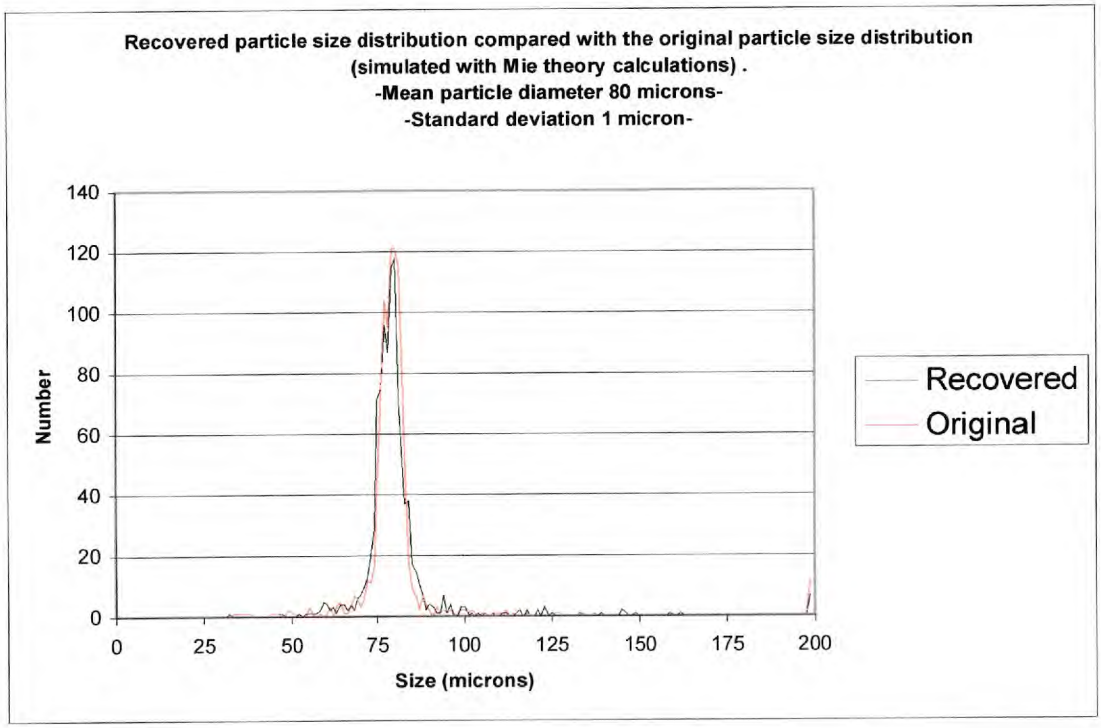
Recovered particle size distribution compared with the original particle size distribution
(simulated with Mie theory calculations) .
-Mean particle diameter 80 microns-
-Standard deviation 1 micron-
Number
Size (microns)
Recovered
Original
0
20
40
60
80
100
120
140
0
25
50
75
100
125
150
175
200

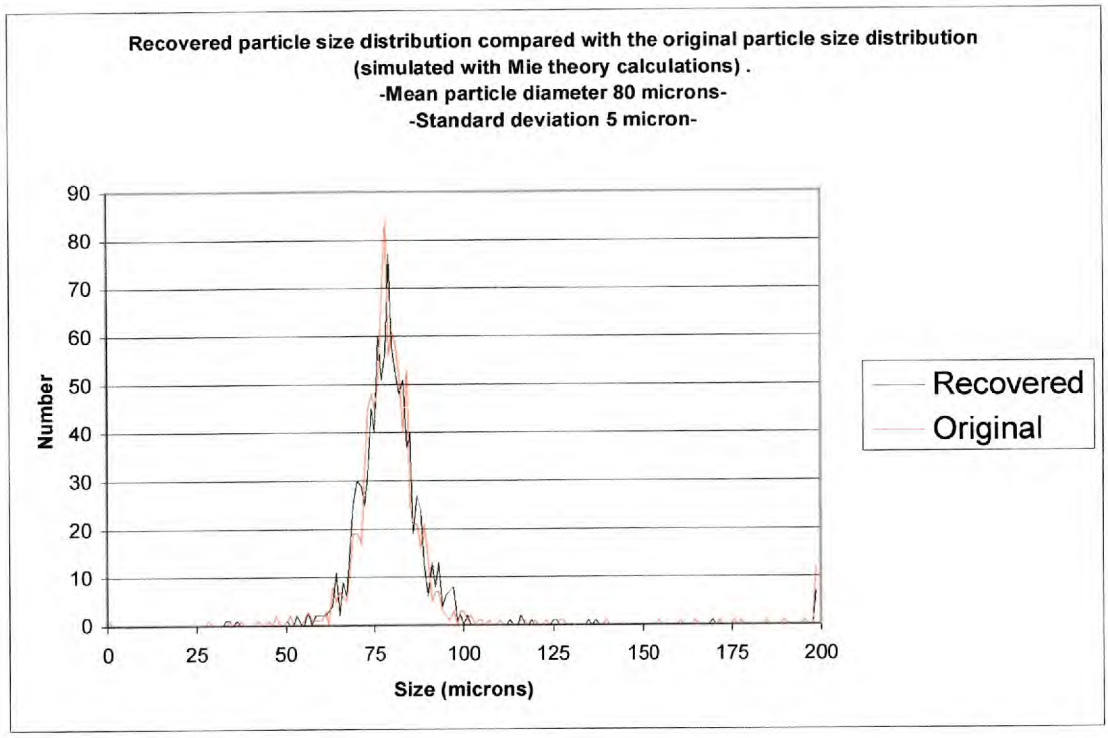
Recovered particle size distribution compared with the original particle size distribution
(simulated with Mie theory calculations) .
-Mean particle diameter 80 microns-
-Standard deviation 5 micron-
Number
Size (microns)
Recovered
Original

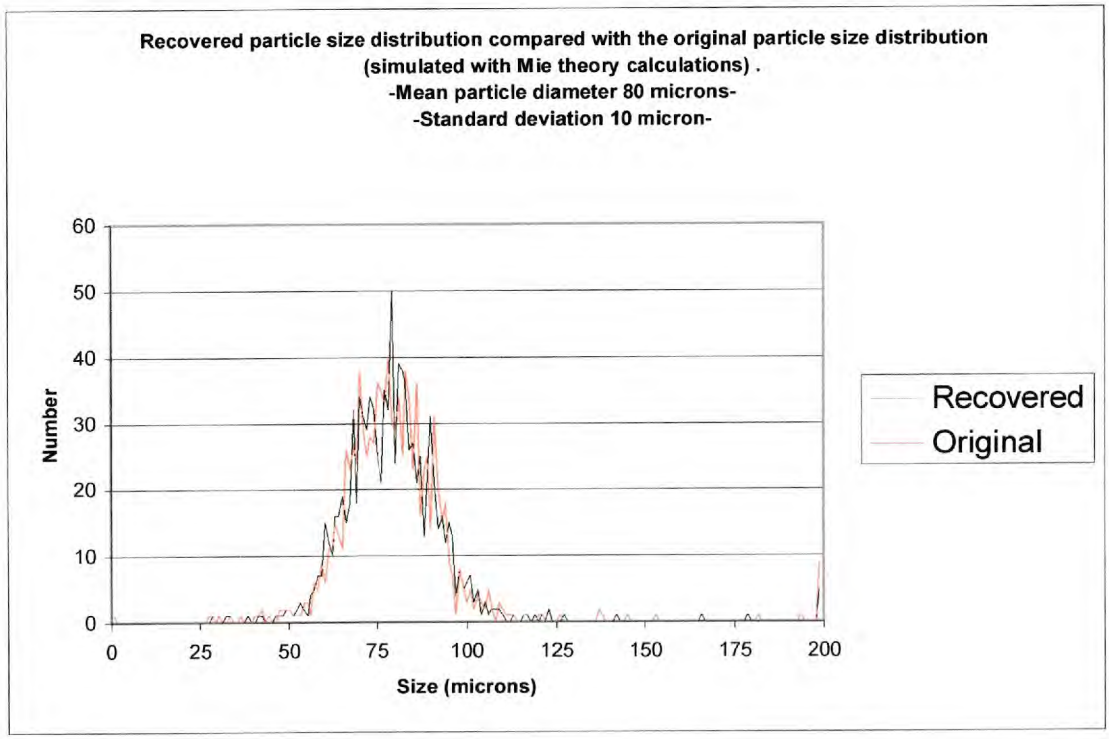
Recovered particle size distribution compared with the original particle size distribution
(simulated with Mie theory calculations) .
-Mean particle diameter 80 microns-
-Standard deviation 10 micron-
Number
Size (microns)
Recovered
Original

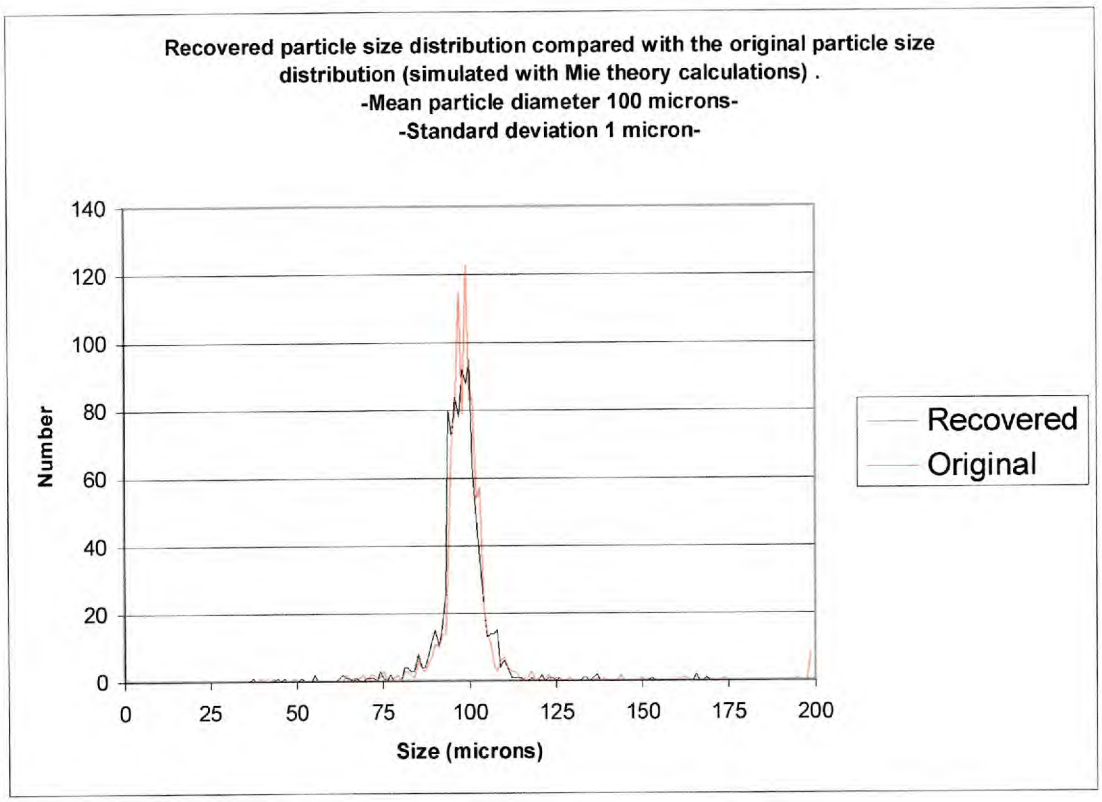
Recovered particle size distribution compared with the original particle size distribution (simulated with Mie theory calculations) .
-Mean particle diameter 100 microns-
-Standard deviation 1 micron-
Number
Size (microns)
Recovered
Original

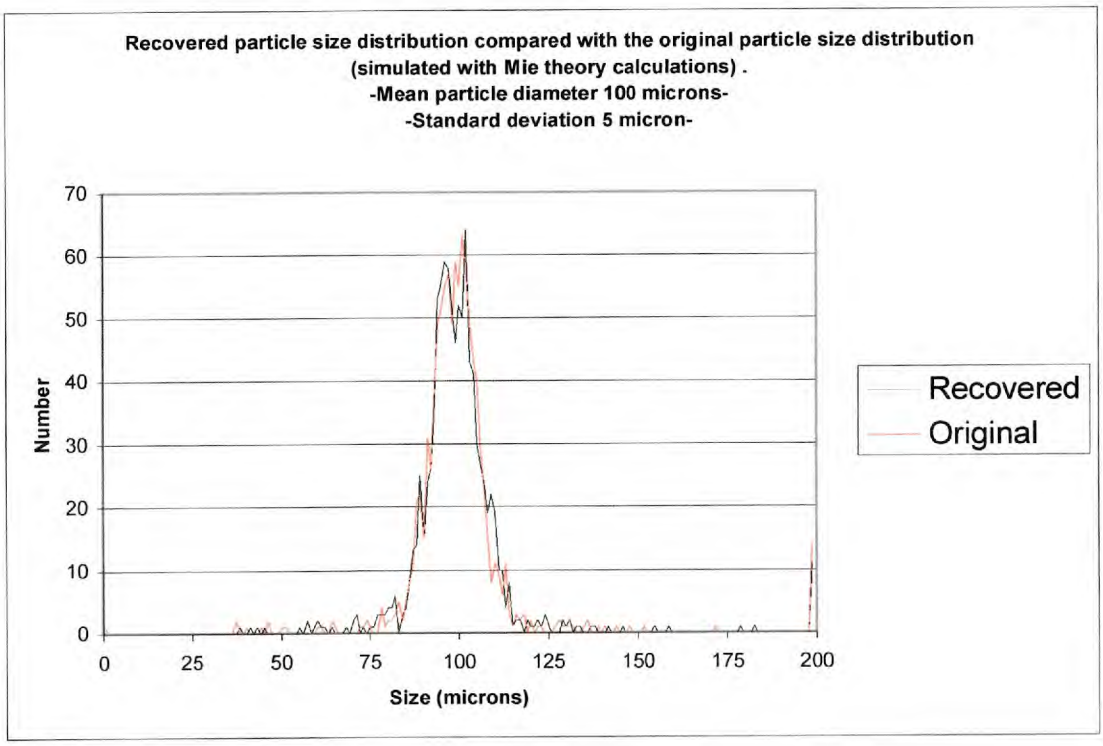
Recovered particle size distribution compared with the original particle size distribution (simulated with Mie theory calculations) .
-Mean particle diameter 100 microns-
-Standard deviation 5 micron-
Number
Size (microns)
Recovered
Original

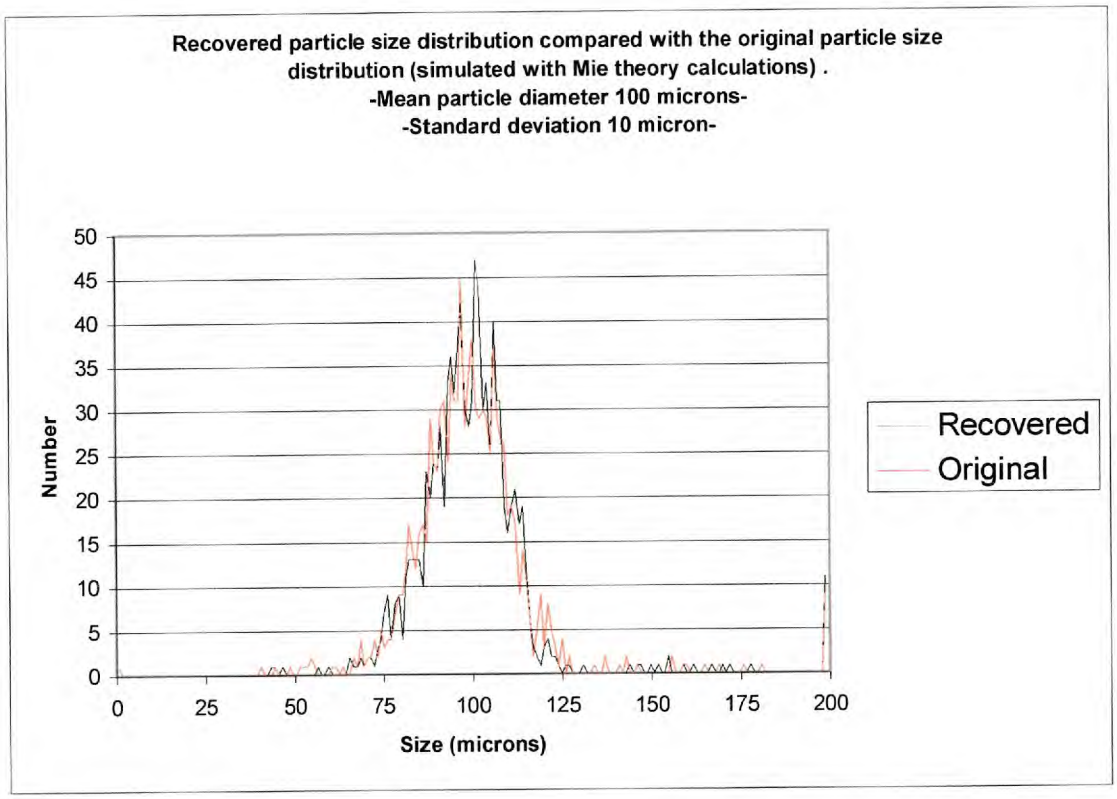
Recovered particle size distribution compared with the original particle size distribution (simulated with Mie theory calculations) .
-Mean particle diameter 100 microns-
-Standard deviation 10 micron-
Number
50
45
40
35
30
25
20
15
10
5
0
0
25
50
75
100
125
150
175
200
Size (microns)
Recovered
Original

References.

[I.1] R. Semiat, E. Leshinski, A.Orell, "Laser grating technique for measurement of local velocity of large drops and jets in liquid-liquid systems", Chem. Eng. Sci. 51-23 (1996), 5111-5123.

[1.1] M. Kerker, "The scattering of light", New York, Academic Press, 1969.

[1.2] A. Ungut, A.J. Yule, D.S. Taylor, N.A.Chigier, "Particle size measurement by laser anemometry", J.Energy 2 (1978), 330-336.

[1.3] B. Chu, "Laser light scattering", New York, Academic Press, 1974, p156.

[1.4] A.R. Jones, "Light scattering for particle characterization", Progress in Energy and Combustion Science 25 (1999), 1-53.

[1.5] D.J. Holve, S.A. Self, "Optical particle sizing for in-situ measurements Part I", Applied Optics 18 (1979), 1632-1645.

[1.6] D.J. Holve, S.A. Self, "Optical particle sizing for in-situ measurements Part II", Applied Optics 18 (1979), 1646-1652.

[1.7] B. Rose et al, "Effects of target structure on the performance of laser time-of-flight velocimeter systems", Applied Optics 36 (1997), 518-533.

[1.8] L.L. Baxter, "Char fragmentation and fly ash formation during pulverized-coal combustion", Combust. Flame 90 (1992), 174-184.

[1.9] C.F. Hess, "Non intrusive optical single-particle counter for measuring the size and velocity of droplets in a spray", Applied Optics 23 (1984), 4375-4382.

[1.10] J.R. Fincke et al, "Simultaneous measurement of particle size, velocity and temperature", Mea. Sci. Technol. 4 (1993), 559-565.

[1.11] G.W. Xie, P. Scott, D.T. Shaw, Y.M. Zhang, Optics Letters 16 (1991), 861-863.

[1.12] J. Pu, H. Zhang, "Aberrated lenses for generating flattened laser irradiance", Applied Optics 37 (1998), 4200-4204.

[1.13] B. Lu, J. Zheng, B. Cai, B. Zhang, "Two-dimensional focusing of laser beams to provide uniform irradiation", Optics Communications 149 (1998), 19-26.

[1.14] K. Nemoto et al, "Optimum control of the laser beam intensity profile with a deformable mirror", Applied Optics 36 (1997), 7689-7695.

[1.15] S.P. Chang et al, "Transformation of gaussian to coherent uniform beams by inverse-gaussian transmittive filters", Applied Optics 37 (1998), 747-752.

[1.16] J. Liu, B.Y. Gu, " Laser beam shaping with polarisation-selective diffractive phase elements", Applied Optics 39 (2000), 3089-3092.

[1.17] D.L. Black et al, " Laser-based techniques for particle-size measurement: A review of sizing methods and their industrial applications", Prog, Energy Combust. Sci. 22 (1996), 267-306.

[1.18] J.R. Hodkinson, "Particle sizing by means of the forward scattering lobe", Applied Optics 5 (1966), 839-844.

[1.19] S. Boron, B.Waldie, "Particle sizing by forward lobe scattered intensity ratio technique: Errors introduced by applying diffraction theory in the Mie regime", Applied Optics 17 (1978), 1644-1648.

[1.20] M. Azzazi, C.F. Hess, "Characterization of suspended particulates on multicomponent systems using polarisation intensity ratio and pointer beam technique", Proc. SPIE:Particle Sizing and Analysis 573 (1985), 47-56.

[1.21] W.M. Farmer, "Measurement of particle size, number density and velocity using a laser interferometer", Applied Optics 11 (1972),2603-2612.

[1.22] C.R. Negus, L.E. Drain, "Mie calculations of the scattered light from a spherical particle traversing the fringe pattern produced by two intersecting beams", J. Phys. D : Appl. Phys. 15 (1982), 375-402.

[1.23] M. Azar, C.A. Ventrice, "Size determination of aerosol particles using the LDA-visibility technique in the backscatter direction", J. Aerosol Sci. 26 (1995), 1009-1017.

[1.24] F. Durst, M. Zare, " Laser Doppler measurements in two-phase flows", Proc. LDA Symp. (1975), 403-429.

[1.25] E.D. Hirleman, Part.Part. Syst. Char. 13 (1996), 59-67.

[1.26] F. Durst, G. Brenn, T.H. Xu, " A review of the development and characteristics of planar phase-Doppler anemometry", Meas. Sci. Technol. 8 (1997), 1203-1221.

[1.27] G. Grehan, G. Gouesbet, A. Naqwi, F. Durst, "Particle trajectory effects in phase Doppler systems: Computations and experiments", Part. Part. Syst. Charact. 10 (1993), 332-338.

[1.28] A. Naqwi, F. Durst, X. Liu, "Two optical methods for simultaneous measurement of particle size, velocity, and refractive index", Applied Optics 30, (1991), 4949-4959.

[1.29] F. Onofri et al, "Phase-Doppler anemometry with dual burst technique for particle refractive index measurements.", LISBON, 1994 .

[1.30] C.F.Hess, C.P. Wood, "Laser technique to measure particle size and velocity in high density applications", Proc. 6th Int. Symp. On Applications of Laser Techniques to Fluid Mechanics, Lisbon, Portugal (1992).

[1.31] C.F. Hess, C.P. Wood, " Pulse displacement technique – a single particle counter with a size range larger than 1000:1", Part. Part. Syst. Char. 11 (1994), 107-113.

[1.32] J.C.F. Wang, D.A. Tichenor, "Particle size measurements using an optical variable-frequency-grid technique", Applied Optics 20 (1981), 1367-1373.

[1.33] R. Semiat, A.E. Duckler, "Simultaneous measurement of size and velocity of bubbles or drops: a new optical technique", AICHE Journal 27 (1981), 148-159.

[1.34] H. Hamam, "Design of Talbot array illuminators", Optics Communications 131 (1996), 359-370.

[1.35] K.Patorski, Progress in Optics 27 (1989),1.

[1.36] H. Hamam, J.L. de Bougrenet de la Tocnay, J. Opt. Soc. Am. A 12 (1995), 1920.

[1.37] A.M.Smolyaninov, "An array generator based on the fractional Talbot effect for Gaussian beams", Optics Communications 133 (1997), 55-61.

[1.38] S. Ghosal, S.A. Self, " Particle size-density relation and cenosphere content of coal fly ash", Fuel 74 (1995), 522-529.

[1.39] A.R. Ramsden, M. Shibaoka, "Characterization and analysis of individual fly-ash particles from coal-fired power stations by a combination of optical microscopy, electron microscopy amd quantitative electron microprobe analysis", Atmospheric Environment 16 (1982), 2191-2206.

[1.40] Y. Mamane, J.L. Miller, T.G. Dzubay, "Characterization of individual fly ash particles emitted from coal- and oil-fired power plants", Atmospheric Environment 20 (1986), 2125-2135.

[1.41] H.L. Seung et al., Cement and concrete research 29 (1999), 1791-1797.

[1.42] J.B.A. Card, A.R. Jones, "A drop tube furnace study of coal combustion and unburned carbon content using optical techniques", Combustion and Flame 101 (1995), 539-547.

[1.43] R.H. Hurt, J.R. Gibbins, "Residual carbon from pulverized coal-fired boilers: 1. Size distribution and combustion reactivity", Fuel 74 (1995), 471-480.

[1.44] R. Hill, R. Rathbone, J.C. Hower, "Investigation of fly ash carbon by thermal analysis and optical microscopy", Cement and Concrete Research 28 (1998), 1479-1488.

[1.45] J.R. Dykstra, R.C. Brown, "Comparison of optically and microwave excited photoacoustic detection of unburned carbon in entrained fly ash", Fuel 74 (1995), 368-373.

[1.46] D.J. Waller, R.C Brown, "Photoacoustic response of unburnt carbon in fly ash to infrared radiation", Fuel 75 (1996), 1568-1574.

[1.47] M. Noda et al., "detection of carbon content in a high temperature environment using laser-induced breakdown spectroscopy", Spectochimica Acta Part B 57 (2002), 701-709.

[1.48] A.H. Biermann, J.M. Ondov, "Application of surface-deposition models to size-fractionnated coal fly ash", Atmospheric Environment 14 (1980), 289-295.

[1.49] S. Ghosal, J.L. Ebert, S.A. Self, "Chemical composition and size distributions for fly ashes", Fuel Processing Technology 44 (1995), 81-94.

[2.1] R.D. Kempster, P.A.E. Crosse, "Apparatus for monitoring the carbon content of boiler fly ash", European Patent Appl.No 86,307,677,4:Publication number EP 0217677 A2 (1987).

[2.2] J. Paya et al., "Thermogravimetric methods for determining carbon content in fly ashes", Cement and concrete research 28 (1998), 675-686.

[2.3] K.A. Katrinak, C.J. Zygarlicke, "Size related variations in coal fly ash composition as determined using automated scanning electron microscopy", Fuel Processing Technology 44 (1995), 71-79.

[2.4] M.M. Varoto-Valer et al., "Characterization of differing forms of unburned carbon present in fly ash separated by gradient centrifugation", Fuel 80 (2001), 795-800.

[2.5] E.J. Rask, J. Inst. Fuel 43-4 (1968), 339.

[2.6] E.L. Crow, K. Shimizu, "Lognormal distributions", Decker NY (1988).

[2.7] D.G. Goodwin, M. Mitchner, "Fly ash radiative properties and effects on radiative heat transfer in coal-fired systems", Int. J. Heat Mass Transfer 32 (1989), 627-638.

[2.8] P.J.A. Borm, "Toxicity and occupational health hazards of coal fly ash (CFA). A review of data and comparison to coal mine dust", Ann. occup. Hyg. 41-6 (1997), 659-676.

[2.9] A. Schneider, R. Chabicovsky, A. Aumuller, Sens. Actuators A, Phys 67 (1998), 24.

[2.10] C.F. Bohren, D.R. Huffman, "Absorption and scattering of light by small particles", Wiley&Sons (1983), p408.

[2.11] R.T. Killinger, R.H. Zerull in: G. Gouesbet, G. Grehan, editors. "Optical particle sizing: theory and practice", NY: Plenum Press (1988), 419-429.

[2.12] H. Bultynck et al., "A miniature monoblock backward phase-Doppler unit", Meas. Sci. Technol. 9 (1998), 161-170.

[4.1] G. Schirripa-Spagnolo, D. Ambrosini, "Talbot effect application: Measurement of distance with a Fourier-transform method", Meas. sci. Technol. 11 (2000), 77-82.

[4.2] M. Testorf et al., "Design of Talbot array illuminators for planar optics", Optics Communications 132 (1996), 205-211.

[4.3] E. Tepichin et al, "2-D Lau patterns: in-register incoherent joint superposition of Montgomery patterns", Optics Communications 125 (1996), 27-35.

[4.4] W.H. Yeh, M. Mansuripur, " Talbot imaging with increased spatial frequency: A technique for replicating truncated self-imaging objects", Optics Communications 170 (1999), 207-212.

[4.5] M.P. Silverman, W. Strange, "Projective imaging of periodic objects: Recognition and retrieval of lattice structures in real space", Optics Communications 152 (1998), 385-392.

[4.6] R.S. Longhurst, "Geometrical and physical optics", Longmans (1967), 259-262.

[4.7] E. Hecht, "Optics", Addison-Wesley (1987), 409-412.

[5.1] C.F. Bohren, D.R. Huffman, "Absorption and scattering of light by small particles", Wiley&Sons (1983), 83-104.

[5.2] A.A. Kokhanovsky, "Optics of light scattering media", Praxis Publications (2001), Appendix 2.

[6.1] H.C. Van De Hulst, "Light scattering by small particles", Dover Publications, NY (1981), 119-130.

[6.2] M. Kerker, "The scattering of light and other electromagnetic radiation", Academic Press, NY (1969), 54-59.

[6.3] C.F. Bohren, D.R. Huffman, "Absorption and scattering of light by small particles", Wiley&Sons (1983), 391.

[6.4] C.F. Bohren, D.R. Huffman, "Absorption and scattering of light by small particles", Wiley&Sons (1983), 390.

[6.5] R. Schodl, "A laser-two-focus (L2F) velocimeter for automatic flow vector measurements in the rotating components of turbomachines", J. Fluid Eng.,102 (1980), 412-419.